SEARCH FOR OUT-OF-TIME DECAYS OF STOPPED PARTICLES AT THE ATLAS DETECTOR

A DISSERTATION
SUBMITTED TO THE DEPARTMENT OF DEPARTMENT OF PHYSICS
AND THE COMMITTEE ON GRADUATE STUDIES
OF STANFORD UNIVERSITY
IN PARTIAL FULFILLMENT OF THE REQUIREMENTS
FOR THE DEGREE OF
DOCTOR OF PHILOSOPHY

Josh Cogan

March 2014

Acknowledgments

The ATLAS experiment is unequivocally *big science* and the success of my work is only possible thanks to the thousands of people who make CERN function. I am grateful to the scientists that designed and built the experiment, as well as the superb team of individuals who keep the LHC performing excellently.

Several people deserve a special note for their assistance on this dissertation who would otherwise go unnoticed: Jose Benitez for spending countless hours teaching me ROOT; Thilo Pauly and David Berger for their detailed knowledge of the trigger system; Mika Huhtinen and David Salek for their understanding of beam-induced backgrounds. This analysis benefited greatly from the insightful feedback from Guillaume Unal, Jamie Boyd and Andreas Hoecker during the editorial process. I personally benefited from an attentive thesis committee and group of readers including: JoAnne Hewett, Rafe Schindler, Vera Luth, Nick McKeown, and my academic advisor—Su Dong. Dr. Luth went above and beyond with her consistently thorough and detailed comments on this dissertation.

Of course, this study would not have amounted to much without the tireless attention and effort of Paul Jackson and Andrew Haas. These two post-docs turned professors went beyond mentoring and spent much time down in the analysis trenches with me. Finally, I would like to thank Emanuel Strauss, Rainer Bartoldus and Ray Sehgal for all their time and tutelage on topics not covered in this dissertation.

Preface

This dissertation has an incredible amount of information documented in the following ATLAS Internal Reports, both of which I was a primary editor of: ATL-COM-PHYS-2011-996, ATL-COM-PHYS-2013-665. Furthermore, several plots were reused from the non-collision background paper, known internally as DAPR-2012-01 and cited as [52]. However, several sections contain information not succinctly documented elsewhere, that may be of particular interest to readers redoing or extend the analysis: 4.1.3, 4.2.4 and 6.1.

Abstract

On July 4^{th} 2012, the ATLAS and CMS experiments announced the discovery of a new particle, later declared to be one of possibly many Higgs bosons [51, 53]. The Higgs mechanism has been so successful explaining several striking features of fundamental particle physics it was the topic of the 2013 Nobel Prize in physics. However, this mechanism provides a few problems of it's own. Most importantly, both the mass of the new Higgs boson and the cosmological constant must be extremely fine-tuned to produce a universe remotely similar to the one we observe today. Supersymmetry, a hypothetical extension to the current theory, addresses many problems in theoretical and experimental physics including the fine-tuned Higgs mass. In this work, a variant, called Split-Supersymmetry, is investigated; it avoids some problems in standard Supersymmetry while explicitly leaving the Higgs mass fine-tuned.

A experimentally unique feature of Split-Supersymmetry is the production of R-hadrons—composite, massive, long-lived, particles. Indeed such long-lived states are predicted in several scenarios of physics beyond the Standard Model, and this search is sensitive to them as well. This dissertation describes the ATLAS searches using 2010, 2011 and 2012 data for gluino and squark R-hadrons which have come to rest within the ATLAS detector, particularly the calorimeter, and decay at some later time to jets or $t\bar{t}$ and a neutralino. Candidate decay events are triggered in the empty bunch crossings in order to remove collision backgrounds. Selections based on jet shape and muon-system activity are applied to discriminate events from backgrounds, the largest of which are cosmic and beam-halo muons. In the absence of a excess, limits are placed on the new particle mass as a function of its lifetime, for various neutralino masses and decay types.

Contents

List of Tables

List of Figures

Chapter 1

Introduction

Something funny, even prophetic, was happening in physics during the 1920's, as the academic community attempted to reconcile the conservation of energy in the macroscopic world its the apparent violation in beta decay. There are two schools of thought worth mentioning here. The first, which included Niels Bohr, stated that conservation of energy simply did not apply to these new atomic systems being studied. This was not as revolutionary as it sounds in retrospect; why would a property of celestial bodies and balls on ramps apply to systems many millions of times smaller? The second school of thought, led by Wolfgang Pauli, demanded that the conservation of energy applied to the new system as well and instead "invented" a new particle to carry away the missing energy. Remember at this time, no non-ionising radiation had been discovered.

While in this particular example, we now know Pauli had the right idea, the spirit of the debate has continued through the past century of particle physics. Given a set of fundamental laws of physics that successfully describe all but a few systems, do we abandon the law as inapplicable, or invent a new hidden particle or family of particles to save it? Indeed, this was the very motivation for the search for the top quark, Higgs boson, supersymmetry and to find them, the excellent work at CERN and other facilities around the world.

This dissertation, however, considers the consequences of abandoning the low-energy theory as "finely-tuned" instead of carefully concocting a model extension to save it. Specifically, it covers a search at the ATLAS detector for a long-lived gluino—a generic signature of split supersymmetry (split-SUSY). This analysis could detect a wide variety of meta-stable particles, but the primary effort is devoted to a scenario with a new long-lived particle (LLP) carrying color charge, which eventually decays and produces at least 100 GeV of visible energy.

1.1 Overview

Long-lived massive particles appear in many theories beyond the Standard Model [60]. They are predicted in supersymmetry (SUSY) models, such as split-SUSY [80, 26] and gauge-mediated supersymmetry breaking (GMSB) [83], as well as other exotic scenarios, e.g. Universal Extra Dimensions [86] and leptoquark theories [38]. Long-lived massive particles containing a heavy colored particle are called R-hadrons.[1] ATLAS [4] studies focus on gluinos that occur in split-SUSY, which attempts to solve the hierarchy problem by the same fine-tuning mechanism that solves the cosmological constant problem, removing a primary motivation for low energy SUSY. Given this condition, SUSY can be broken at a very high energy scale, leading to heavy fermions, light scalars and a light finely tuned Higgs particle [80]. Within this phenomenological picture, squarks will be much heavier than gluinos, suppressing the gluino decay and resulting in meta-stable gluinos. If the lifetime of the gluino is long enough, it will hadronize into R-mesons ($\tilde{g}q\bar{q}$), R-baryons ($\tilde{g}qqq$), and so-called R-gluinoballs ($\tilde{g}g$). Other models, notably R-parity violating (RPV) SUSY, can produce a long lived squark that would also form an R-hadron; this phenomenology is comparable to the gluino production.

R-hadron interactions in matter are highly uncertain, but some features are well predicted. The gluino can be regarded as a heavy, non-interacting spectator, surrounded by a cloud of interacting quarks. R-hadrons change their properties through strong interactions with the detector: most R-mesons will turn into R-baryons [71] and they can also change their electric charge. At the Large Hadron Collider (LHC) at CERN [59], the gluino R-hadrons (if they are realized in nature) will be produced

[1] This R corresponds to the R-parity found in SUSY.

in pairs and approximately back-to-back in the transverse plane. Some fraction of these R-hadrons will lose all of their momentum, mainly from ionization energy loss, and come to rest within the detector volume, only to decay at some later time. For this search, we use a trigger operating only in the empty bunches of the LHC bunch structure to remove backgrounds close in time with collision processes, leaving only some small machine-related backgrounds and natural sources such as cosmic rays.

1.2 Literature Review

The results discussed in this dissertation have been published [13]. A previous search for stopped gluino R-hadrons was performed by the D0 collaboration [89] which excluded a signal for gluinos with masses up to 250 GeV[2]. This analysis, however, could only use the filled crossings in the Tevatron bunch scheme and demanded that there were no non-diffractive interactions present to suppress collision related backgrounds. Search techniques similar to those described herein have also been considered by the CMS collaboration [88, 44] using 4fb^{-1} of 7 TeV data under the assumptions that gluino mass ($m_{\tilde{g}}$) is at least 100 GeV higher than the neutralino's mass and the gluino may only decay to gluon and neutralino. The resulting limit, at 95% confidence level, is $m_{\tilde{g}} < 640$ GeV for lifetimes from 10 μs to 1000 s. ATLAS has up to now only studied 31 pb^{-1} of data recorded in 2010 [9], resulting in limits on $m_{\tilde{g}} < 341$ GeV, under similar assumptions.

Furthermore, many of the standard model (SM) extensions predict the production of particles which, some fraction of the time, traverse the detector and appears as heavy stable charged particles. These have been studied at the four LEP experiments [31, 22, 23, 21], HERA [24], D0 [18, 19, 20], CDF [17],CMS [70, 45, 43], and ATLAS [6, 7, 5, 14, 12].

[2]Natural units, with $c = 1 = \hbar$, are used throughout.

Chapter 2

Theory

This study searches for new meta-stable particles that, after getting trapped in the ATLAS calorimeter, decay out-of-time with the LHC bunch crossings. The signature, while unusual, is sensitive to many SM extensions not yet ruled out. For a particle to be selected in this analysis, it must

1. Have a lifetime $\boldsymbol{\tau \gtrsim 10\,\mu}$**s**. Otherwise, the particle decays during a train of colliding bunches.

2. Be **electrically charged** while traversing at least part the ATLAS detector, so it may get trapped in the material surrounding the interaction point.

3. Be produced at relatively slow speed, $\boldsymbol{\beta \lesssim 0.15}$. to be stopped by the ATLAS calorimeters.

4. Release $\boldsymbol{E > 100\,\mathrm{GeV}}$ of visible energy in its decay, and pass the ATLAS trigger requirements.

5. Produce **no muon** with momentum $\gtrsim 1\,\mathrm{GeV}$ in its the decay, to avoid vetoes designed to reject cosmic-ray muons.

Indeed a wide variety of models could produce new particles satisfying the above conditions. In the ensuing dissertation, only new colored particles are considered, for theoretical interpretation—specifically the gluino from split-SUSY. But the long-lived stau lepton found in some GMSB models could also stop and have detectable decays, for example. Above all else, this is an experimental dissertation and most effort is spent on discussing methods and cross-checks. However, we believe we have tackled one of the "hardest" signature—the R-hadron. Reinterpreting the limits for simpler color-singlets would not require the full GEANT4 model we employed, since the fraction of R-hadrons stopping is significantly easier to calculate.

Historically, LLPs become testbeds to accurately measure phenomena driven from much higher-scale phenomena, such as the CP-violation in the neutral kaon system. Generally there are three mechanisms that can extend a particles decay time: tunneling through a energetically-forbidden state, suppressed couplings, or small available phase space. The last reason, which gives the neutron its long life time compared to the muon, does not contribute to models pertinent here because of the requirement on visible decay energy of $E > 100\,\mathrm{GeV}$. However, the current model of particle physics and supporting experimental data do not seem to require a new LLP satisfying the above conditions[1], so why go searching for one?

Roughly speaking, there are two reasons. First and requiring less exposition, we are experimentalists so we experiment. Science is often guided by having a good guess where to look, and yet often finds new effects in unexpected places; so we look for plausible if "unusual" signatures[2]. To understand the second reason, supersymmetry, we must introduce the Standard Model, and the Higgs potential. Once there, we discuss three viable predictions of supersymmetry: namely a colored LLP: split-supersymmetry, gravitino lightest supersymmetric particle (LSP) and R-parity violating.

[1] Dark matter is, of course, a new LLP but this search would miss it because of the contradictory charge requirements; dark matter would pass right through the ATLAS calorimeter unfettered.

[2] On the discovery of the muon, Nobel laureate Rabi famously quipped "who ordered that?"

2.1 The Standard Model

The scientific community thinks very highly of a model named *The Standard Model*, and perhaps rightfully so. With a few exceptions that will be discussed later, the SM has predicted, with incredible accuracy, all observed subatomic phenomena. Indeed the theory does not breakdown for larger, macroscopic scales; it simply becomes too cumbersome a tool, and more approximative descriptions are used. The SM contains the details of what is in the universe (i.e. what kinds of particles) and how they interact (i.e. what forces do they experience), while relying on quantum field theory (QFT) to calculate observable phenomena.

It is hard to pick a semantically perfect definition of how to count the number of different types of subatomic particles, but a common one (followed here) has 61: 48 fermions and 13 bosons.

2.1.1 Group Theory

In 1918, mathematician Emmy Noether showed a connection between differentiable symmetries of a Lagrangian and the corresponding conservation laws [81]. When coupled with the physical principle that global symmetries should actually be local symmetries–ones that each point in space-time may redefine. Here, a “symmetry” refers to an transformation that can be performed on a Lagrangian without changing the behavior of the system it describes. Since multiple transformations can be applied, and we require then any of them can be undone, it’s convenient to employ group theory to describe symmetries. Specifically, Noether’s theorem only applies to differentiable symmetries which we are primarily interested in Lie groups and their corresponding Lie algebras.

Let us illustrate the issue with a concrete example, taking notation from Peskin and Schroeder [p78]. Below is the action, S, describing a relativistic, non-interacting, electron field.

$$S = \int d^4x \; \bar{\psi} \left(i\gamma^\mu \partial_\mu - m \right) \psi \tag{2.1}$$

Given quantum mechanics has a global phase ambiguity for all wavefunctions, we know that transforming $\psi \to e^{i\alpha}\psi$ should, and does, leave the action invariant. Let us demand that this global U(1) symmetry is in fact a local symmetry, and try transforming $\psi \to e^{i\alpha(x^\mu)}\psi$.

$$S \to \int d^4x \; \bar{\psi}\,(i\gamma^\mu\partial_\mu - m)\,\psi - \bar{\psi}\gamma^\mu[\partial_\mu\alpha(x^\mu)]\psi \tag{2.2}$$

The action is not quite invariant. Introducing a vector field transforming like $A_\mu \to A_\mu - \partial_\mu\alpha(x^\mu)$ solves the problem however.

$$S = \int d^4x \; \bar{\psi}\,(i\gamma^\mu\partial_\mu - \gamma^\mu A_\mu(x^\mu) - m)\,\psi \tag{2.3}$$

At the cost of introducing a new field, whose significance will become clear soon, we have an action that is completely invariant under local U(1) transformations. The electron must interact with this A-field, but we do not know what it is exactly; are there other invariant terms with just A that we can add? Taking a guess from classical electromagnetism, we note that the field stress tensor $F_{\mu\nu} = \partial_\mu A_\nu - \partial_\nu A_\mu$ is invariant under $A_\mu \to A_\mu - \partial_\mu\alpha(x^\mu)$. The indices on $F_{\mu\nu}$ can only be contracted one non-trivial way: $F_{\mu\nu}F^{\mu\nu}$ since $\partial^\mu\partial^\nu F_{\mu\nu} = 0$.

Notice that a mass term, $m^2A^\mu A_\mu$, explicitly violates the action's invariance, a generic fact for new fields introduced for symmetry reasons, known as gauge fields.

2.1.2 The Standard Fermions

The fermions (particles with half-integer spin) account for what is normally considered the "matter" component. While it is possible to have a fundamental 3/2-spin particle, none exist in the SM. Thus, only two properties can discriminant between the fermions: mass and charge. The fermions are typically split into groups called quarks and leptons depending on whether they transform like triplets or singlets under SU(3)–equivalently if they have color-charge. The strong interaction describes the forces that affect particles carrying color-charge. Both groups have three known families such that each family is identical except for mass. For example, there are three quark families, each one with an SU(2) doublet for the left-handed up and down type, and an SU(2) singlet for the right-handed up types and another for the down types.

$$Q_L^i = \left(\begin{pmatrix} u_L \\ d_L \end{pmatrix}, \begin{pmatrix} c_L \\ s_L \end{pmatrix}, \begin{pmatrix} t_L \\ b_L \end{pmatrix} \right) \tag{2.4}$$

$$u_R^i = (u_R, c_R, t_R) \tag{2.5}$$

$$d_R^i = (d_R, s_R, b_R) \tag{2.6}$$

$$\tag{2.7}$$

This separation means that the SM is a *chiral* theory since it is not invariant under spatial reflections. In fact, charged weak interactions maximally violate parity, and thus the W^i bosons, discussed below, only couple to left-handed fermions. Equation 2.4 shows six particles, but since each quark has a corresponding antiquark and can carry one of three color charges, we tend to count 36 quarks in total.

The remaining 12 fermions are leptons which include the electron, neutrino and their respective families. This group of particles is almost identical to the quarks except for the lack of color charge. Additionally, the down-type left-handed leptons, known as neutrinos, are capable of oscillating between flavor states. This behavior has strong experimental limits on it in the quark sector.

$$L_L^i = \left(\begin{pmatrix} e_L \\ \nu_{eL} \end{pmatrix}, \begin{pmatrix} \mu_L \\ \nu_{\mu L} \end{pmatrix}, \begin{pmatrix} \tau_L \\ \nu_{\tau L} \end{pmatrix} \right) \tag{2.8}$$

$$e_R^i = (e_R, \mu_R, \tau_R) \tag{2.9}$$

$$\tag{2.10}$$

Note that Equation 2.4 and 2.8 naturally provide both lepton universality and maximal parity violation. However because the left- and right-handed versions of the same particle have different charge simple mass terms like $m^2 \bar{f}_L f_R$ are not allowed. We will have to wait till the discussion of the Higgs mechanism to resolve this puzzle.

2.1.3 The Standard Model Gauge Bosons

The Standard Model realizes a symmetry group much larger than just U(1). Ignoring spacetime which has a SO(3,1), the SM follows a SU(3) $\otimes$ SU(2) $\otimes$ U(1) internal symmetry. Given SU(N) has $N^2 - 1$ real degrees of freedom, and U(1) has 1, then we expect a total of $8 + 3 + 1 = 12$ gauge bosons. Indeed all 12 are there but not all are massless, as naively expected. The first 8 correspond to the unbroken SU(3) of quantum chromodynamics (QCD) and are thus referred to collectively as gluons. Since neither the Lagrangian nor the ground-state violate this symmetry, they are massless and the three colors are indistinguishable.

The other four gauge bosons mediate the electroweak forces: $W^{\pm}$,Z, and γ. While the photon is an excellent candidate (massless and uncharged) for the U(1) boson, the masses of the W and Z violate gauge invariance. This problem has been a prime focus of particle physics for decades: the W appears to be a gauge boson because of its universal fermion couplings, but it has a non-trivial mass. The solution, the Glashow-Weinberg-Salam model, unified the weak force with the electromagnetic but it required another mechanism to explicitly break an SU(2) gauge, granting the W and Z mass. The Higgs mechanism does just the trick by having a ground-state that spontaneously breaks the symmetry even though the Lagrangian (and thus high-energy theory) does not.

2.1.4 Higgs Mechanism

As of late 2013, there is strong evidence from both ATLAS and CMS that there is at least one Higgs boson, and its mass is $\approx 126\,\mathrm{GeV}$ [8, 42, 46, 3, 2]. The new scalar has been observed decaying to Z, W and γ pairs, with rates consistent with a top-mediated gluon-fusion loop. In this section, it is assumed that the Higgs couples to the W, Z, and top quark according to the SM prediction.

Here, I follow notation introduced and concepts introduced elsewhere [54]. First, we write down the kinetic terms of the three SU(2) fields and the one U(1) field (since we hope to show that exactly three get masses).

$$L = -\frac{1}{4} W_i^{\mu\nu} W_{i\mu\nu} - \frac{1}{4} B^{\mu\nu} B_{\mu\nu} \tag{2.11}$$

where W and B are the analogs to $F^{\mu\nu}$ in classical electromagnetism

$$W_{\mu\nu}^i = \partial_\nu W_{i\mu} - \partial_\mu W_{i\nu} + g\epsilon^{ijk} W_{j\mu} W_{k\nu} \tag{2.12}$$

$$B_{\mu\nu} = \partial_\nu B_\mu - \partial_\mu B_\nu \tag{2.13}$$

Now we introduce two new complex-valued scalar fields, $\Phi^\dagger = \left(\phi_+^*, \phi^*\right)$ which transform as a SU(2) doublet, with the following potential

$$V(\Phi) = \mu^2 \Phi^\dagger \Phi + \lambda \left(\Phi^\dagger \Phi\right)^2 = \mu^2 \left(\phi_+^* \phi_+ + \phi^* \phi\right) + \lambda \left(\phi_+^* \phi_+ + \phi^* \phi\right)^2 \tag{2.14}$$

and kinetic terms, where D_μ is the covariant derivative[3] corresponding to

$$\left(D^\mu \Phi\right)^\dagger \left(D_\mu \Phi\right), \quad D_\mu = \partial_\mu + ig/2\vec{W}_\mu \vec{\sigma} + ig'/2B_\mu \tag{2.15}$$

The new Lagrangian is

$$L_{\text{G.W.S}} = \left(D^\mu \Phi\right)^\dagger \left(D_\mu \Phi\right) + V(\Phi) - \frac{1}{4} W_i^{\mu\nu} W_{i\mu\nu} - \frac{1}{4} B^{\mu\nu} B_{\mu\nu} \tag{2.16}$$

Notice that in the ground state–the field configuration with lowest energy–Φ might not be identically zero everywhere. When $\mu^2 < 0$, Φ acquires a vacuum-expectation value, v, and the field configuration of minimal energy corresponds to $\langle \Phi^\dagger \Phi \rangle = \frac{-\mu^2}{2\lambda} = \frac{v^2}{2}$, for all points in space-time. This corresponds to a downward "shift" of $\frac{-\mu^4}{4\lambda}$ in energy density. For physical processes where the energy density is significantly less than $\frac{\mu^4}{4\lambda}$, the Φ-potential is well approximated by

$$V(\phi) \approx -2\mu^2 \left(\phi - \sqrt{\frac{-\mu}{2\lambda}}\right)^2 - \frac{\mu^4}{4\lambda} \tag{2.17}$$

[3]Here, we are cheating with the notation and dropping the Y_W for weak hypercharge. Luckily later in Equation 2.25 the final expression provides the right intuition.

Without loss of generality, we can rewrite

$$\Phi(x) = \frac{e^{i\vec{\chi}(x)\cdot\vec{\sigma}+i\theta(x)}}{\sqrt{2}} \begin{pmatrix} 0 \\ v + h(x) \end{pmatrix} \tag{2.18}$$

where $\chi(x)$, $h(x)$ are all real-valued, and $v = \sqrt{\frac{-\mu^2}{\lambda}}$. As usual, σ denotes the Pauli matrices, which are the generators of SU(2) and θ is the generator of U(1). Since we can perform physical calculations in any gauge, we chose the *unitarity gauge* where $\vec{\chi}(x) = 0$, and $\theta = 0$. Expanding the Pauli matrices, the covariant derivative of the scalar field becomes

$$D_\mu\Phi = \frac{1}{\sqrt{2}} \begin{pmatrix} \left(\frac{ig}{2}W_{1\mu} + \frac{g}{2}W_{2\mu}\right)(v+h) \\ \partial_\mu h - \frac{ig}{2}W_{3\mu}(v+h) + \frac{ig'}{2}B_\mu(v+h) \end{pmatrix} \tag{2.19}$$

Before we calculate $(D^\mu\Phi)^\dagger(D_\mu\Phi)$, let's change the basis, so the final answer is simpler. Let

$$W_\mu^\pm = \frac{1}{\sqrt{2}}(W_{1\mu} \mp iW_{2\mu}) \tag{2.20}$$

$$Z_\mu = \frac{1}{\sqrt{g^2+g'^2}}(gW_{3\mu} - g'B_\mu) \tag{2.21}$$

$$A_\mu = \frac{1}{\sqrt{g^2+g'^2}}(g'W_{3\mu} + gB_\mu) \tag{2.22}$$

then,

$$(D^\mu\Phi)^\dagger(D_\mu\Phi) = \frac{g^2}{4}W^{\mu-}W_\mu^+(v+h)^2 + \frac{g^2+g'^2}{8}Z^\mu Z_\mu(v+h)^2 + \frac{1}{2}\partial^\mu h\partial_\mu h \tag{2.23}$$

Notice that after expanding the $(v+h)^2$ terms, there are new mass terms for the gauge bosons[4]: $m_{W^\pm} = \frac{gv}{2}$, $m_Z = \frac{v\sqrt{g^2+g'^2}}{2}$, and $m_A = 0$. Thus from the four original gauge bosons, three have acquired mass and the new scalar field also appears massive,

[4]Note that there are actually two W-mass terms, which account for the extra factor of two between the W and Z mass denominator

as shown below.

$$
\begin{aligned}
L_{\text{G.W.S.}} = &-\frac{1}{4}W_i^{\mu\nu}W_{i\mu\nu} - \frac{1}{4}B^{\mu\nu}B_{\mu\nu} \\
&+ \left(m_W^2 W^{\mu-}W_\mu^+ + \frac{m_Z^2}{2}Z^\mu Z_\mu\right)\left(1 + \frac{2}{v}h + \frac{1}{v^2}h^2\right) \\
&+ \frac{1}{2}\partial^\mu h \partial_\mu + 2\mu^2 h^2
\end{aligned}
\tag{2.24}
$$

Furthermore, after rotating the W^3 and B fields into Z and A, the covariant derivative from Equation 2.15 becomes the familiar expression after fixing $e = g\sin(\theta_W) = g\frac{g'}{\sqrt{g^2+g'^2}}$.

$$
\begin{aligned}
D_\mu = &\ \partial_\mu \\
&+ i\frac{e}{\sqrt{2}\sin(\theta_W)}W_\mu^+ \begin{pmatrix} 0 & 0 \\ 1 & 0 \end{pmatrix} \\
&+ i\frac{e}{\sqrt{2}\sin(\theta_W)}W_\mu^- \begin{pmatrix} 0 & 1 \\ 0 & 0 \end{pmatrix} \\
&+ ieZ_\mu \begin{pmatrix} \cot(2\theta_W) & 0 \\ 0 & -\csc(2\theta_W) \end{pmatrix} \\
&+ ieA_\mu \begin{pmatrix} 1 & 0 \\ 0 & 0 \end{pmatrix}
\end{aligned}
\tag{2.25}
$$

To understand just how far we have come, imagine the kinetic term for one lepton family[5]. In Equation 2.26, we get just the electroweak coupling we had hoped for: charged current couples the neutrino and charged lepton while the neutral current does not.

[5] Because we dropped Y_W, which equals 1 in this examples, from Equation 2.15 the expression does not give the right form of the quark couplings, but does for the left-handed leptons.

$$\bar{\psi_L}\gamma^\mu D_\mu \psi_L = (\bar{e_L}, \bar{\nu_e})\, \gamma^\mu D_\mu \begin{pmatrix} e_L \\ \nu_e \end{pmatrix}$$
$$= \bar{e_L}\gamma^\mu \partial_\mu e_L + \bar{\nu_e}\gamma^\mu \partial_\mu \nu_e$$
$$+ \frac{ie}{\sqrt{2}\sin(\theta_W)}\bar{\nu_e}\gamma^\mu W_\mu^+ e_L + \frac{ie}{\sqrt{2}\sin(\theta_W)}\bar{e_L}\gamma^\mu W_\mu^- \nu_e$$
$$+ ie\cot(2\theta_W)\bar{e_L}\gamma^\mu Z_\mu e_L - ie\csc(2\theta_W)\bar{\nu_e}\gamma^\mu Z_\mu \nu_e + iee\bar{e_L}\gamma^\mu A_\mu e_L \tag{2.26}$$

Finally there remains the problem of chiral fermion mass in the SM, but again the Higgs field remedies this problem too. The SM Lagrangian can accommodate the Yukawa terms like $\lambda_f \Psi_L \Phi \Psi_R$, without violating SU(2) symmetry. After the scalar field acquires a vacuum expectation value, the fermions accommodate a mass $m_f = \lambda_f v$ and interact with the dynamic Higgs boson with coupling equal to m_f. Interestingly, for all fermions $\lambda_f \ll 1$, except for the top quark for which $\lambda_t \approx 1$.

2.2 Motivating Supersymmetry

The SM of particle physics has successfully predicted a wide variety of subatomic phenomena. It does, like all great models, fail to explain a few features observed in nature. A comprehensive discussion of all the SM's shortcomings is beyond this work's scope, so a few topics such as neutrino masses and the strong CP problem will be skipped. The following SM dilemmas will be discussed briefly however: dark matter, grand unification, quantum gravity, and two hierarchy problems. These will naturally lead us to examine SUSY as a possible extension to the SM.

2.2.1 Supersymmetry Basics

Here, only a few relevant details about SUSY will be discussed; for a thorough overview, on which this work is based, see Martin's *Supersymmetry Primer* [79]. SUSY in its most general form introduces an operator which converts a boson into a fermion and vice versa. An approximate form of this operator is shown in Equation 2.27.

$$Q|Boson\rangle = |Fermion\rangle \ , \quad Q|Fermion\rangle = |Boson\rangle \tag{2.27}$$

The precise form of the supersymmetry algebra relations are listed in Equation 2.28,2.29.

$$\left\{Q_\alpha, Q^\dagger_{\dot\alpha}\right\} = Q_\alpha Q^\dagger_{\dot\alpha} + Q^\dagger_{\dot\alpha} Q_\alpha = \begin{pmatrix} P_0 + P_3 & P_1 + iP_2 \\ P_1 - iP_2 & P_0 - P_3 \end{pmatrix}_{\alpha,\dot\alpha} \tag{2.28}$$

$$\{Q_\alpha, Q_\beta\} = 0 = \left\{Q^\dagger_{\dot\alpha}, Q^\dagger_{\dot\beta}\right\} \tag{2.29}$$

The following commutation relationship follows from the fact that supersymmetry is a global transformation and $[P^\mu, X] = i\partial^\mu X$,

$$[Q_\alpha, P^\mu] = 0 = \left[Q^\dagger_{\dot\alpha}, P^\mu\right] \tag{2.30}$$

Now, Equation 2.30 demands that $[P^\mu P_\mu, Q_\alpha] = 0$, which implies that the supersymmetry operator leaves the mass of a state, $-P^\mu P_\mu$, unaltered. Furthermore, since Q and $Q^\dagger$ commute with the generators of the gauge transformations, the states produced by theses operators also have equal charge under the fundamental forces. But if the super-partners had the same mass and the same charge, they would have been observed years ago. Yet we have not observed any super-partners (sparticles). So if nature realizes SUSY there must be some spontaneous breaking of the ground-state that allows the Lagrangian to respect the (anti)commutation relationships even though the low-energy theory, the SM, does not. This would allow the masses of the super-partners to grow large enough to have escaped detection.

The simplest SUSY we have introduced already has quite a few phenomenological problems that require parameter tuning. For example, in this basic form SUSY has lepton, and baryon number violating terms[6] and flavor changing neutral currents. To

[6]Recall there is no known symmetry in the SM to protect baryon and lepton number but the experimental constrains on their conservation are quite strong.

control SUSY terms that lead to measurable large baryon or lepton number violation, a new fundamental Z_2 symmetry called R or matter parity is assumed. Typically defined as

$$R - \text{parity} = P_R = (-1)^{3(B-L)+2s} \tag{2.31}$$

where s is the particle spin and enforced at each interaction vertex; all the sparticles have $P_R = -1$ and matter particles $P_R = 1$. Since each sparticle decay must lead to an odd number of new sparticles, there is a LSP that cannot decay without violating R-parity. If the LSP carries no color or electric charge then it is an excellent dark matter candidate and is discussed later.

Despite these problems, even as it is, SUSY already solved several large theoretical problems including quantum gravity and grand unification.

2.2.2 Quantum Gravity and Grand Unification

In it's current form, the SM explains well three of the four observed force. Gravity, and its hypothetical force-carrier, the graviton are conspicuously missing from the SM Lagrangian; we must turn to the classical theory of general relativity for a satisfactory mathematical model. Early attempts to marry gravitation with quantum field theory discovered that quantum gravity required a *local* version of SUSY [56, 62]. Furthermore earlier formal results had shown that SUSY is the only realistic theory [7] able to nontrivially mix the Poincaré symmetry with internal ones [50, 84]. Indeed, SUSY appears to be the only way to unify the SM and gravity.

Due to higher-order corrections, the apparent gauge couplings change with energy. In QCD α_s diverges near 200 MeV, setting the proton mass. If there existed an energy scale where all three forces had equal coupling constants, they would have *unified*. This is a desirable property of theories because it implies an deeper underlying theory with few free parameters. Unfortunately, in the SM α_1 and α_2 intersect at an energy scale 10^4 lower than α_2 and α_3, as show in Figure 2.1.

[7] Recall from Section 2.1 that left- and right-handed fermions carry different charges for $SU(2)_L$ and $U(1)_Y$

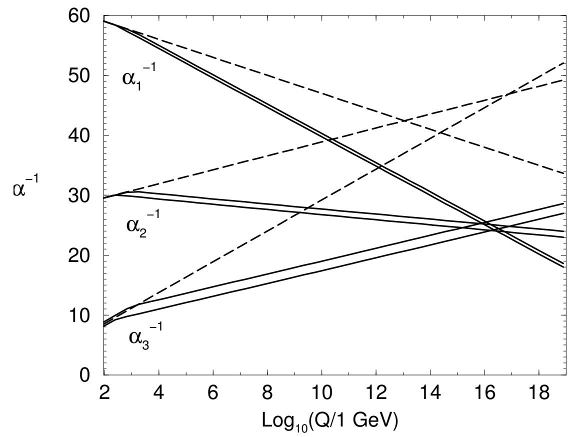

(a) SM and low-energy SUSY running couplings

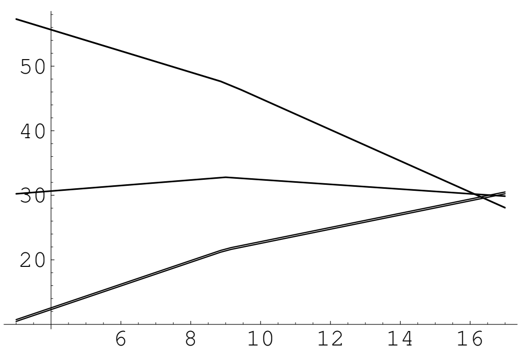

(b) Split-SUSY running couplings

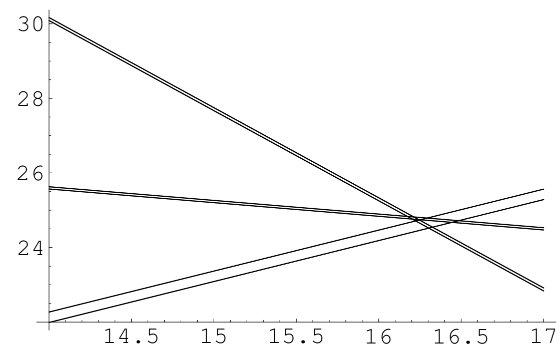

(c) Zoom in low-energy SUSY running couplings

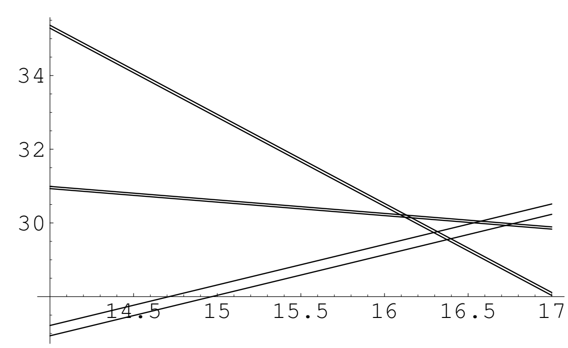

(d) Zoom in Split-SUSY running couplings

Figure 2.1: Figure 2.1(a) shows the running couplings in the SM (solid band) and Minimal Supersymmetric Model (dashed)[58, 36]. Figure 2.1(b), 2.1(d), and 2.1(c) show the how split-SUSY running compares to the minimal supersymetric standard model [80]. The x- and y-axis label is identical across all plots.

With the introduction of new particles even at relatively low energies (10^3 GeV), the three forces come remarkably close to unifying at a single strength just above 10^{16} GeV.

2.2.3 Dark Matter

During the 1930's, evidence began to trickle in that stars in distant galaxies moved in a gravitational well much deeper than the mass of the stars would predict. As experimental methods improved, it became evident that a significant fraction of the gravitational pull on stars could not come from the other luminous matter. Dark matter (DM) is a proposed new type of matter that is relatively massive and does not carry electromagnetic or color charge. The limits on the dark matter's individual particle mass, are model-dependent, but mostly come from large structure formation constraints and disallow light but the otherwise-adequate neutrinos from playing the part.

Despite SUSY being introduced for completely unrelated reasons, it provides several excellent candidates for the dark matter particle, since the LSP is stable. At first glance, the super-partners to the neutral particles could all serve the role: wino, bino, higgsino, sneutrino and gravitino. Since the winos and the bino mix, the mass eigenstates are often written in terms of charginos $\tilde{\chi}_i^{\pm}$ and two neutralinos $\tilde{\chi}_i^0$. For the purposes, all these DM scenarios are similar in the LLP phenomenology, except for the gravitino case. Since the gravitino couples so feebly to other particles, the next-next-to-lightest supersymmetric particle (NLSP) also becomes long-lived. There are however complex constraints on gravitino cosmology as discussed elsewhere [40]. Furthermore, SUSY's new heavy particles would also occur at nearly correct thermal relic densities.

2.2.4 Fine-Tuning Problems

Together, the SM and general relativity lead to a theoretical catastrophe called the *cosmological constant problem*; the argument goes as follows. From cosmological measurements we know the curvature of the universe corresponds to an energy density of

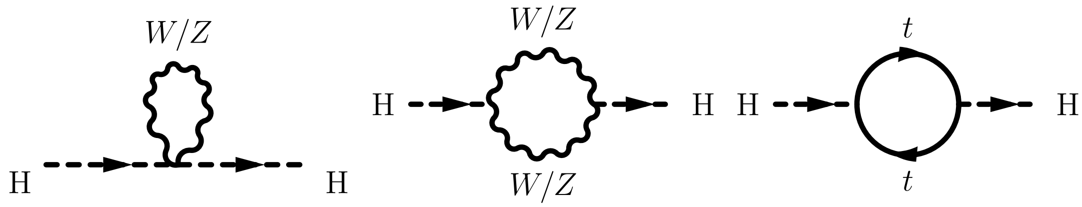

(a) $\Delta m_h^2 \propto e^2\ \Lambda_{\mathrm{UV}}^2$ (b) $\Delta m_h^2 \propto e\ m_{W/Z}\ \Lambda_{\mathrm{UV}}^2$ (c) $\Delta m_h^2 \propto -(m_t/v)^2\ \Lambda_{\mathrm{UV}}^2$

Figure 2.2: Feynman diagrams contributing radiative corrections to the Higgs mass. All loops are quadratically sensitive to the cut-off scale, Λ_{UV}.

$\Omega \approx 6\frac{GeV/c^2}{m^3}$. However QFT naively suggests that there is only one natural scale—the Planck scale—which corresponds to an energy density of $\Omega_P \approx 4 \times 10^{120}\frac{GeV/c^2}{m^3}$. This guess is not very close, but perhaps we should not be surprised since the SM does include extra non-trivial scales like the electroweak and QCD Landau pole. Using the Higgs energy density derived from the measured Higgs mass and vacuum expectation value, the calculated density is still far too large: $\Omega_H \approx 3 \times 10^{55}\frac{GeV/c^2}{m^3}$. The energy density calculated above could be cancelled with an *ad-hoc* term, known as the cosmological constant, added to Einstein's field equations. Unfortunately this cosmological constants value must be precisely tuned to cancel the large densities discussed above. This fine-tuning remains relatively unaddressed in the current understanding.

There is, however, a fine-tuning in the SM, that SUSY could address. The Higgs mass receives potentially very large radiative corrections from processes like those depicted in Figure 2.2. As usual we suppose there is some loop-integral cut-off scale, Λ_{UV} where new physics enters and regulates the divergent behavior of the loop. In the limit $\Lambda_{\mathrm{UV}} = M_P$, the Higgs pole mass must be fine-tuned to match the radiative corrections to one part in 10^{30}. SUSY, by introducing, superpartners with opposite spin-statistics, regulates this behavior. With SUSY, the Higgs mass corrections become only logarithmically dependent on the cut-off scale but are now quadratically sensitive to the superpartner mass.

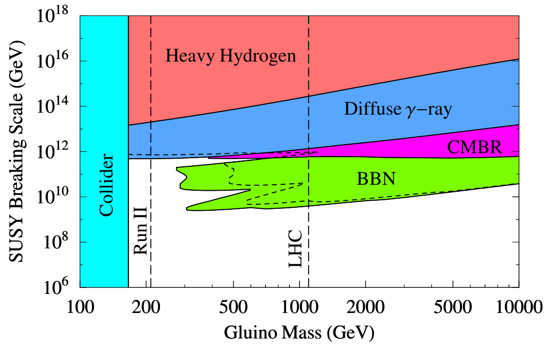

(a) General gluino cosmology limits

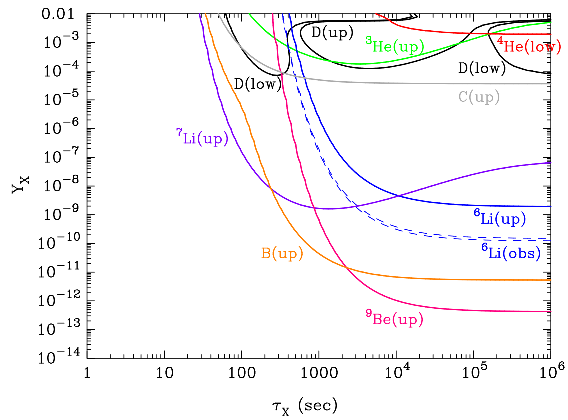

(b) Big Bang Nucleosynthesis limits

Figure 2.3: Limits on gluino mass and lifetime based on various cosmological limits. The left figure shows limits from several different cosmological constraints [28]. However it only considers the destructive forces of gluino decay in BBN and is thus incomplete. The right figure shows the results of a detailed analysis on the effects of R-hadrons in nuclei formation during BBN [75]. Here Y_X is the ratio of the R-hadron number density to the baryon number density and the R-hadron mass is assumed to be much greater than the nucleon mass. Typical thermal relic abundances correspond to $Y_X \approx 10^{-8}$.

2.3 SUSY Long-Lived Colored Particles

Several classes of SUSY models yield colored LLPs and their collider and cosmological consequences are discussed below. In split supersymmetry the gluino must tunnel through extremely massive squarks to decay and becomes long-lived. In gauge mediated supersymmetry breaking, the gravitino may be so light as to produce a sufficiently long-lived NLSP. Finally in SUSY models that violate R-parity, a colored LSP would also meet the criteria.

Generically, any colored LLP would have several cosmological consequences, regardless of other constraints on the model that produced it. Most stringent are the big bang nucleosynthesis (BBN) constraints [75]. If the R-hadron had a lifetime $\tau \gtrsim 30\,\mathrm{sec}$ it would be present during nuclei formation and t would greatly affect the isotopic ratios by catalyzing certain nuclear reactions. These results depend very weakly on the LLP mass in the regime $m_\chi \gg 1\,\mathrm{GeV}$ and favor a LLP lifetime $\tau < 30\,\mathrm{sec}$.

2.3.1 Split-SUSY: Abandoning Naturalness

While seemingly innocuous, requiring SUSY to stabilize the Higgs mass causes phenomenological problems such as proton decay, flavor changing neutral currents, and large electron and neutron dipole moments. Furthermore, several precision measurements from B-physics and g-2, would receive detectably large enhancements from standard low-energy SUSY [80]. Each of these problems can be dealt with by tuning SUSY parameters, however one can deal with all of them by elevating the fermions' superpartners to a scale much higher than the electroweak, which is exactly what happens in split-SUSY. Since the gauginos and higgsinos remain near the TeV-scale, the coupling unification still occurs neatly as shown in Figure 2.1. Also, the neutralino remains an excellent candidate for dark matter.

However, since the mass gap between the fermions and their super-partners is large in split-SUSY, the Higgs mass remains fine-tuned[8]. The authors argue that its reasonable to consider that whatever mechanism[9] handles the cosmological constant, also addresses the Higgs mass, which is much smaller in comparison. Discussions of the validity of landscape-oriented arguments are beyond the scope of this dissertation, and we stick to the phenomenological and experimental consequences of this proposal. Indeed, the gluino in split-SUSY becomes unusually long-lived since it must tunnel through a squark which is now much heavier, as shown in Figure 2.4.

The gluino lifetime can be calculated from the scalar scale, m_s, as in Equation 2.32. A rigorous treatment [64] for the calculation of k found it to be approximately 4, and only to weakly depend on m_s, $m_{\tilde{g}}$ in scenarios which the ratio of the Higgs vacuum expectation values, $\tan\beta$, is 20.

$$\tau_{\tilde{g}} = k \times \left(\frac{m_s}{10^9\,\mathrm{GeV}}\right)^4 \times \left(\frac{1\,\mathrm{TeV}}{m_{\tilde{g}}}\right)^5 \mathrm{sec} \tag{2.32}$$

Gluino masses $m_{\tilde{g}} \lesssim 10\,\mathrm{TeV}$ are accessible at the LHC and could have lifetimes ranging from 10^{-6} sec to almost the age of the universe. However, strong limits

[8]Recall that with SUSY the radiative corrections are still quadratically sensitive to the sfermion masses

[9]The authors use the landscape of meta-stable vacua to fine-tune the cosmological constant

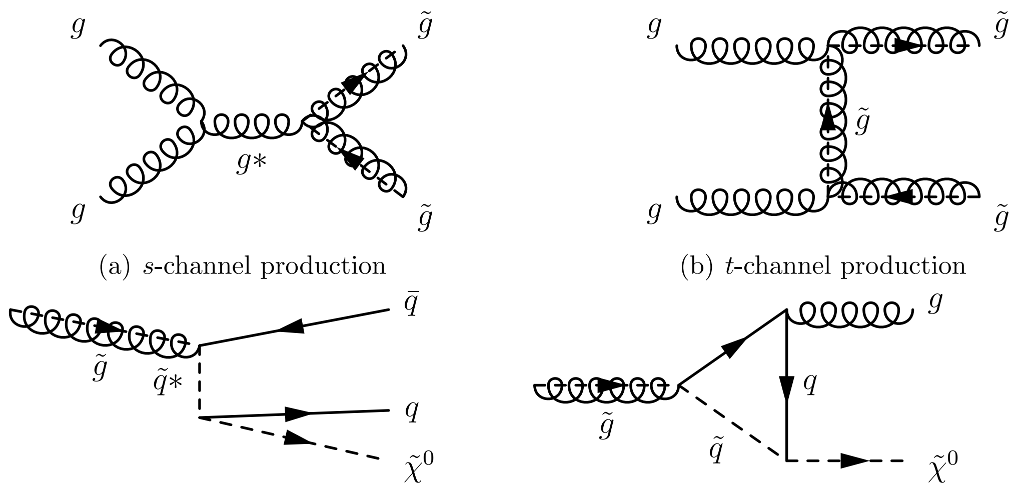

(a) s-channel production (b) t-channel production

(c) Gluino tree decay (d) Gluino loop decay

Figure 2.4: Feynman diagrams for the dominant gluino production and decay mechanisms. The production mechanisms dominant at the LHC because quarks have smaller color charge than gluons and the lack of valence antiquarks. The partial width of the loop decay approaches one as the squark mass grows.

have been placed on allowed gluino lifetimes from cosmology [28]. The requirements are show in Figure 2.3, and overall necessitate the gluino lifetime to be less than approximately 100 seconds .

2.3.2 Gravitino LSP

The gravitino, $\tilde{G}$, presents and intriguing DM candidate. Its mass and couplings are determined by $\langle F \rangle$, the SUSY breaking vev [40]. Since the NLSP can only decay to the gravitino, and those couplings are suppressed, the NLSP now becomes long-lived, as shown in Equation 2.34

$$m_{\tilde{G}} = \frac{\langle F \rangle}{\sqrt{3} m_P} \tag{2.33}$$

$$\Gamma_{\tilde{g} \to g \tilde{G}} \approx \frac{m_{\tilde{g}}^5}{48 \pi m_P^2 m_{\tilde{G}}^2} \tag{2.34}$$

In models with very light gravitinos, the NLSP decays promptly. In fact, the lightest gravitino that could produce an LSP detectable in this search ($\tau \approx 10^{-6}$ sec) has mass $m_{\tilde{G}} \gtrsim 10\,\text{keV}$. On the other side, given the center of mass energy at the LHC could produce gluinos with $m_{\tilde{g}} \approx 1\,\text{TeV}$ and this search is sensitive to particles with lifetimes $\tau \lesssim 10^{4}$ sec, a model's gravitino mass is bounded from above too, $m_{\tilde{G}} \lesssim 200\,\text{GeV}$.

While the R-hadron lifetime and cosmological density are tightly constrained, there are additional cosmological constraints from the gravitino. If one assumes early-universe thermal production and decay of SUSY particles, then the relic densities are too high and should overclose the universe. This is typically solved by fine-tuning the reheating temperature, it has been recently shown that a class of GMSB models evade this problem entirely [63].

2.3.3 R-parity Violating SUSY: Abandoning Dark Matter

Earlier, it was mentioned that a neutral LSP would be an excellent dark matter candidate, and this would favor such a neutralino or gravitino LSP[10]. However, if finding a DM candidate does not exist any sparticle may be the LSP [57]. Of course, if an electrically charged LSP were still present, it would be hard to miss in cosmology. These R-parity violating decays occur naturally in SUSY and have to be suppressed to preserve the proton lifetime. Instead of relying on the existence of a global Z_2 parity, R parity, the proton decay (which violates baryon and lepton number simultaneously) has to be stabilized by tuning various coupling constants. Luckily the couplings can be tuned such that a squark or gluino decay, violating only baryon number, without allowing proton decay. Squarks and gluinos are produced in RPV SUSY are still dominantly pair-produced, but the decays of the LSP follow Figure 2.5.

2.4 Passage of Colored Particle through Matter

The study of interactions between subatomic particles is a well studied and documented field, its results are compiled annually by the Particle Data Group [35]. Since

[10] There are strong constraints on left-handed sneutrinos, and right-handed sneutrinos would require a right-handed neutrino for which there is no current evidence.

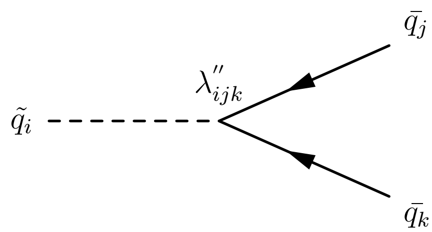

(a) RPV $\tilde{q}$ decay

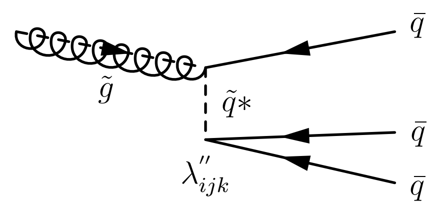

(b) RPV $\tilde{g}$ decay

Figure 2.5:

the study presented here so greatly relies on an understanding of particle-matter interactions, a few facts are discussed below. We are primarily concerned with the evolution of a stable particle (carrying color charge) as it traverses relatively dense detector. Recall that due to color confinement the new particle must pull SM quarks and gluons out of the vacuum to shield its color charge. We call the new composite particle an R-hadron, and it interacts with the detector through electromagnetic forces, primarily ionisation, and nuclear scattering.

2.4.1 Electromagnetic energy loss

When stable charged particles, like protons or muons, traverse material they lose energy due to a large number of low-energy interactions. Since there are so many electromagnetic interactions, we can approximate the process as continuous and quantify the energy loss "stopping power" as $\langle dE/dx \rangle$. Stopping power is the expected energy loss per centimeter divided by the material density.

The stopping power is modest even in lead: $\frac{dE}{dx} \approx 1\,\text{GeV/m}$ for $\beta\gamma > 1$. However, for $0.05 \lesssim \beta\gamma < 1$, the stopping power grows like β^{-2}, reaching values, 100 times larger. This means that muons with momenta greater than 1 GeV mostly traverse the ATLAS detector. R-hadrons come to rest more readily than stopping muons, due to the low production velocity at threshold. Most muons, and other long-lived SM particles, are produced from the decays of heavier particles such J/Ψ or Z which imparts them with kinetic energy many times their mass. Gluinos, and other heavy colored particles, are typically produced near threshold giving them a $\beta\gamma \approx 1$. Thus the massive particles are losing energy significantly faster, but have much more kinetic

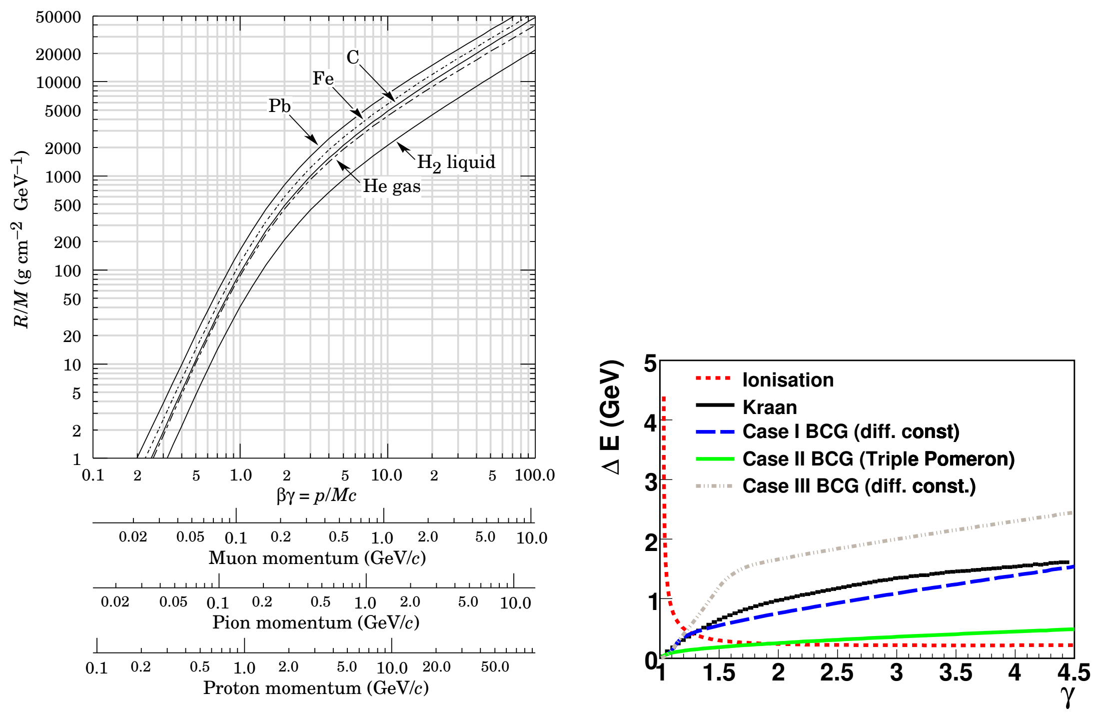

(a) Material stopping range (b) R-hadron Hadronic energy loss

Figure 2.6: Figure 2.6(a) shows the stopping range of various materials when only electromagnetic ionisation and atomic excitation are considered [91]. Figure 2.6(b) shows typical R-hadron energy loss per nuclear scatter for various models [60].

energy to lose before coming to rest.

The full expression for stopping power is given in *Passage of particles through matter* [91]. It can be integrated in the "continuous slowing down approximation", to find the range, r, of a particle with incident $\beta\gamma$, as shown in Figure 2.6(a). For example, an R-hadron of mass and momentum 250 GeV would require $r/m = 70\,\frac{\mathrm{g}}{\mathrm{cm^2 GeV}}$, or $r = \frac{19.4}{m}$ in iron, to stop. For $\beta\gamma \lesssim 1$, the following expression describes the stopping ranges in iron.

$$\frac{\rho \mathrm{r}}{\mathrm{m}}\frac{\mathrm{cm}}{\mathrm{GeV}} \approx 100\,(\beta_i\gamma_i)^{3.3} \tag{2.35}$$

The factor of 100 varies by less than 50% for most solids and liquids. This implies that for heavier R-hadrons, a smaller fraction can be stopped in a fixed amount of ATLAS detector. If we approximate ATLAS as a 3 m thick iron block, then a R-hadron of 100 GeV mass must be traveling with $\beta \lesssim 0.15$ to stop, and an R-hadron of 1 TeV mass would stop for $\beta \lesssim 0.08$. The phase space enhancement in the matrix element favors high momenta outgoing particles, and therefore many particles pass these requirements. The possibility for nuclear interactions introduces new complexity.

2.4.2 Nuclear scattering

The interaction between colored (of course shielded) particles and the material nuclei is extremely complex. A 100 GeV neutron loses very little energy until it strikes a nucleus; then both it and the nucleus initiate a hadronic shower resulting in many new neutrons, pions and others. Eventually, the collisions between the shower particles and nuclei have too little energy to generate new showers. The neutrons slowly lose energy to the nuclei through a *veritable cornucopia* of elastic and inelastic processes until they are either captured or undergo beta-decay[11]. The capturing nucleus often emits gamma radiation as it settles into a lower state of energy.

While studying R-hadrons, the mass of the new stable particle is assumed to be much larger than hadron binding energy, allowing it to be safely ignored during

[11] The neutron lifetime is almost 15 minutes, so beta-decay is common only in very low density systems like a vacuum.

nuclear interactions[12] When the R-hadron is energetic enough to initiate hadronic showers, it may also exchange quarks with the nuclei. Since the new massive colored particle carries most of the momentum, it continues nearly unaffected by the nuclear collision as seen in Figure 2.6(b). The exchange of quarks, means the R-hadron also changes charge, strangeness and baryon number during collisions. When the charge changes, possibly becoming doubly- or singly-charged or neutral, the electromagnetic energy loss changes correspondingly. Thus even relatively slow neutral particles traverse most of the detector uninhibited. This means the fraction of R-hadrons that stop is sensitive to the spectrum of allowed hadronic states, and extremely sensitive to the lowest state in which it presumably spends most of its time. The specific models used to describe the R-hadron nuclear cross section and spectrum of states is discussed in Section 6.

[12]Note that the Compton wavelength of the gluino is $\lambda = \frac{\hbar c}{m}$, which is two to three orders of magnitude smaller than the proton charge radius $\approx 1\,\mathrm{fm}$.

Chapter 3

Analysis Overview

3.1 Signatures of Long Lived Colored Particles

3.2 Experimental setup

The ATLAS detector [4] covers almost the whole solid angle point with layers of tracking detectors, calorimeters and muon chambers. It has been designed to study a wide range of physics topics at LHC energies [15]. For the measurements presented in this note, the calorimeters and muon system are of particular importance.

High granularity liquid-argon calorimeter (LAr) electromagnetic sampling calorimeters, with excellent energy and position resolution, cover the pseudo-rapidity range $|\eta| < 3.2$. The hadronic calorimetry in the range $|\eta| < 1.7$ is provided by a scintillator-tile calorimeter, which is separated into a large barrel and two smaller extended barrel cylinders, situated on either side of the central barrel. In the end-caps $|\eta| > 1.5$, LAr technology is used for the hadronic calorimeters, extending the outer $|\eta|$ limits of the end-cap electromagnetic calorimeters. The LAr forward calorimeters provide both electromagnetic and hadronic energy measurements, and extend the coverage to $|\eta| = 4.9$.

Jets are reconstructed using the infra-red and collinear-safe anti-k_T jet algorithm [39] at the EM scale with a distance parameter (η-ϕ space)[1] set to R = 0.4.

[1]The ATLAS reference system is a Cartesian right-handed coordinate system, with nominal

The inputs to the jet algorithm in collision data samples are energy depositions in the calorimeter clusters, and the minimum jet p_T is 7 GeV. ATLAS jet reconstruction algorithms are described in more detail elsewhere [87]. Missing transverse momentum (MET) is calculated using the standard tool "MET_RefFinal" (only events without muons will be used in the search region).

The ATLAS muon spectrometer [4], designed to detect tracks over pseudo-rapidity region $|\eta| < 2.7$, is made of a large toroidal magnet (with an average magnetic field of 0.5 Tesla) and consists of four types of detectors, each using a different technology. It has one barrel regions (BR) and two endcap regionss (ERs). Monitored drift tubes (MDT) in both the BR and ER sections and cathode strip chamber (CSC) are used as precision chambers, whereas resistive plate chambers (RPCs) in the BR and thin gap chamber (TGC) in the ER are used as trigger chambers. The chambers are arranged in three layers, so particles traverse up to three stations with a lever arm of several meters.

The ATLAS detector has a three-level trigger system: Level 1 (L1), Level 2 (L2), and the Event Filter (EF). For this study, the trigger relies on the jet triggers from the calorimeter which fire during an empty bunch crossing.

3.3 Triggering Strategy

We trigger on the energy the signal deposits in the calorimeter. For an R-hadron with a mass of 400 GeV and a 100 GeV neutralino, roughly 200 GeV of energy is typically deposited during the decay to jets (the rest being carried away by a neutralino). The novel approach to isolating these events is that we require that the jet trigger during time buckets in which a pp collision is very unlikely to occur, because the crossing accelerator bunches are not filled with protons. In 2011 and 2012, RF buckets that were typically filled with $> 10^{11}$ protons. Unfilled buckets could contain some protons due to diffusion from neighboring filled buckets, but this was typically $< 10^8$ protons

collision point at the origin. The anti-clockwise beam direction defines the positive z-axis, with the x-axis pointing to the center of the LHC ring. The pseudo-rapidity is defined as η = -ln(tan($\theta/2$), where the polar angle θ is taken with respect to the positive z direction.

per slot [66, 29]. Since this environment is almost entirely free from the usual pp collision backgrounds, it permits a low trigger threshold on the jet energy, without suffering from a large prescale factor.

There are numerous RF buckets of the LHC orbit in which no pp collisions occur. There are periods of only empty buckets between bunch trains, and also three abort gaps which never contain filled buckets. These gaps have lengths of 0.2 μs, 1 μs and 3 μs, and in total account for approximately 20% of the LHC orbit. We use information from the beam position and timing monitors (BPTX), collected at the beginning of a beam store. Once the LHC injection is complete, the BPTX identify all the filled and unpaired bunches [82]. ATLAS assigns each bunch crossing to a specific category ("filled", "empty", "unpaired", etc.). During data-taking, the Level 1 Central Trigger Processor looks up the bunch crossing categories to determine if an empty or collision trigger fired.

The L1_J10_EMPTY and L1_J30_EMPTY triggers require 10 and 30 GeV of energy (disregarding energy calibration for hadronic effects) in a L1 jet object during an empty bunch crossing, respectively. The L1 trigger rate is quite low during a standard LHC fill, around 5-20 Hz for L1_J10_EMPTY and just 1-2 Hz for L1_J30_EMPTY. But bursts of calorimeter noise can often increase the L1 rates by a factor of 10. Further rejection using the high level trigger (HLT) is required to reduce the rate to an acceptable level of <1 Hz consistently. HLT Jets are reconstructed using the anti-kT algorithm with topo-clusters at the EM scale. MET is also reconstructed (ignoring muons) using the standard HLT algorithms. The EF_j50_a4tcem_eta25_xe50_empty trigger requires at least one HLT jet with p_T >50 GeV in $|\eta| < 2.5$ and HLT MET>50 GeV in events passing L1_J30_EMPTY and runs unprescaled; it is the main signal trigger for this analysis. (A backup trigger, EF_j50_a4tcem_eta13_xe50_empty, with a 1.3 eta cut was also defined and almost always ran unprescaled as well.) A lower threshold trigger, EF_j30_a4tcem_eta13_xe30_empty, required just a 30 GeV jet and 30 GeV of MET, based on events passing L1_J10_EMPTY and was sometimes prescaled. Events from the lower threshold trigger are useful for checking back rates versus predicted rates with higher statistics. A parallel group of triggers was also defined for the first-empty (discussed in Section 4.2.4) bunch crossings, e.g.

EF_j30_a4tcem_eta13_xe30_firstempty, but were found to have too much background in the muon system to be used for this analysis.

In addition, events passing the L1_J10_UNPAIRED_ISO and L1_J10_UNPAIRED_NONISO triggers are used for studying the beam-halo background. Unpaired bunch crossings are those for which a filled bunch is going through ATLAS in one direction and an empty bunch is going in the other direction. And events passing the L1_RD1_EMPTY trigger are used to monitor the background rate of muon segments in the empty bunch crossings. These are random-triggered empty events (which are not being used for calibration by detector groups).

Chapter 4

Experimental setup

4.1 Accelerating and Colliding Protons

The LHC, operated by European Laboratory for Particle Physics (CERN) in Geneva (Switzerland), is currently the highest energy and highest luminosity proton collider in the world. Access to the decay products of particle produced in pp collisions provides a window into new processes occurring at extremely high energies. The LHC Design Report is an excellent and in-depth reference for expected running parameters, which have been typically achieved [37]. Thanks to the efforts of of CERN's extremely competent accelerator and infrastructure teams, the injection system was tuned and re-tuned during physics data-taking. This led to very large performance increases for the LHC but also meant that no single set of machine parameters covered the entire 3 years of data-taking. This dissertation discusses the general flow from the proton source to the LHC, but focuses on parameters particularly important to this analysis, specifically delivered luminosity, bunch structure and beam energy.

The LHC is situated in a 27 km circumference tunnel approximately 100 m underground. It accelerates charged particles by passing them through radiofrequency (RF) cavities precisely phased to the arrival time of the particles such that they experience a consistently attractive force along their path. Large multi-Tesla dipole magnets turn the particles through the Lorentz force forcing them into a roughly circular trajectory. The LHC relies on pre-accelerators to accelerate and condition

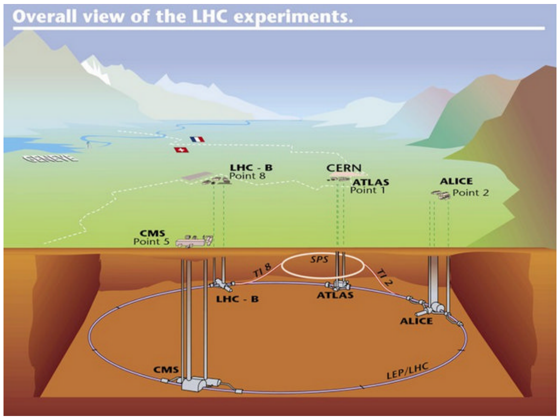

(a) Geographic overview

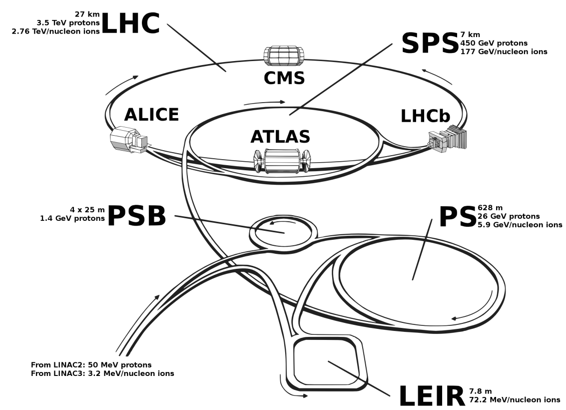

(b) Injector Chain

Figure 4.1: Figure 4.1(a) shows a geographical diagram of the LHC physical layout with large experiments indicated. Figure 4.1(b) shows the set of accelerators preparing the beam for LHC injection; this diagram is not to scale [67].

the beam of protons.

4.1.1 Injection Chain

Starting at the beginning of the injection chain, a bottle of H_2, provides one billionth of a mole of room temperature molecular hydrogen is injected into the duoplasmatron. The duoplasmatron uses thermionic electrons ejected from a cathode filament to strike the molecular hydrogen under strong electric fields. During these collisions, the atomic electrons are knocked off and the remaining protons are accelerated by a 90 kV field. The 360 mA-pulse of protons then enter a 1.75 m long radiofrequency quadrupole, further raising the energy to 750 keV, and simultaneously focusing the pulse. The 30 m Alvarez linear accelerator, as shown in Fig 4.2; this raises the energy of the protons to 50 MeV.

$$R \approx \frac{\gamma mc}{qeB} = 3.3\,\mathrm{m}\frac{\mathrm{E}\,[\mathrm{GeV}]}{q\mathrm{B}\,[\mathrm{Tesla}]} \tag{4.1}$$

The protons then pass to a set of four successively larger synchrotons—the first being the proton synchroton booster (PSB). Synchrotons accelerate charged particles in a closed, evacuated torus, by repeatedly passing them through dipole magnets

(a) Linac2 (b) Linac4

Figure 4.2: Two proton linear accelerators used at CERN. Figure 4.2(a) shows an external view of Linac2 and its support structure. Figure 4.2(b) shows a cross section view of Linac4 which will replace Linac2. The alternating conducting rings and gaps along the beam path allow non-relativistic particles to avoid decelerating forces from the RF.

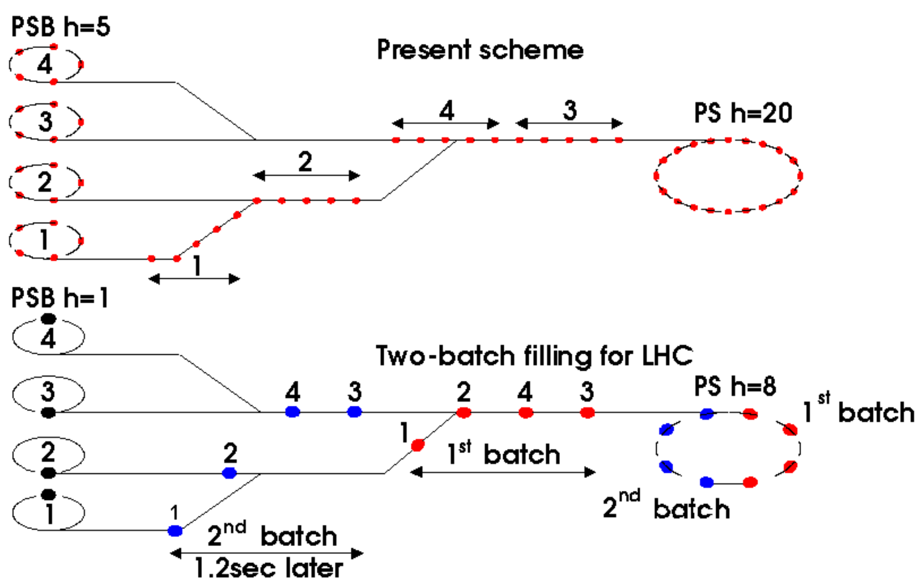

Figure 4.3: Diagram of the two-batch PS filling scheme. h is the ratio of f_{RF} to f_{rev} and represents the maximum number of bunches a ring can hold.

and RF cavities. As the energy of the particles increases the magnetic field is increased to keep the bending radius constant as in Equation 4.1. Each pass through the synchrotron loop adds little energy but many passes are achieved by increasing the magnetic field. The beam energy is typically limited by radiation losses during acceleration (cavities and dipoles) and how much energy the beam extracts from the RF system per turn. The PSB consists of four 25 m superimposed accelerating rings, each storing a single bunch. Every 1.2 seconds, the PSB passes bunches of 1.4 GeV to the PS. Space-charge effects cause large bunch growth inside the PSB, due to the slow particle speed, $0.3 < \beta < 0.7$, and many turns (10^6) they make. The LHC's requirement for high beam brightness requires the implementation of a two-batch PS filling scheme to mitigate the space-charge effects as shown in Figure 4.3.

At the end of running in 2012 the PS was being filled by a "4+2" scheme from the PSB leading to only 6 bunches in the PS at a time [69]. By slowing ramping up and down the voltage on RF systems with different frequencies (so-called RF gymnastics), the incoming six bunches are split into a total of 36. After being accelerated to 24 GeV are transferred to the super proton synchrotron (SPS) [65]. The SPS is a 7 km ring that accelerates the bunches to 450 GeV after accepting either three or four PS injections. Finally, after acceleration from the SPS the bunches passed via 2.5 km transfer lines into two beam pipes for the LHC. It takes about three minutes to fill each beam.

4.1.2 The Large Hadron Collider

The LHC performs the final acceleration and then guides the beams into collision for the experiments and through various services in the straight sections as shown in Table 4.1.

The LHC tunnel carries two beam pipes to carry protons traveling in opposite directions. The tunnel consists of eight 2.5 km arcs separated by eight 0.5 km straight sections. Each arc consists of 154 cryogenic bending dipoles operating with a turning radius of 2803.59 m. The arcs also contain a variety of other beam optics such as: vertical and horizontal quadrupoles for focusing, dipole orbit correctors, sextupoles,

Table 4.1: Short description of activities performed at each of the eight IR.

Interaction Region	Name	Activities
IR 1	ATLAS	General purpose 4π detector
IR 2	ALICE	Tracking-focused detector for Pb-Pb collisions
IR 3	Cleaning	Set of collimators to minimize stray particles
IR 4	RF	Adds energy to the beam and controls phase
IR 5	CMS	General purpose 4π detector
IR 6	Beam Dump	Executes safe removal of the beam from the LHC
IR 7	Cleaning	Set of collimators to minimize stray particles
IR 8	LHCb	One-sided detector optimized for b-hadron study

and octupoles lattice correctors. Once the SPS has filled both beams, the RF voltage is increased until the protons have either 7 TeV or 8 TeV of energy in 2010-11 and 2012 respectively. This process takes about 20 minutes and is constrained by the inability for the superconducting dipole magnets to increase current more rapidly. According to Equation 4.1, the magnetic field must transition from ≈ 0.53 T to ≈ 4.7 T (designed for 8.3 T).

The 1232 LHC main dipoles are perhaps the greatest engineering achievement in the entire complex. Each one carries almost 12,000 amps through superconducting NbTi filaments embedded in a copper matrix operating at 1.8 K. While all coolant in the tunnel is helium, it is operated at several temperatures in the gaseous, liquid and superfluid phases. The superfluid phase has the advantage of tremendous heat capacity, heat transmission and very low viscosity, making it the ideal thermal contact. A primary design concern for the LHC cryogenic and magnet system is controlling the quench rate. During a quench, part of the superconducting material transitions back to normal conduction but is still trying to pass the full current. This can be caused by material impurities, heat gain in the cryogenic system or, ironically, magnetic fields that are too large. Once the material becomes resistive again, all the helium evaporates and the cryostat pressure builds to 15-20 atmospheres.

Beam losses inside the dipole sections induce a heat load which is both costly to remove and increases the chance of a quench. A beam screen kept at 4.5 K, mitigates

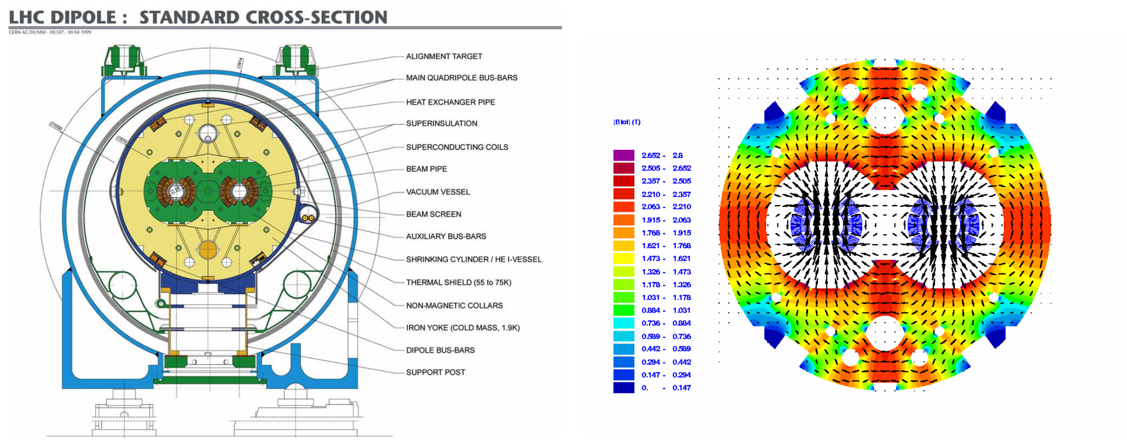

(a) Dipole cross section schematic

(b) Dipole field configuration

Figure 4.4: Figure 4.4(a) shows a cross section view of the dipole superconducting windings and support. Figure 4.4(b) shows the strength and direction of the magnetic field. The winding geometry produces a uniform field in both beam pipes.

heating from synchrotron radiation, image currents, and electron clouds. However, the beam screen cannot stop the heat load from beam-gas interactions. To prevent, proton on gas-ion scattering in the LHC, the beam pipe is kept at an astounding low pressure. The vacuum system requirements are often quoted in equivalent hydrogen gas densities, where all gases are normalized to their ionisation cross sections. Throughout the entire ring, densities must remain below 10^9 equivalent $H_2/\,cm^3$ for beam lifetime constraints. Near the experiments the density must remain below 10^7 to prevent background to physics data-taking [1].

4.1.3 Bunch Patterns

Especially important to this analysis is the exact scheme of paired and empty bunches in the LHC. Unfortunately this pattern, called the filling scheme or bunch pattern, changed frequently through 2010-2012 to cope with increasing luminosity demands. The jargon used here, specifically paired, empty and unpaired, is related but different to the same words used in the trigger system description and is discussed in detail in

[1] This background is extremely important for this particular analysis and receives an in-depth treatment in Section 8.

Section 4.2.4.

The LHC RF operates at 400 MHz which creates a so-called RF bucket every $\frac{c}{400\,\mathrm{MHz}} \approx 75\,\mathrm{cm}$, which defines the minimum possible distance between two proton bunches in stable orbit. However, due to the PS RF system, only one in every 10 buckets could be filled by design, leading to the often quoted beam crossing rate of 40 MHz and a total of 3564 possible bunch slots. Unfortunately, even empty buckets—those the SPS did not intend to put protons in—accumulate a few protons from nearby filled buckets. The occupancy of the empty slots is small but contributes to a significant source of background for this analysis. In addition to filled and empty RF buckets there are also so-called unpaired ones. These slots have a filled bunch traveling in one beam, but an empty slot in the other. They are an artifact of serving colliding bunches to all four experiments on the LHC ring, which are not symmetrically located.

To mitigate beam-beam interactions the LHC operated with extra space between paired bunches. While it was designed to operate at 25 ns bunch spacing (one paired bunch per ten RF buckets), in 2010 it operated at 150 ns and in 2011-2012 50 ns spacing.

Example 2012 Run

To clarify the complex bunch structures during the 2012 LHC operation, one specific example is examined: run 205071 with filling scheme 489. Of the total 3564 bunches in the beams, only 1368 are paired (thus deliver appreciable luminosity to ATLAS), 12 are unpaired and the remaining 2184 are considered by the LHC to be empty. Close inspection of the scheme in Figure 4.5 shows the PS and SPS effects in the LHC.

This filling scheme has a total of 38 PS segments, each with 35 filled bunches except for the very first which has 36 filled bunches. Either two or four PS trains are grouped into larger SPS with 11 empty bunches between them. The SPS trains have a larger gap of empty bunches either 38, 51 or at the end of the scheme 236. The large gap serves as the abort gap which is to slew a fast acting kicker and safely change the beam orbit in $\approx 1\mu s$. Any protons in the abort gap would experience a

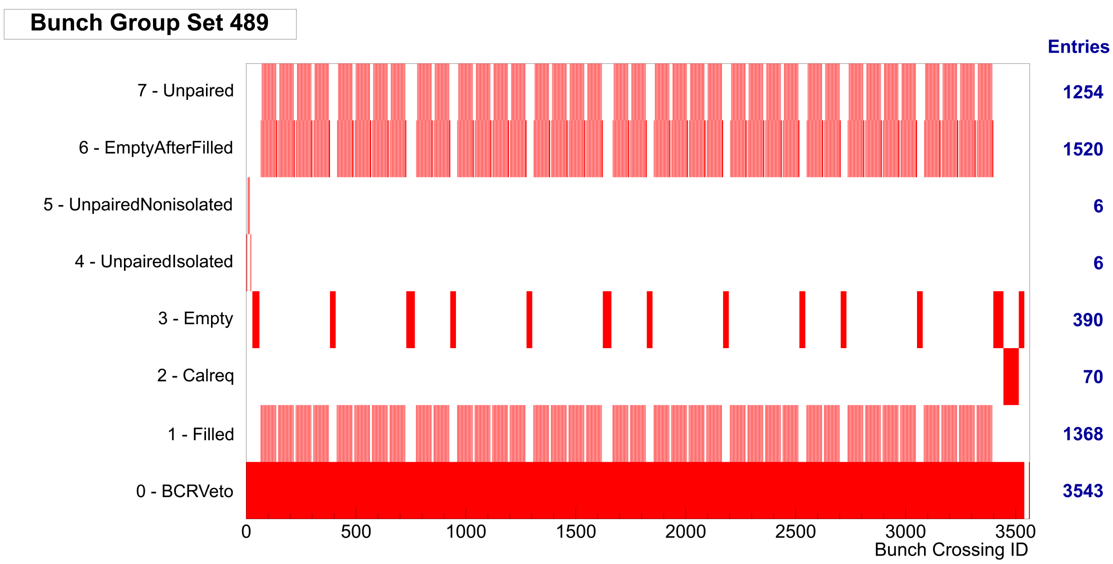

Figure 4.5: Filling scheme 489 as presented by ATLASTrigConf. This plot uses the ATLAS naming convention, so LHC-empty bunches are split into Empty, EmptyAfterFilled and CalReq. It should be noted that in 2012 **bunch group #7 (top most entry) does not indicate unpaired bunches**. This group was used to designate bunches well within the train since the jet p_T and missing momentum perform much better in that regime. Confusingly, its name does not correspond to its use in this auto generated plot.

changing field and collide with the beam pipe spraying the superconducting magnets with decay products and possibly causing a quench. The design limits for the abort gap population are $10^9 \frac{p^+}{m}$ at 7 TeV and $10^7 \frac{p^+}{m}$ at 450 GeV [2][1].

4.1.4 Collimators, Shielding and Beam Backgrounds

As the beams pass through each other—at IP1 in Figure 4.6(a)—they produce a large flux of hadronic particles traveling down the beam pipes. This radiation would induce an undesirably large heat load on the superconducting magnets [52]. A set of shields and absorbers, including the TAS absorber (19 m from the interaction point (IP))—a 1.8 m long copper block with a 17 mm bore—prevent most of the radiation from hitting the inner quadrupole triplet. However the flux is so incredibly high that that $D1$, the dipole responsible for separating the beams into two beam pipes, is operated at room temperature. This shielding that protects the magnets from ATLAS serves a dual purpose of protecting ATLAS from the radiologically-insignificant radiation that comes from beam background.

The LHC is continually performing momentum and betatron cleaning at IR3 and IR7 respectively. While the set of collimators and absorbers depicted in Figure 4.6(b) is over 99.9% efficient at capturing the particles, so-called tertiary halo still escapes down the beam pipe [52]. This physics analysis is concerned only with beam backgrounds that enter ATLAS $1\,\mathrm{m} < r < 4.25\,\mathrm{m}$ from the beam pipe. Since showers occurs when a multi-TeV proton strikes a collimator or gas molecule, the interaction products are highly boosted, and typically travel on paths deviating by $\approx 1°$ from the original proton path. For a resulting particle to strike ATLAS a meter away from the beam pipe, it must ≈ 150 m up stream and pass through the shielding discussed above. The shielding does not appear as thick to the halo particles compared to the IP1 collision products, since the halo particles are cutting through in the "wrong" direction. Furthermore, the LHC tunnel is only 2 m in diameter so some halo particles enter the earth before re-emerging in the ATLAS cavern. Both these effects strongly suppress all particles; only muons survive at a large enough rate to affect physics

[2]Recall that at 400 MHz , RF buckets occur every .75 m .

analyses.

4.2 The ATLAS Detector

ATLAS—A Toroidal LHC Apparatus—is one of four large particle detectors, each situated at a collision point on the LHC. Two of these four experiments, ALICE and LHCb, focus on a particular subset of problems, namely heavy-ion collisions and B-physics. ATLAS and its sister experiment, CMS, were designed to be most sensitive to signatures of Higgs boson decays, supersymmetry, and a wide variety of models beyond the Standard Model.

ATLAS[3] is a detector consisting of several coaxial layers of subdetectors, each performing complimentary measurements. Closest to the interaction region is the inner detector (ID), which provides consists of high-precision trackers immersed in a 2 T magnetic field. The electromagnetic and hadronic calorimeter with a total of over 20 radiation lengths and 10 (nuclear) interaction lengths, which provide excellent energy resolution and prevent hadronic punch-through. A variety of tracking technologies are employed in the muon system (MS); its extent stretching 44 m in length, 25 m in diameter, and weighing 7000 tons.

This search presented here is unusual and does not use the detector as intended. The analysis depends on just few detector systems; in fact, the entire ID, half of the muon spectrometer, the forward calorimeters, magnet system, and part of the high-level trigger do not contribute. The only noticeable difference being the amount of stopping material presented to an R-hadron as it traverses ATLAS. The LAr, tile calorimeter (TileCal), MDT and Level-1 Trigger (L1) are uniquely important.

[3] ATLAS uses a right-handed coordinate system with its origin at the nominal IP in the center of the detector and the z-axis along the beam pipe. The x-axis points from the IP to the center of the LHC ring, and the y-axis points upward. Cylindrical coordinates (r, ϕ) are used, ϕ being the azimuthal angle around the beam pipe. The pseudorapidity is defined in terms of the polar angle θ as $\eta = -\ln\tan(\theta/2)$.

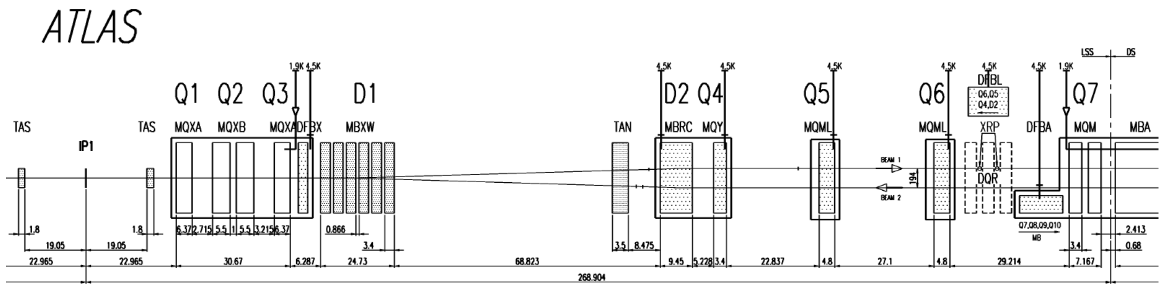

(a) IR1 Layout

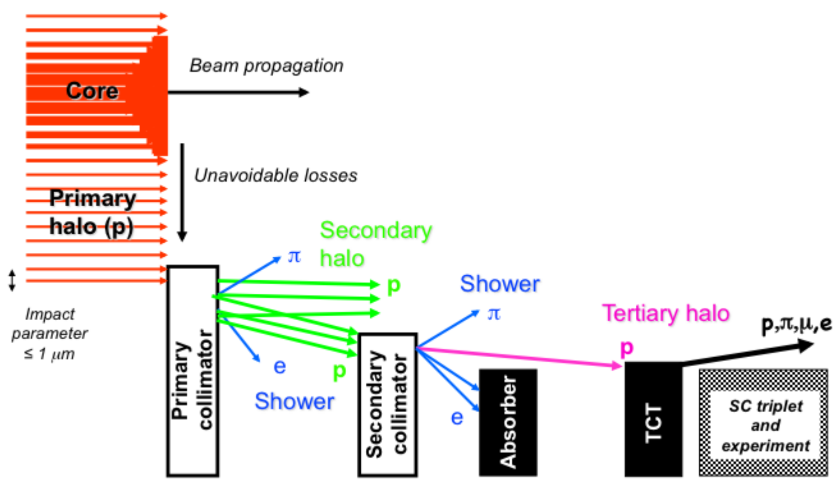

(b) Collimators

Figure 4.6: Figure 4.6(a) shows a schematic layout of the long straight section surrounding ATLAS. All distances are in meters; D denotes a dipole and Q a quadrapole [59]. The Target Collimator Tertiary (TCT) is not shown but is located between $D2$ and the target absorber for neutrals (TAN). Figure 4.6(b) shows the diagrammatic evolution of the proton beam-halo through showers and collimators to beam-induced background (or beam-halo) experienced by ATLAS [52]. The triplet in this figure refers to $Q1$, $Q2$, and $Q3$ in Figure 4.6(a).

4.2.1 Inner Detector

The ID consists of three coaxial detectors each having a barrel and two endcaps: the pixel, silicon microstrip (SCT) and transition radiation tracker (TRT), as seen in Figure 4.7. This system was designed to achieve high track momentum resolution as well as primary and secondary vertex resolution in large track multiplicity environments and a 25 ns readout. The ID has a not-insignificant amount material before the calorimeter, as seen in Figure 4.8.

The innermost component is the pixel detector, with active elements ranging from 50.5 mm to 122 mm in radius. It consists of three barrel layers and three endcaps layers on each side. Each of the 1744 pixel sensors is identical with a size of $19 \times 63\,\mathrm{mm}^2$. In turn, each sensor has 46080 individual readout channels, corresponding to a single $250\,\mu$m thick pixel $50 \times 400\,\mu\mathrm{m}^2$ in size. The radiation dose (here in 1 MeV neutron fluence) $F_{eq} \approx 10^{15}\,\mathrm{cm}^{-}2$ is so high in the pixel detector that the p-dopants eventually transition into n-type. N+ implants and oxygenated materials are employed to assure adequate charge collection efficiency after type inversion. Since this drives up cost significantly, a standard p-in-n technology is used for the SCT which has fluxes $F_{eq} \lesssim 2 \times 10^{14}\,\mathrm{cm}^{-}2$. The 15912 SCT sensors have a slightly lower intrinsic vertexing resolution $\delta R \times \delta z = 17\,\mu\mathrm{m} \times 580\,\mu\mathrm{m}$ (cf. pixel with $10\,\mu\mathrm{m} \times 115\,\mu\mathrm{m}$) but its larger radius, up to 560 mm , provide excellent additional space-points for track momentum measurement.

Both the Pixel and SCT operate with a nominal 150 V or reverse bias voltage at temperatures of $-10\,^{\circ}\mathrm{C}$ to slow the radiation damage. As the damage increases, the bias voltage is increased to counteract the loss of efficiency, possibly up to 600 V for the Pixel or 350 V for the SCT.

The TRT, which has a much lower radiation exposure, operates at room temperature as the outer tracker and is optimized for electron identification. It comprises of polyimide drift straws, filled with a 70% Argon, 27% CO_2 and 3% O_2 mixture, extending out to a radius of 1066 mm and full length of 1424.2 mm. Since each straw extends along half the barrel, the TRT is only able to measure the $R - \phi$ parameters of the track.

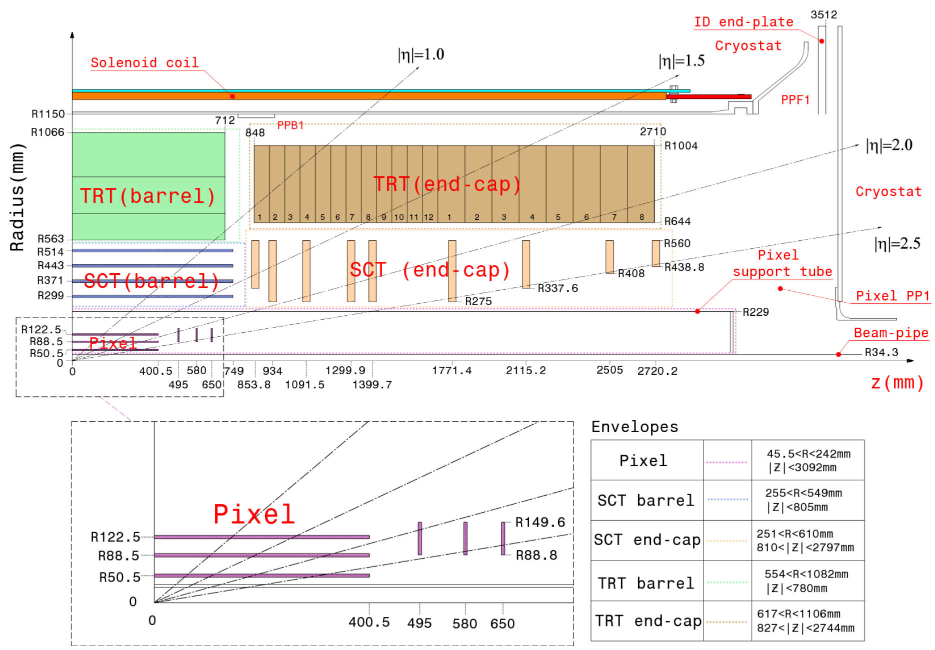

Figure 4.7: Schematic showing and r-Z view of the three trackers in the ID [4].

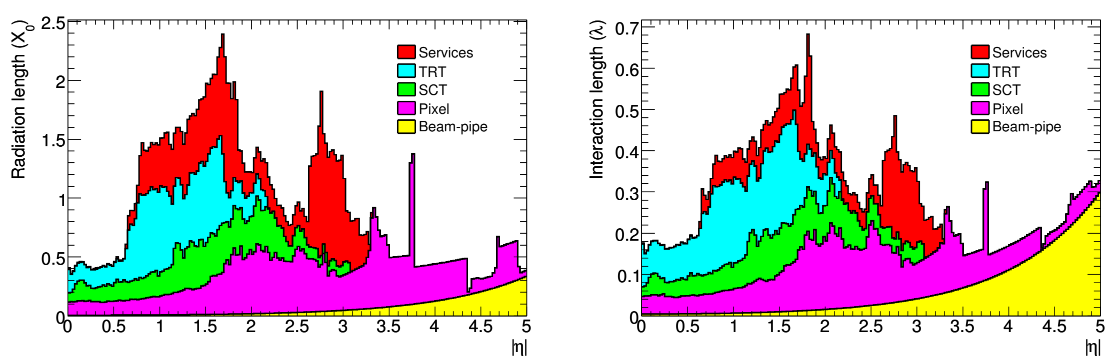

(a) Radiation lengths

(b) Nuclear Interaction lengths

Figure 4.8: The material load of the ID and its services in both electromagnetic radiation lengths (left) and nuclear interaction lengths (right) as a function of η. The solenoid adds another ≈ 0.66 radiation lengths at $\eta = 0$.

4.2.2 Calorimeters

The calorimeters serve two critical purposes in this search. Firstly, their bulk provides the primary means of stopping and trapping R-hadrons. Secondly, they provide the measurements for both triggering and measuring the energy from the R-hadron decay. To control background rates, this analysis restricts the search to the region $|\eta| < 1.2$, which excludes the forward calorimeters and extended barrel calorimeters.

Two types of sampling calorimeters are used in ATLAS to ensure good energy resolution, low punch-through, radiation hardness in a cost-effective way. The electromagnetic calorimeter and the forward calorimeters, use liquid argon as the active material due to its intrinsic radiation hardness, high energy resolution and fine segmentation [4]. The central hadronic calorimeter employs a scintillating tile with steel absorbers.

Electromagnetic Calorimeter

This liquid argon and lead sampling calorimeter (LAr) is separated into a central barrel $|\eta| < 1.475$ and two endcaps $1.375 < |\eta| < 3.2$, each contained in its own cryostat. The barrel consists of two half-barrels each 3.2 m long and $1.4\,\mathrm{m} < r < 2\,\mathrm{m}$ in radius, with a 4 mm gap between them. The total barrel weighs 114 tons and has a volume 41 m^3.

To minimize leakage from azimuthal cracks, the 1024 lead absorbing plates were built in an accordion shape with readout electrodes and drift gaps interleaved. The total drift time at nominal voltage of 2000 V in the 2.1 mm gap is 450 ns—many times longer than the bunch crossing interval of 25 ns. The LAr is divided into 3 radially separated layers with varying granularity; from inside out, they are $\Delta\eta \times \Delta\phi = 0.025/8 \times 0.1$, 0.025×0.025, and 0.05×0.025. Overall, in jets from the interaction region, the calorimeter achieves a resolution of $6\% < \frac{\sigma(p_T)}{p_T} < 9\%$ for the geometric and kinematic regions used in this analysis [11].

The LAr readout system has three primary pieces: the on-module cold calibration circuit, the front-end boards (FEBs) on the detector,but outside cryostat, and the read-out driver (ROD) located in the underground counting room 70 m away. The

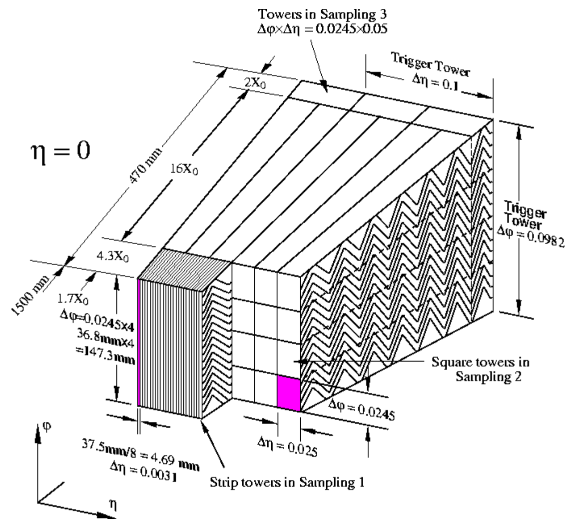

(a) LAr schematic

Figure 4.9: Schematic drawing of a azimuthal section of the LAr demonstrating its accordion structure.

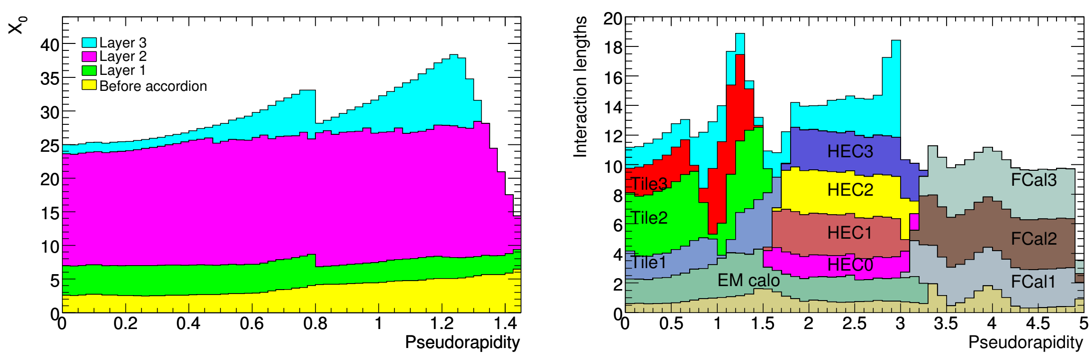

(a) LAr radiations lengths

(b) Calorimeter interactions lengths

Figure 4.10: The amount of material in and before the calorimeters as a function η. Note that the left hand plot does not show the distribution TileCal radiation lengths which is important to this analysis; it however add roughly one meter of steel.

cold circuit is primarily responsible for transmitting the photomultipiler tuber (PMT) pulse to the FEB, and injecting precise current pulses for calibration. The FEB must shape, buffer and digitize the signal, while summing and forwarding it to the hardware trigger processors described below. Additionally, the FEB also distributes the 40 MHz clock and L1 trigger accept (L1A). Interestingly, the LAr buffer is actually analog and employs 144-cell deep switched capacitor array and functions as a derandomizer[4]. If an L1A is received, then 5 samples are digitized by a 12-bit analog-to-digital converter (ADC) and optically transmitted to the ROD in the counting room. The FEB is also the first step of the analog summing of the cells into the trigger towers.

Hadronic Calorimeter

This steel and tile scintillator sampling TileCal is, similarly to the LAr, separated into a central barrel and two extended barrels (EBA, EBC) which extend to $|\eta| < 1.7$. The entire TileCal subtends the region from $2.3\,\mathrm{m} < r < 3.9\,\mathrm{m}$ from $|z| < 6.1\,\mathrm{m}$. The barrel is constructed from 64 segments each subtending $5.625\,^\circ$ azimuthally. The mechanical support girders for each of the three layers, additionally house the readout electronics and serve as the solenoid's flux return.

The scintillator—based on polystyrene—initially emits UV photons, which are converted to visible light by the PTP primary fluor and POPOP secondary fluor. A wavelength-shifting fiber collects these photons from tiles at one or two radial depths and after being grouped with other fibers, transmits the light to a dedicated PMT. Each PMT measures the light output from a cell $\Delta\eta \times \Delta\phi = 0.1 \times 0.1$ in the first two layers and 0.2×0.1 in the one farthest from the beam pipe. Readout cells in the first, second and third layer correspond to 1.5, 4.1 and 1.8 interactions lengths at $\eta = 0$, respectively.

During 2012 data-taking, the TileCal suffered from low-voltage power supply trips that affected data quality. The rate of trips was very linear with instantaneous luminosity $0.600 \pm 0.002\,\mathrm{trips} \cdot \mathrm{pb}$. During data taking these faults are automatically logged for offline analysis. Section A.3 provides a detailed look of the effect on this

[4]While the data enters the buffer in chronological order, it might not exit in the same order since the high level trigger operates in a pull orientation.

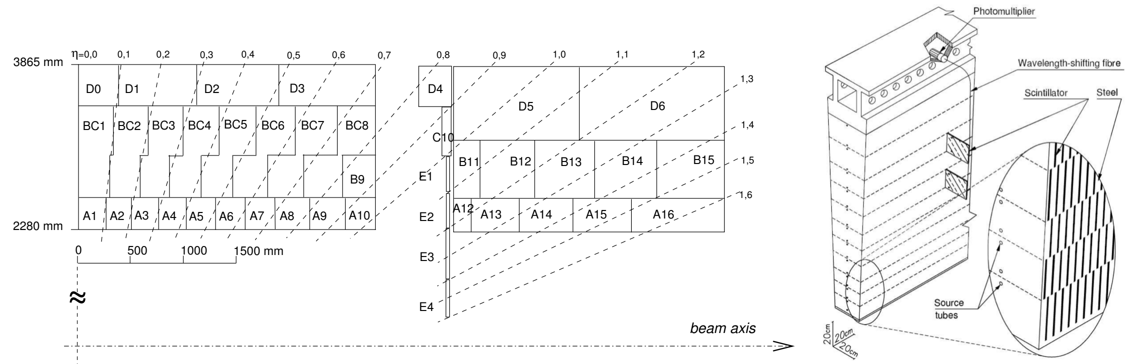

(a) Organization of TileCal readout cells (b) Single TileCal module

Figure 4.11: Layout of the TileCal. The left subfigure shows that the readout cells are designed to be projective for a particle originating from the interaction region.

analysis.

An on-detector microcontroller manages the high voltage supply of 48 individual PMTs (typically 680 V) to within 0.25 V for a nominal gain of 10^5. The front-end electronics provide single-sided signal-shaping resulting in a pulse width of 50 ns. The signal is then added in analog and forwarded to the trigger, while in parallel is digitized by a 10-bit ADC. During normal data-taking, each L1A causes the forwarding of four samples before the peak, one close to the peak and two after it (each separated by 25 ns). This provides the crucial ability to measure the energy even for decays out-of-time with the nominal bunch crossings.

4.2.3 Muon Spectrometer

The ATLAS MS consists of a set of high-precision tracking chambers and fast triggering chambers outside of the calorimeters immersed in a toroidal magnetic field of the air-core magnets. The RPCs and TGCs provide tracking coverage in the ranges $|\eta| < 1.05$ and $1.05 < |\eta| < 2.4$. In the barrel region there are three coaxially layers located at approximately $r = 5\,\mathrm{m}$, $7.5\,\mathrm{m}$, and $10\,\mathrm{m}$. There is a small gap in the chambers at $\eta = 0$ to allow services to pass. Figure 4.12 show the general MS layout.

Since this search uses no muon triggers nor muon tracks, the extra information from the RPC and TGC is not particularly useful. On the other hand, the two

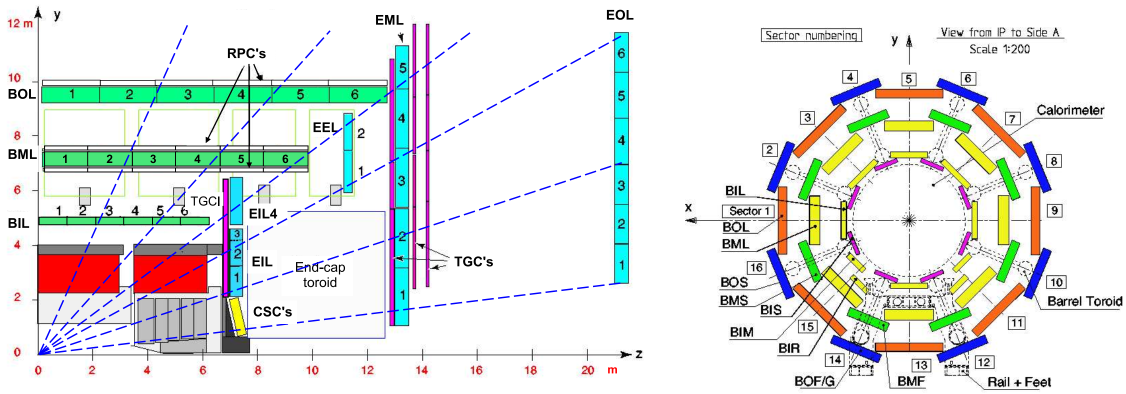

(a) MS R-z view (b) MS x-y view

Figure 4.12: Schematic view of the MS in the R-z and x-y planes. The dashed lines indicate trajectories of infinite-momentum (non-bending) particles.

precision chambers—MDT and CSC—perform a critical function of tagging muon segments. The MDT cannot sustain rates $> 150\,\mathrm{Hz/cm^2}$, and are limited to $|\eta| < 2.0$. The CSC can handle rates up to $1000\,\mathrm{Hz/cm^2}$ and extends from $2.0 < |\eta| < 2.7$ and is located only in the inner-most layer of the endcap.

Monitored Drift Chambers

Each MDT chamber, which is installed on the other side of the RPC and TGC chambers, consists of six or eight layers of Ar/CO_2 (93/7 %) filled drift tubes pressurized to 3 bar . At the center[5] of each 30 mm tube is a tungsten-rhenium $50\,\mu\mathrm{m}$ – wire at 3080 V as seen in Figure 4.13. All tubes point in the azimuthal direction, tangential at their midpoints to a circle centered on the beamline. In the barrel all tubes are identical, while in the endcap 24 different lengths are used; the smaller ones are placed closer to the beamline. To accommodate the ATLAS structural supports, several special MDT chambers were designed. These do not negatively impact the muon coverage for this analysis since nearly all muons come from the atmosphere or from the beam and penetrate the endcaps.

MDT chambers contain two sets of layers, called multi-layers, that are separated

[5]Special tube endcap connectors ensure the wire is within $\sigma < 10\,\mu\mathrm{m}$ of true center.

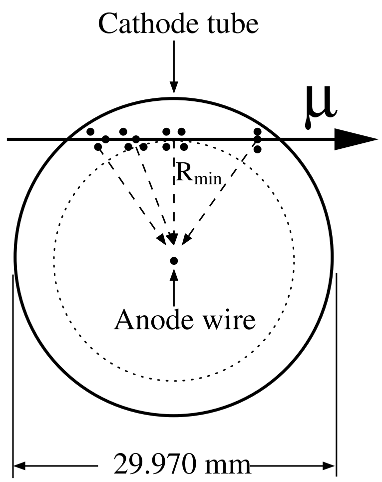

(a) Tube cross section

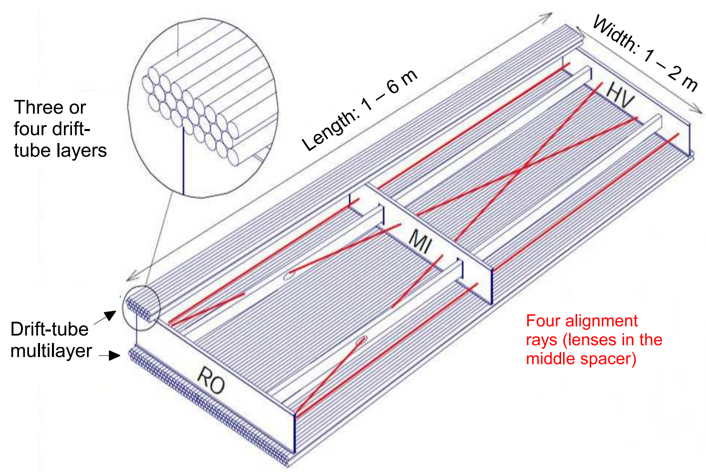

(b) Chamber Layout

Figure 4.13: The left figure is schematic of the MDT tubes showing drift circle. The right one shows the multi-layered nature of the MDT chambers.

by spacers varying in width from 6.5 mm in the inner barrel to 317 mm in the outer barrel. The multi-layer has three layers of tubes in a honeycomb pattern except for the inner barrel ones which have four layers. When a particle traverse a chamber, each of the six or eight layers provide an independent measurement of its location; η is determined by the tube position in ATLAS at ϕ by the arrival time of the pulse.

The MDT readout is accomplished by an amplifier/shaper/discriminator (ASC) which routes the output signal for eight tubes to a time-to-digital converter (TDC). The leading and trailing edges are marked in units of the TTC 40 MHz clock, with 12 bits, while each bunch-crossing interval is further subdivided by 5 bits for fine-time measurements. Additionally, the ASC measures the pulse amplitude to monitor the tube performance in real-time. Counter-intuitively, the pulse height is encoded as the trailing edge time which contains no actual timing information. The ASC uses a programmable dead-time to suppress multiple hits from the same track; it is nominally set to 750 ns . The TDC outputs are aggregated on the chamber service module (CSM) which distributes TTC signals and transmits muon hits to the L1 trigger system.

Cathode-Strip Chambers

To cope with the high rate expected in the inner layer of the forward region a different muon tracking technology is used. Unlike the MDT, the each CSC chamber is a multi-wire proportional chamber, and offers better double-track resolution and lower neutron sensitivity with an electron drift time of only 40 ns . The CSC consists of two partially overlapping rings containing eight chambers, each of which has four planes. The planes have gold-plated tungsten (3% rhenium) radial anode wires and one cathode segmented in the η direction and one in the ϕ direction. The cathodes are laminates clad with 17 μm of copper. The CSC typically provides four independent η measurements (and four more for ϕ). Similar to the LAr, the CSC employs a switch capacitor array to store the output of its amplifier and shaper. After receiving the L1A, the buffered value is digitised and transmitted via optical link to the RODs.

4.2.4 Trigger and Data Acquisition

The ATLAS trigger and data acquisition (TDAQ) system accomplishes the monumental task of buffering, analyzing, discarding and saving data. In 2012, there were 20 million bunch crossings per second, each with roughly 30 visible proton-proton interactions. Reading out all detector data at this rate would require almost 1 Petabyte/s of bandwidth, and is prohibitive for many reasons[6]. To cope with this dire situation, a sophisticated system of custom and commercial hardware and software filters and reduces the data to a manageable 1.5 Gigabytes/s .

The TDAQ system is the first point of standardization in the ATLAS dataflow and begins where the subdetectors end—the RODs. ATLAS employs one hardware level trigger (L1) and two levels of software trigger, collectively known as the HLT, containing the level two trigger (L2) and event filter (EF). Finally, the TDAQ system ends once the data is persisted on a high-capacity CERN RAID array. This analysis relies quite strongly on L1 performance and characteristics so most discussion focuses on that. The L2 and EF are discussed momentarily.

[6] The world produces only about 30 Terabytes of hard drives every second!

L1 Trigger

In 2012, the L1 trigger system reduced the rate of events to 75 kHz , and the accept command reached the front-end electronics only 2.5 μs after the corresponding bunch-crossing. However, of the 2.5 μs of allowed L1 latency, 0.5 μs is reserved for contingency and 1.0 μs is used by cable-propagation delays. To optimally exploit the available detector information in this allowed 1.0 μs a custom-hardware calorimeter (L1Calo) was built.

Central Trigger Processor Bunch Groups

There is an unfortunate clash in bunch group naming between the LHC and ATLAS. While the LHC classifies each bunch-slot crossing as paired, empty, or unpaired, ATLAS usually labels each bunch multiple ways, and some bunches not at all. For example, all bunches in BG1 are also in BG0, while in Figure 4.5 bunches #61-65 belong to no category. ATLAS uses the BPTX to determine which RF buckets are filled in either beam. The following list summarizes the definitions of various ATLAS bunch groups, while Tab. 4.2 details how they changed from 2010-2012.

BG0 *BCRVeto* Almost all bunches in the scheme. The bunches not in BCRVeto are explicitly vetoed by the central trigger processor (CTP) since its using that time to send out a "bunch-counter reset" to the front-end electronics in the TDAQ system.

BG1 *Filled* All the bunches that have a filled RF bucket in both beams. Technically a LHC-paired bunch might not be classified as filled. However, single paired bunch delivers so much luminosity that a purportedly empty or unpaired trigger with a paired bunch feeding it would quickly exceed its rate limitations and get prescaled.

BG2 *CalReq* A small set of continuous empty bunches for which no physics, hardware triggers can fire. They occur in the abort gap because of its controlled low background and are used to measure and calibrate the calorimeter performance.

BG3 *Empty* Bunch crossings without either RF bucket carrying protons. These bunches must be far enough away from any paired (but not unpaired) bunch.

BG4 *Unpaired Isolated* The bunches with one filled and one empty RF bucket that are also far enough away from paired bunches to have low collision backgrounds.

BG5 *Unpaired Non-Isolated* The bunches with one filled and one empty RF bucket that are not considered isolated as discussed above.

BG6 *First Empty* Bunch crossings without either RF bucket carrying protons. These bunches must be far enough away from any paired (but not unpaired) bunch, but the requirements are relaxed compared to the empty bunches discussed above. Bunches that are considered empty cannot be firstempty as well.

BG7 *First In Train* Introduced in 2012 this bunch group includes all the filled bunches except those at the beginning of an injection train. A filled bunch must six or more bunches away from the beginning of the train to be considered FirstInTrain. The name, from `BunchGrouper_logic.data.xml`, is a bit of a misnomer as it should be called ***Not*** *First In Train*. This group was used to avoid large calorimeter-based trigger rates coming from the unbalanced LAr-bipolar response.

Table 4.2: Components of the bunch group definitions that changed across different TDAQ releases.

Bunch Group Properties	TDAQ Release 02-00-03	03-00-01	04-00-01
Release Date	July 29 2009	Dec 2010	Jan 2012
BG6 use	EmptyAfter-Paired (unused)	FirstEmpty	FirstEmpty
BG7 use	AllUnpaired = BG4 OR BG5	Undefined and unused	FirstInTrain
TRT Front-End Polling	Group only excluded from empty[a]	Lumped into CalReq	Lumped into CalReq
TRT-FE-Polling Location	3469-3538	3469-3538	3445-3514
CalReqTileCal Location	3489-3539	3489-3539	3465-3514
Unpaired Isolation Buffer [b]	3	3	7
Empty Isolation Buffer [c]	20, 5	5, 5	5, 5
EmptyAfterPaired [d]	5, 1	0, 5	0, 5
BPTX Threshold	0^e	0^e	$\frac{0.02\times10^{11}\,p^+}{bucket}$

[a] Theoretically this means that TRT-FE-Polling could have occurred during filled-bunch data-taking, hence the change in 2011.
[b] An unpaired bunch in beam 1 (2) is considered isolated if the nearest filled bunch in beam 2 (1) is X crossings away or farther. X is the value listed.
[c] A bunch-crossing with two empty RF buckets is considered empty if the most recent paired bunch is at least X+1 crossings earlier. Additionally the next paired bunch must be more than Y crossings later. The values listed are (X,Y).
[d] If there is no bunch from $[a, a+\text{NumberOfEmpties})$ that is paired, then bunches $[a, a+\text{NumberOfTriggers})$ are labeled EmptyAfterPaired if they are not filled. Both bounds are exclusive on the upper bound. The values listed are (NumberOfEmpties, NumberOfTriggers).
[e] This threshold was actually some very low number set in the BPTX internally. In 2012, the charge in satellite bunches was too large and extra bunches were being tagged as filled before the threshold was increased.

Chapter 5

Data Samples

To acquire data potentially rich with R-hadrons, we trigger on the decay energy deposits in the calorimeter during the empty bunch crossings. For an R-hadron with a mass of 400 GeV and a 100 GeV neutralino, roughly 200 GeV of energy is typically deposited during the decay to jets (the rest being carried away by the neutralino). The novel approach to isolating these events is the requirement that the jet trigger be fired during time buckets in which a pp collision is very unlikely to occur in ATLAS because the crossing accelerator bunches are not filled with protons. In 2011 and 2012 running, LHC RF buckets that were filled typically had $> 10^{11}$ protons. Unfilled buckets could contain protons due to diffusion from filled ones, but this was typically $< 10^8$ protons per slot [66, 29]. Since this environment is almost entirely free from the usual pp collision backgrounds, it permits a low trigger threshold on the jet energy, without suffering from a large prescale factor. Due to the low background, the offline selection is relatively simple and only requires the reconstruction of jets, and muon segments.

5.1 Data Samples

A total of seven orthogonal[1] data samples are used, five of them for background estimation, one for efficiency estimation and one to search for an excess of events. Firstly, regions differ by which trigger accepted the event and then are again subdivided by what part of 2011 or 2012 they were recorded.

5.1.1 Trigger Strategy

The L1_J30_EMPTY trigger, which collects data for the search and cosmic region, requires 30 GeV of energy in a L1 jet object during an empty bunch crossing. The L1 trigger rate is quite low during a standard LHC fill, around just 1-2 Hz. But bursts of calorimeter noise can often increase the L1 rates by a factor of 10. Further rejection using the HLT is required to reduce the rate to an acceptable level of <1 Hz consistently. Jets are reconstructed using the anti-kT algorithm with topo-clusters at the EM scale. MET is also reconstructed (ignoring muons) using the standard HLT algorithms. The EF_j50_a4tcem_eta25_xe50_empty trigger requires at least one HLT jet with p_T >50 GeV in $|\eta| < 2.5$ and HLT MET>50 GeV in events passing L1_J30_EMPTY and runs unprescaled; it is the main signal trigger for this analysis[2] A lower threshold trigger, EF_j30_a4tcem_eta13_xe30_empty, required just a 30 GeV jet and 30 GeV of MET, based on events passing L1_J10_EMPTY and was sometimes prescaled. Events from the lower threshold trigger are useful for checking back rates versus predicted rates with higher statistics. A parallel group of triggers was also defined for the first-empty bunch crossings, e.g. EF_j30_a4tcem_eta13_xe30_firstempty, but were found to have too much background in the muon system to be used for this analysis. Since the L2 and event filter (EF) triggers veto few events, in this work streams and samples are typically identified by their L1 trigger.

In addition, events passing the L1_J10_UNPAIRED_ISO trigger is used for studying the beam-halo background. Unpaired bunch crossings are those for which a filled

[1] Technically the empty random and empty J10 triggers are not strictly orthogonal. Yet both rates are very low and they fire in a statistically independent way.

[2] A backup trigger, EF_j50_a4tcem_eta13_xe50_empty, with a 1.3 eta cut was also defined and almost always ran unprescaled as well.

bunch is going through ATLAS in one direction and an empty bunch is going in the other direction. And events passing the L1_RD1_EMPTY trigger are used to monitor the background rate of muon segments in the empty bunch crossings. These are random-triggered empty events (which are not being used for calibration by detector groups). Since the expected rate of events into the final search region is so small, the data volume can be managed primarily through skimming events from different streams.

5.1.2 Data Regions

Events passing the L1_J30_EMPTY signal trigger were kept in the CosmicCalo stream for 2011 data and the JetTauEtmiss stream for 2012 data. Background events passing the L1_J10_UNPAIRED trigger were kept in the JetTauEtmiss stream in 2011 and the Background stream in 2012. Background events passing the L1_RD1_EMPTY trigger were kept in the CosmicCalo stream in 2011 and 2012. For the JetTauEtmiss stream, ESDs are not saved for 2011 or 2012 data. The RPVLL_DESD selected events passing the L1 triggers of interest that have a reconstructed AntiKt4TopoEM jet with $p_T > 40$ GeV, $|\eta| < 1.3$, and $< 95\%$ of its energy in the pre-sampler (to remove noise). To further reduce the rate of events selected, only one out of 20 events with more than two muon segments (MuonBoy in 2011, Muon in 2012) was kept, since we are mainly interested in the events with no muon activity. The trigger and muon-segment-based filtering occurred during the RPVLL_DESD creation.

Events in each of the streams of interest are first required to have passed one of the L1 triggers and to pass the good runs list (GRL) selection:

```
data11_7TeV.periodAllYear_DetStatus-v60-pro10-02_DQDefects-00-01-00_PHYS_StandardGRL_All_Good_Tight.xml
data12_8TeV.periodAllYear_DetStatus-v58-pro14-01_DQDefects-00-00-33_PHYS_StandardGRL_All_Good_Tight.xml
```

The GRLs are derived from systematics assessments of data quality from offline shifters. The requirement for "All_Good" requires the entire detector is in a good state, even the sections not used in this analysis. Then the passing events are re-reconstructed [3] and saved into the RPVLL_DESD format. These data sets were finally passed through a dedicated ntuple-making package, *StoppedGluinoAnalysis*, producing a small ntuple containing only those quantities pertinent to the analysis.

[3] using 17.0.6.8 for 2011 data and 17.2.0.3 for 2012 data

The debug ESD stream was also processed. No candidates pass even the loosest offline criteria: L1_J10_EMPTY, leading jet energy above 50 GeV, and less than 6 jets.

The data used are summarized in Table 5.2, where the corresponding integrated luminosity and detector live time are provided. We select the early periods of data taking (2011 periods A–E) as a "background region" to estimate the number of expected background events (mostly from cosmic muons, as discussed below) in the data we analyze. This is motivated due to the low integrated luminosity and low number of filled bunches during these initial periods. They make up a large amount of ATLAS data taking time but relatively little luminosity. For a typical signal model we will rule out, we expect $< 3\%$ of events in the background region to arise from signal processes. As we will discuss in detail in Section 8.2, the cosmic muon background is constant in rate, but the signal rate scales with luminosity. This means that data from periods A–E in 2011 have very low signal to background ratios.

5.2 Reconstruction

Physically relevant quantities, such as jet energy, are iteratively built up from raw detector quantities such as current from a TileCal PMT. This process happens once in the L2 and EF triggers, which must perform calculations significantly faster than offline algorithms to meet the rate and latency demands. Since this analysis does not depend strongly on the high level trigger response, only the offline versions of physics objects is discussed including jets, and muon segments.

5.2.1 Jets

During particle interactions involving the production of quarks or gluons, collimated sprays of hadrons are produced. ATLAS does not try to reconstruct each individual particle for analysis, but rather their aggregate energy deposition known as a jet. The first step is to build calorimeter clusters out of calorimeter cells, which are the fundamental readout object. Clusters are seeded by searching for all cells reporting

Table 5.1: A breakdown of the data analyzed the **2010** work and the corresponding live time of the ATLAS detector during those periods. Detector live time is the sum over good luminosity blocks of the number of empty bunches times the duration of that luminosity block. The break down of 2010 data is further discussed in section **??**.

Data Period	Integrated Luminosity (pb^{-1})	Detector Live Time (bunch hours)
Period A	0.00035	240,272
Period B	0.0063	324,133
Period C	0.0071	98,917
Period D	0.25	406,701
Background	0.26	1,070,023
Period E	0.90	388,649
Period F	1.66	161,485
Control	2.56	550,134
Period G	6.57	217,373
Period H	5.93	60,567
Period I	18.16	39,288
Search	30.7	317,228
Data Sample	33.47	1,937,385

Table 5.2: The data analyzed in this work and the corresponding live time of the ATLAS detector during those periods. Detector live time is the sum over good luminosity blocks of the number of empty bunches times the duration of that luminosity block.

Data Period	Integrated Luminosity [fb^{-1}]	Hours Running	Detector Live Time [bunch hours]
2011 A	0.0000	6.08	20,548
2011 B	0.0133	19.22	51,170
2011 D	0.1855	139.03	330,504
2011 E	0.0527	24.20	46,277
Background	0.25 @ 7	188.53	448,499
2011 F	0.1593	53.95	78,478
2011 G	0.5721	158.22	17,6203
2011 H	0.2867	82.68	62,779
2011 I	0.3639	92.35	62,460
2011 J	0.2403	46.96	17,046
2011 K	0.6850	118.27	41,562
2011 L	1.5536	188.65	82,006
2011 M	1.1548	125.31	44,561
2012 A	0.9102	110.04	191,945
2012 B	5.6244	410.02	196,458
2012 C	1.5378	114.74	54,433
2012 D	3.6270	253.97	104,593
2012 E	2.8592	178.90	69,771
2012 G	1.4512	94.05	46,269
2012 H	1.6814	99.80	39,687
2012 I	1.1725	67.84	26,456
2012 J	3.0233	181.18	70,659
2012 L	1.0115	56.91	22,196
Search	5.0@7 + 22.9@8	2,433.84	1,387,562
Data Sample	5.3@7 + 22.9@8	2,622.37	1,836,061

energy at least four times their typical noise value. Next any neighboring cell, in all three dimensions, is added to this growing cluster if its energy is greater than two times its noise value. Finally, all cells with positive[4] energy are added if they are adjacent to any of the previously aggregated cells. In ATLAS, these are called "TopoClusters" since they aggregate in all three directions; they are assigned a transverse momentum, p_T, η and ϕ, and are the input to jet finding.

Clusters are next fed into a jet-finding algorithm, which attempt to group together all energy deposits coming from a fundamental particle produced in the hard scatter. This analysis uses anti-k$_T$ R=0.4 EM jets [39] which follow the standard recipe for producing a collinear and IR-safe jet definition. The algorithm picks the highest p_T object in the input list and calculates $d_{i,j}$ for each other object as defined in Equation 5.1

$$d_{i,j} = \min(p_{T,i}^{-2}, p_{T,j}^{-2}) \frac{\Delta R^2}{0.4^2} \tag{5.1}$$

If the smallest $d_{i,j}$ is less than $p_{T,i}^{-2}$ then the ith and jth objects are merged and the resulting object is put back into the input list. If the smallest $d_{i,j}$ was greater than $p_{T,i}^{-2}$ the ith object is removed from the input list and is labeled a jet. This processes is repeated until no items remains in the list. Due to energy mis-measurement intrinsic in hadronic calorimetry, jets often receive an extra calibration based on Monte Carlo studies. This analysis however always quotes energies at the electromagnetic scale without any extra hadronic calibration.

5.2.2 Muon Segments

Since the two largest backgrounds to this search involve muons traversing the muon spectrometer, an aggressive muon veto is used. Muon reconstruction typically involves clustering MS hits into roads, then segments and finally fully-fledged tracks. Segments were employed since they have a high efficiency for tagging muons not pointing to the nominal interaction point, while remaining insensitive enough to noise in the MS.

[4] Since the LAr has a bipolar pulse shape and long integration time, it occasionally reports negative energy values.

In 2011 and 12 the MuBoy segment finding algorithm was used, for which the only inputs are CSC and MDT hits; a detailed discussion can be found elsewhere [90].

Reconstructing MDT drift circles requires knowledge of when the particle passed through the tubes. During typical reconstruction the muon "t0" is forced to correspond to an LHC bunch-crossing, which is suboptimal for this analysis, which has many out-of-time muons. Thus this analysis requires access to ESD-level information, since events must be re-reconstructed using "cosmic" settings for the muon system to reconstruct muon segments with high efficiency. Cosmic muons are of course present at a random time compared to the bunch-crossing time, and beam-halo muons are in-time with proton bunches but may appear early if they hit the muon chamber before the bunch crossing (as is often the case). Using cosmic settings as part of the muon reconstruction, a fit is performed to the "t0" of the muon at each muon segment, rather than fixing it relative to the expected bunch crossing time for each chamber. Cuts on the segment direction etc. are also loosened. Example event displays of cosmic muons are shown with standard and cosmic reconstruction in Figure 5.1.

Each segment corresponds to the traversal of a charged particle across only a single MS station. MDT segments are seeded by calculating all tangent lines for each pair of hits, and requiring that it must have at least three hits with $\Delta r < 1.5\,\mathrm{mm}$. These candidates are then refit with a straight line, and extra hits are added if they would match within five times the timing uncertainty. Additionally, some hits may be dropped for quality reasons. Finally, only segment with at least four hits are considered in this analysis.

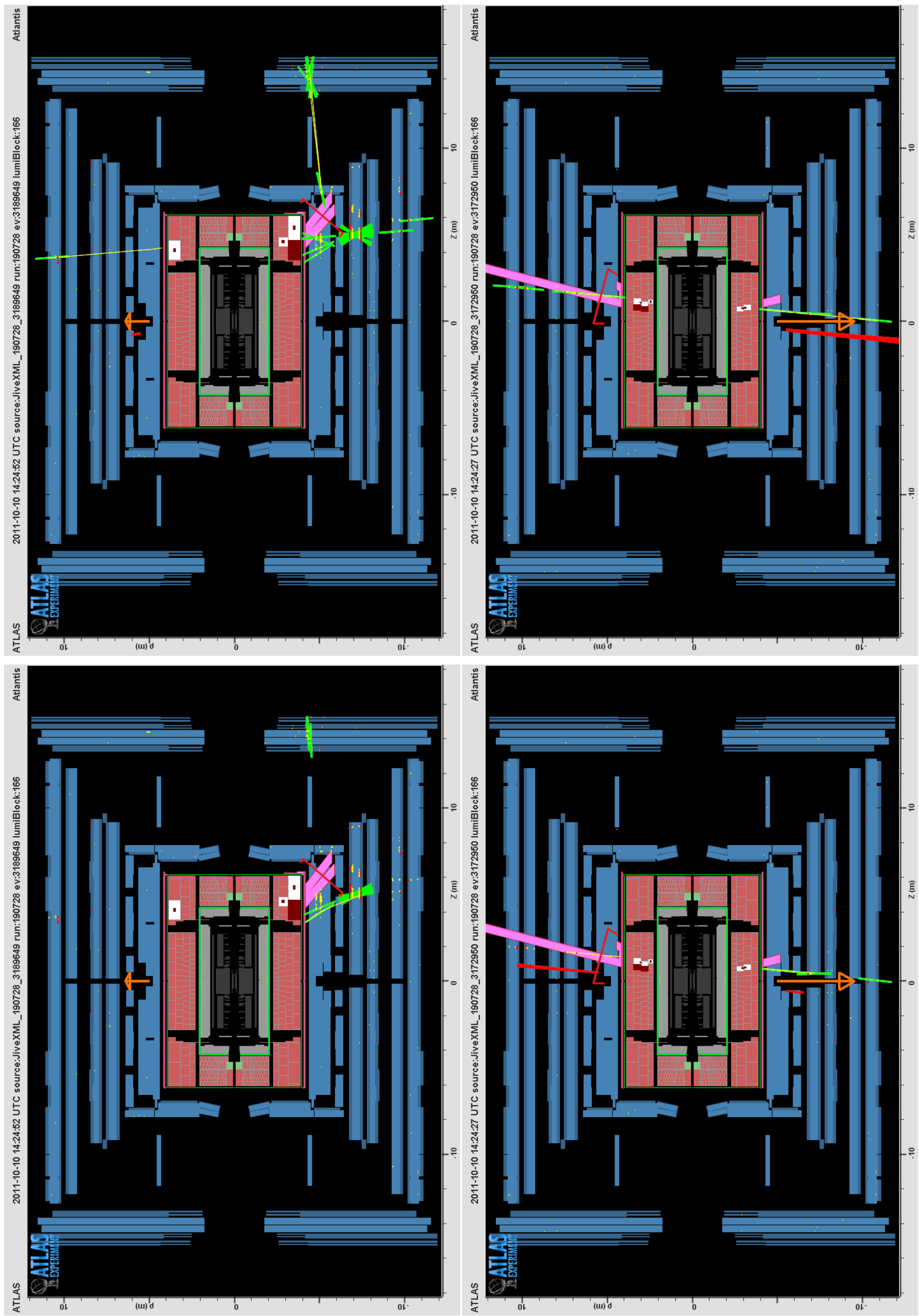

Figure 5.1: Comparison of two reconstructed cosmic muon events in data using standard reconstruction (left) and the "cosmic" reconstruction used for this analysis (right).

Chapter 6

Signal Simulation

The ATLAS simulation infrastructure is discussed in detail elsewhere [16]. The most in-depth discussion of R-hadron simulations can be found in R. Mackeprang's dissertation [76]. To correctly simulate signal events for the stopped gluino search several problems must be overcome. Due to constraints in the ATLAS simulation framework, the "stopping" and "decaying" parts of the simulation cannot be done in the same event. Therefore the simulation is broken up into two pieces which are coupled together for consistency: 1) the gluino production, R-hadronisation, and stopping and 2) the decay of the stopped R-hadron and detector response.

6.1 Gluino Production

The Pythia program [85], version 6.427, is used to simulate gluino-gluino pair production events. The string hadronisation model [25], incorporating specialized hadronisation routines [60] for R-hadrons, is used inside Pythia to produce final states containing two R-hadrons. Here, the produced gluinos are assume to have infinite lifetime. These stable gluinos are then passed to GEANT4, where a custom package simulates their propagation through ATLAS, and their interactions with the detector components. As a result, some fraction of the produced gluinos stop within the detector volume.

The cross section for gluino pair production is shown in Figure 6.1(a) as a function of gluino mass. The values in the plot (and those used in limit extraction) come from [68]. Signal cross sections are calculated to next-to-leading order in the strong coupling constant, adding the resummation of soft gluon emission at next-to-leading-logarithmic accuracy (NLO+NLL) [34, 74, 73, 32, 33]. The nominal cross section and the uncertainty are taken from an envelope of cross section predictions using different parton distribution functions (PDF) sets and factorisation and renormalisation scales, as described in Ref. [72].

Figure 6.2 shows the locations of stopped gluinos in the ATLAS detector for a sample of 1000 GeV gluinos simulated in 7 TeV center of mass *pp* collisions. Throughout this work, an R-hadron is considered stopped if it came to rest anywhere within the detector, not just the calorimeters. The stopping fractions only weakly depend on mass, and are in good agreement with expectation from theory [27]. For the simulated samples, the stopping fractions that determine the number of generated gluinos that come to rest in the detector are listed in Tables 6.1,6.2. The code which takes care of the propagation of R-hadrons through matter is stored in the Simulation/G4Extensions/R-hadrons package where two models of R-hadron interactions are included based on the cloud model defined in [78]. To compensate for the fact that R-hadron scattering is not strongly constrained by SM analogues, the simulation of R-hadron interactions in matter was handled by special GEANT4 routines based on three different scattering models with different sets of assumptions: the *generic* [71, 78], *regge* [55, 77] and *intermediate* [61] models. Each model is based on a central picture of a non-interacting heavy parton, while having different assumptions on gluino mass spectra and cross sections. The models' spectra and hadronic cross sections are listed in Tables 6.3 and 6.4. All interaction cross sections scale like (atomic number density)$^{0.7}$ and weakly depend on the R-hadron velocity. Briefly, the phenomenologies of the different models are described as follows:

Generic : Limited constraints on allowed stable states permit such occurrences as doubly charged R-hadrons and a wide variety of charge reversal scenarios. The scattering model is purely phase space driven. This model was chosen as the nominal signal model for gluino R-hadrons.

Regge : Fewer hadronic states are stable. Specifically only one (electrically neutral) baryonic state is allowed. The scattering model employs a triple-Regge formalism.

Intermediate : Most recent mass spectrum calculation in the literature. As the name implies, the spectrum is more restricted than the generic model, while still featuring charged baryon states. The scattering model used is that of the generic model.

For each case we record the locations in ATLAS where the R-hadrons stopped (if they did at all). An R-hadron would bind to a heavy nucleus of an atom in the detector, once it slows down sufficiently, and remain in place indefinitely. The nuclear potential is always attractive in the case of a heavy colored object, and there is no Fermi repulsion since the gluino has distinct quantum numbers [27].

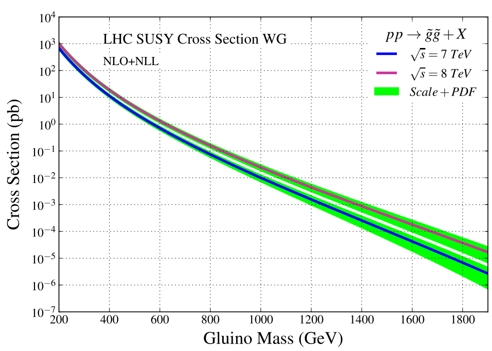

(a) Gluino Production Cross section

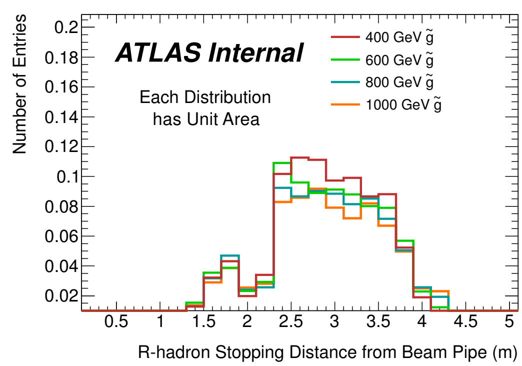

(b) R-hadron Stopping Radius

Figure 6.1: 6.1(a) Predicted cross section for $p + p \to \tilde{g} + \tilde{g} + X$ as calculated by the LHC SUSY Cross Section Working Group. The squarks were assumed to be massive enough to decouple from gluino production. 6.1(b) The stopping radii for various signal points in meters. Each plot is left unscaled.

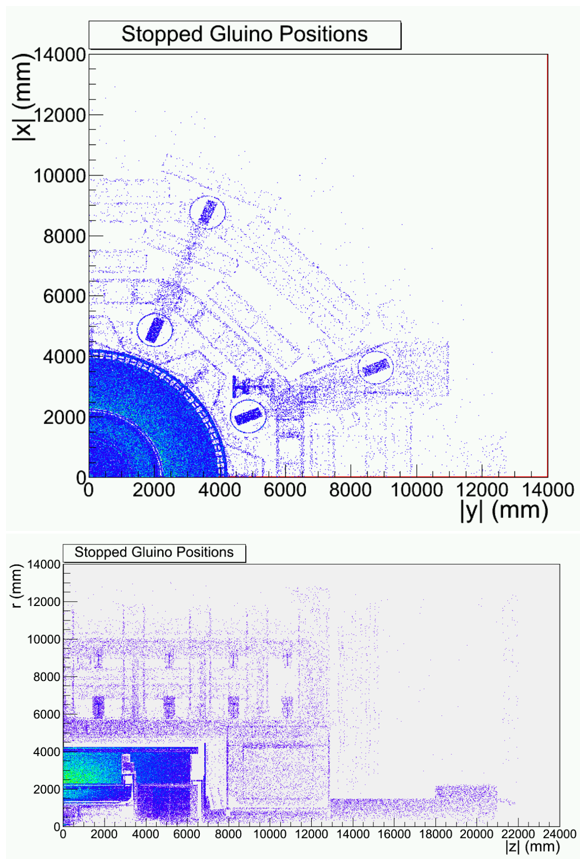

Figure 6.2: Example of stopped gluino locations in the |x|-|y| plane (left) and |r|-|z| plane (right). The gluinos predominantly come to rest in the densest materials of the detector, which in the case of ATLAS means the calorimeters.

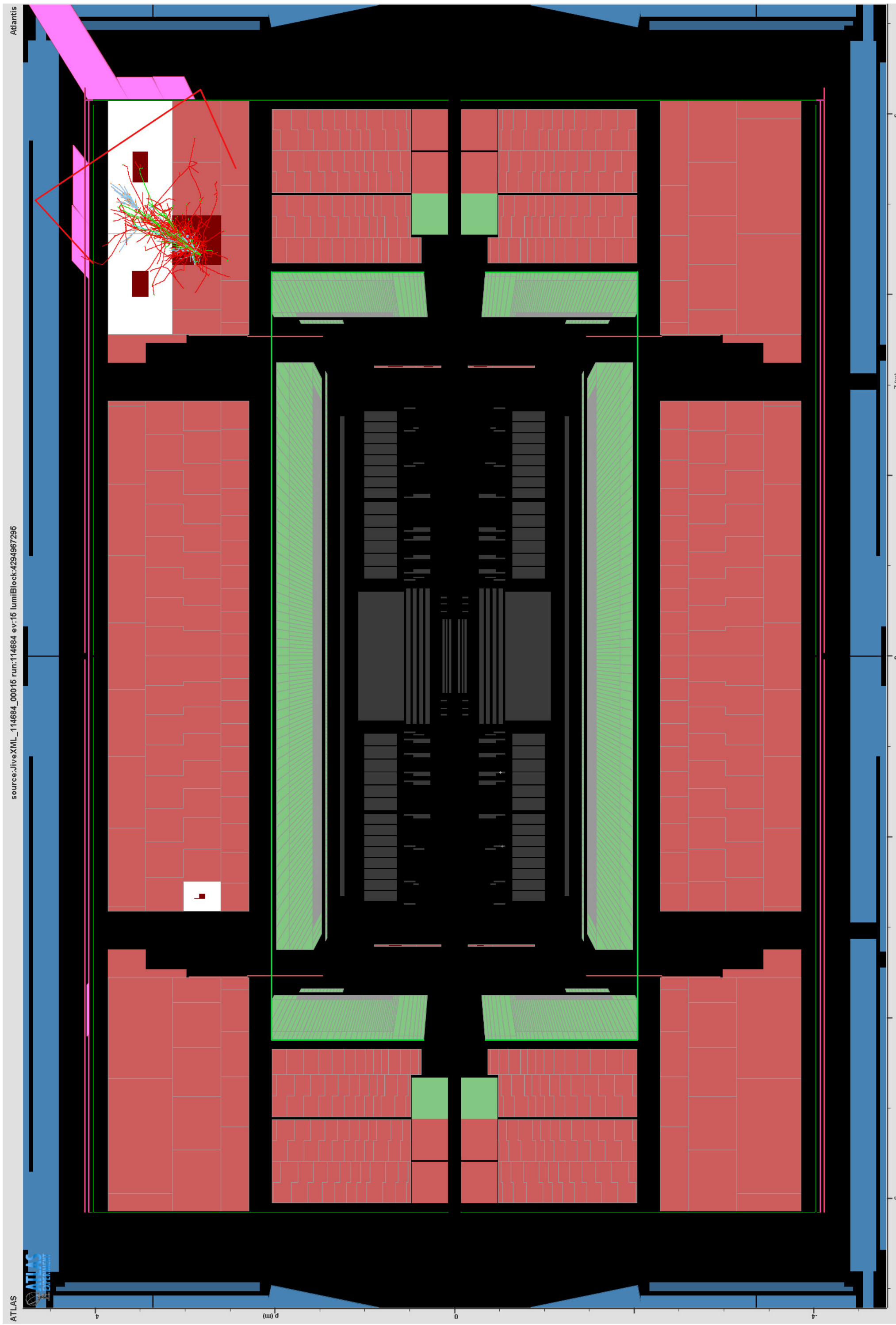

Figure 6.3: A simulated gluino decay event, showing the intermediate particles produced during the GEANT4 detector simulation.

6.2 Gluino Decay

Next, we generate *unstable* gluino R-hadrons at the stopped positions from the previous step, with a zero lifetime. These are decayed using Pythia6 and fed into a new G4 event. A random translation is applied in time, from -15 to +35 ns, relative to the bunch crossing time, since the decay of the gluino will clearly decay at a random time relative to the bunch structure of the LHC. (Later, a trigger window of 25 ns from within this 50 ns time is chosen, but the larger initial window in the simulation allows for timing studies.) The remainder of the standard simulation chain is carried out as normal, with standard ATLAS digitization and reconstruction then subsequently performed. No pile-up is added during digitization though, since we are simulating empty bunches. The effects of cavern background are included by measuring the muon activity in the random-triggered empty data (see section 10. The calorimeter activity, due to pile-up and other effects, in the random data is found to be negligible, compared to the jet energy uncertainty, and is ignored. Just 0.2% of random-triggered events have an additional jet with $p_T > 50$ GeV from noise or pile-up. Cosmic re-reconstruction and ntuple-making then follows, as is done for data. In order to model the possible parameters of the gluino stopping and decay we produce a multitude of simulation samples with a variety of different model parameters and assumptions imposed, such as varying the neutralino mass and the branching fractions of the gluino. Tables 6.1,6.2, describes the samples which have been studied. An example signal MC event is shown in Figure 6.3.

Table 6.1: Monte Carlo samples generated to study the stopped gluino signal as a function of various parameters. All samples are generated with a center-of-mass energy of 8 TeV. Those with decays to (non-top) quarks and gluons have a 50% branching ratio of each, and no top quark decays. The uncertainties on the stopping fraction are statistical only and arise from the finite number of events in the simulations.

Dataset ID	Mass (GeV) $\tilde{g}$	Mass (GeV) $\tilde{\chi}^0$	Stopping Model	Decay Modes	Stopping Fraction (%)
175240	400	100	Generic	$q\bar{q}\tilde{\chi}^0$, $g\tilde{\chi}^0$	12.2 ± 0.1
175241	600	100	Generic	$q\bar{q}\tilde{\chi}^0$, $g\tilde{\chi}^0$	
175242	800	100	Generic	$q\bar{q}\tilde{\chi}^0$, $g\tilde{\chi}^0$	
175243	1000	100	Generic	$q\bar{q}\tilde{\chi}^0$, $g\tilde{\chi}^0$	
175244	400	300	Generic	$q\bar{q}\tilde{\chi}^0$, $g\tilde{\chi}^0$	
175245	600	500	Generic	$q\bar{q}\tilde{\chi}^0$, $g\tilde{\chi}^0$	
175246	800	700	Generic	$q\bar{q}\tilde{\chi}^0$, $g\tilde{\chi}^0$	
175247	1000	900	Generic	$q\bar{q}\tilde{\chi}^0$, $g\tilde{\chi}^0$	
175248	400	100	Generic	$t\bar{t}\tilde{\chi}^0$	
175249	600	100	Generic	$t\bar{t}\tilde{\chi}^0$	
175250	800	100	Generic	$t\bar{t}\tilde{\chi}^0$	
175251	1000	100	Generic	$t\bar{t}\tilde{\chi}^0$	
175252	400	20	Generic	$t\bar{t}\tilde{\chi}^0$	
175253	600	220	Generic	$t\bar{t}\tilde{\chi}^0$	
175254	800	420	Generic	$t\bar{t}\tilde{\chi}^0$	
175255	1000	620	Generic	$t\bar{t}\tilde{\chi}^0$	
177023	400	100	Intermediate	$q\bar{q}\tilde{\chi}^0$, $g\tilde{\chi}^0$	7.0 ± 0.1
177024	600	100	Intermediate	$q\bar{q}\tilde{\chi}^0$, $g\tilde{\chi}^0$	
177025	800	100	Intermediate	$q\bar{q}\tilde{\chi}^0$, $g\tilde{\chi}^0$	
177026	1000	100	Intermediate	$q\bar{q}\tilde{\chi}^0$, $g\tilde{\chi}^0$	
177027	400	100	Regge	$q\bar{q}\tilde{\chi}^0$, $g\tilde{\chi}^0$	5.2 ± 0.1
177028	600	100	Regge	$q\bar{q}\tilde{\chi}^0$, $g\tilde{\chi}^0$	
177029	800	100	Regge	$q\bar{q}\tilde{\chi}^0$, $g\tilde{\chi}^0$	
177030	1000	100	Regge	$q\bar{q}\tilde{\chi}^0$, $g\tilde{\chi}^0$	

Table 6.2: Monte Carlo samples generated to study the stopped squark signal as a function of various parameters. All samples are generated with a center-of-mass energy of 8 TeV. All decays proceed via $\tilde{q} \rightarrow q\tilde{\chi}^0$. The uncertainties on the stopping fraction are statistical only and arise from the finite number of events in the simulations.

Dataset ID	Mass (GeV) $\tilde{q}$	Mass (GeV) $\tilde{\chi}^0$	Stopping Model	Squark	Stopping Fraction (%)
179365	400	100	Generic	$\tilde{t}$	10.1 ± 0.1
179366	600	100	Generic	$\tilde{t}$	
179367	800	100	Generic	$\tilde{t}$	
179368	300	100	Generic	$\tilde{t}$	
179369	400	200	Generic	$\tilde{t}$	
179370	600	400	Generic	$\tilde{t}$	
179371	800	600	Generic	$\tilde{t}$	
179372	400	150	Generic	$\tilde{t}$	
179373	400	100	Regge	$\tilde{t}$	8.1 ± 0.1
179374	600	100	Regge	$\tilde{t}$	
179375	800	100	Regge	$\tilde{t}$	
179376	300	100	Regge	$\tilde{t}$	
179377	400	100	Regge	$\tilde{b}$	5.3 ± 0.1
179378	600	100	Regge	$\tilde{b}$	
179379	800	100	Regge	$\tilde{b}$	
179380	300	100	Regge	$\tilde{b}$	
179381	400	300	Regge	$\tilde{b}$	
179382	600	500	Regge	$\tilde{b}$	
179383	800	700	Regge	$\tilde{b}$	
179384	300	200	Regge	$\tilde{b}$	

Table 6.3: The allowed hadronic resonances for various gluino R-hadrons. The simulated mass of the hadron is the bare sparticle mass plus the small shift listed below. All states are assumed to be stable. The nuclear cross section and mean free path correspond to a $\beta = 0.1$ particle traversing iron.

Sparticle	Stopping Model	Hadron	PDG Id	Mass Shift (MeV)	$\sigma_{nuclear}$ (mb)	Mean Free Path (cm)
$\tilde{g}$	Generic	$\tilde{g}g$	1000993	700	495.9	20.2
$\tilde{g}$	Generic	$\tilde{g}\rho^+$	1009213	650	495.9	20.2
$\tilde{g}$	Generic	$\tilde{g}K^{*0}$	1009313	825	371.9	26.9
$\tilde{g}$	Generic	$\tilde{g}K^{*+}$	1009323	825	371.9	26.9
$\tilde{g}$	Generic	$\tilde{g}\rho^0$	1009113	650	495.9	20.2
$\tilde{g}$	Generic	$\tilde{g}\omega$	1009223	650	495.9	20.2
$\tilde{g}$	Generic	$\tilde{g}\phi$	1009333	1800	247.9	40.3
$\tilde{g}$	Generic	$\tilde{g}\Delta^-$	1091114	975	743.8	13.4
$\tilde{g}$	Generic	$\tilde{g}\Delta^0$	1092114	975	743.8	13.4
$\tilde{g}$	Generic	$\tilde{g}\Delta^+$	1092214	975	743.8	13.4
$\tilde{g}$	Generic	$\tilde{g}\Delta^{++}$	1092224	975	743.8	13.4
$\tilde{g}$	Generic	$\tilde{g}\Sigma^{*-}$	1093114	1150	619.8	16.1
$\tilde{g}$	Generic	$\tilde{g}\Sigma^{*0}$	1093214	1150	619.8	16.1
$\tilde{g}$	Generic	$\tilde{g}\Sigma^{*+}$	1093224	1150	619.8	16.1
$\tilde{g}$	Generic	$\tilde{g}\Xi^{*-}$	1093314	1300	495.9	20.2
$\tilde{g}$	Generic	$\tilde{g}\Xi^{*0}$	1093324	1300	495.9	20.2
$\tilde{g}$	Generic	$\tilde{g}\Omega^-$	1093334	1600	371.9	26.9
$\tilde{g}$	Inter.	$\tilde{g}g$	1000991	330	495.9	20.2
$\tilde{g}$	Inter.	$\tilde{g}\pi^+$	1009211	330	495.9	20.2
$\tilde{g}$	Inter.	$\tilde{g}\pi^0$	1009111	330	495.9	20.2
$\tilde{g}$	Inter.	$\tilde{g}K^0$	1009311	460	371.9	26.9
$\tilde{g}$	Inter.	$\tilde{g}K^+$	1009321	460	371.9	26.9
$\tilde{g}$	Inter.	$\tilde{g}\Lambda^0$	1093122	280	619.8	16.1
$\tilde{g}$	Inter.	$\tilde{g}uud$	1092212	660	743.8	13.4
$\tilde{g}$	Inter.	$\tilde{g}udd$	1092112	660	743.8	13.4
$\tilde{g}$	Inter.	$\tilde{g}\Delta^+$	1092214	530	743.8	13.4
$\tilde{g}$	Inter.	$\tilde{g}\Delta^0$	1092114	530	743.8	13.4
$\tilde{g}$	Regge	$\tilde{g}g$	1000993	700	542.3	18.4
$\tilde{g}$	Regge	$\tilde{g}\rho^+$	1009213	700	542.3	18.4
$\tilde{g}$	Regge	$\tilde{g}\rho^0$	1009113	700	542.3	18.4
$\tilde{g}$	Regge	$\tilde{g}K^0$	1009313	700	542.3	18.4
$\tilde{g}$	Regge	$\tilde{g}K^+$	1009323	700	542.3	18.4
$\tilde{g}$	Regge	$\tilde{g}\Lambda^0$	1093122	700	346.6	28.9

Table 6.4: The allowed hadronic resonances for various squark R-hadrons. The simulated mass of the hadron is the bare sparticle mass plus the small shift listed below. All states are assumed to be stable. The nuclear cross section and mean free path correspond to a $\beta = 0.1$ particle traversing iron.

Sparticle	Stopping Model	Hadron	PDG Id	Mass Shift (MeV)	$\sigma_{nuclear}$ (mb)	Mean Free Path (cm)
$\tilde{b}$	Regge	$\tilde{b}\bar{d}^0$	1000512	325	426.8	23.4
$\tilde{b}$	Regge	$\tilde{b}\bar{u}^-$	1000522	325	426.8	23.4
$\tilde{b}$	Regge	$\tilde{b}ud^0$	1005211	650	231.1	43.3
$\tilde{t}$	Generic	$\tilde{t}\bar{u}^+$	1000612	325	247.9	40.3
$\tilde{t}$	Generic	$\tilde{t}\bar{d}^0$	1000622	325	247.9	40.3
$\tilde{t}$	Generic	$\tilde{t}\bar{s}^+$	1000632	500	124.0	80.7
$\tilde{t}$	Generic	$\tilde{t}dd^{10}$	1006113	650	495.9	20.2
$\tilde{t}$	Generic	$\tilde{t}ud^{0+}$	1006211	650	495.9	20.2
$\tilde{t}$	Generic	$\tilde{t}ud^{1+}$	1006213	650	495.9	20.2
$\tilde{t}$	Generic	$\tilde{t}uu^{1++}$	1006223	650	495.9	20.2
$\tilde{t}$	Generic	$\tilde{t}sd^{00}$	1006311	825	371.9	26.9
$\tilde{t}$	Generic	$\tilde{t}sd^{10}$	1006313	825	371.9	26.9
$\tilde{t}$	Generic	$\tilde{t}su^{0+}$	1006321	825	371.9	26.9
$\tilde{t}$	Generic	$\tilde{t}su^{1+}$	1006323	825	371.9	26.9
$\tilde{t}$	Generic	$\tilde{t}ss^{10}$	1006333	1000	247.9	40.3
$\tilde{t}$	Regge	$\tilde{t}\bar{u}^+$	1000612	325	426.8	23.4
$\tilde{t}$	Regge	$\tilde{t}\bar{d}^0$	1000622	325	426.8	23.4
$\tilde{t}$	Regge	$\tilde{t}ud^{0+}$	1006211	650	231.1	43.3

Chapter 7

Event Selection Criteria

First, events are required to pass tight data quality constraints which verify that all parts of the detector are operating normally, and no calorimeter noise bursts are present in the event (passed_larg_noise). The basic selection criteria imposed to isolate signal-like events from background-like events demand at least one high energy jet and no segments reconstructed in the muon system. The variables in the following discussion can be seen before the muon veto in Figures 7.1, 7.2,7.3 and Appendix A.5. In these figures, the "Cosmic" is the only scaled data-derived histogram. The agreement between the two backgrounds and data is consequence of the search region being dominated by cosmic muons after the cut on jet fraction in the Tile calorimeter. When this jet fraction selection is not applied, Figure 7.1(b), the beam-halo muon population exceeds the search region's population.

Since most of the gluino bound states are produced centrally in η we restrict ourselves to searching only in the central barrel and extended barrel of the calorimeter and require that the leading jet satisfy $|\eta| < 1.2$. In order to reject energy deposits from minimum-ionizing particles, we demand the leading jet energy be greater than 50 GeV. We allow for additional jets (up to 5 jets in total) in order to retain sensitivity to the decay mode $\tilde{g} \to q\bar{q}\chi^0$.

In order to remove events from a single, narrow spike in the calorimeter, due to noise in the electronics or data corruption, we veto events where 90% of the energy deposit of the leading jet (n90) is contained inside three or fewer cells. This n90 cut also reduces background significantly since most large energy deposits from muons in the calorimeter result from hard Bremsstrahlung photons, which create short, narrow EM showers. Large, broad, hadronic showers from deep-inelastic scattering of the muons off nuclei are far rarer. To further exploit the difference between calorimeter energy deposits from muons and the expected signal, we require the first moment of the lateral jet energy distribution (jet width) to be >0.04. Jet width is the p_T-weighted ΔR average of each constituent relative to the jet axis. The fraction of the jet's energy deposited in the tile calorimeter (JetTileFrac) must be >0.5, to reduce background from beam- halo since the LAr calorimeter has poorer coverage from the forward muon system.

The fractional missing $E_T > 0.5$ cut eliminates background from beam-gas and residual *pp* events and has minimal impact on the signal efficiencies. The requirement that there are no reconstructed charged particle tracks in the event was dropped for this update of the analysis, since no additional background was removed by the cut. Figure 9.3(b) shows that after all selection criteria are applied (but before the jet energy threshold is raised to 100 GeV). There is only a negligible amount of background with tracks. A comparison of the shapes of these variables between the background and signal data period can be seen in Figures A.5(d) and 7.2(b). Finally, we require that no muon segment be reconstructed in the event that has more than 4 "hits". Segments with small numbers of hits often originate from cavern background and pile-up, as studied in the random-triggered data. A jet energy cut of > 100 GeV defines the signal region, but lower energy jets above 50 GeV are studied as a control sample. An additional search region with jet energy > 300 GeV was proposed before un-blinding the data, for the signal points with large mass gaps. Table 7.1 presents the number of events surviving each of the imposed selection criteria. The selection efficiency from the signal Monte Carlo is presented in Tables 7.2-7.4. Appendix A.1 contains tabular cut flows for all models studied in this note.

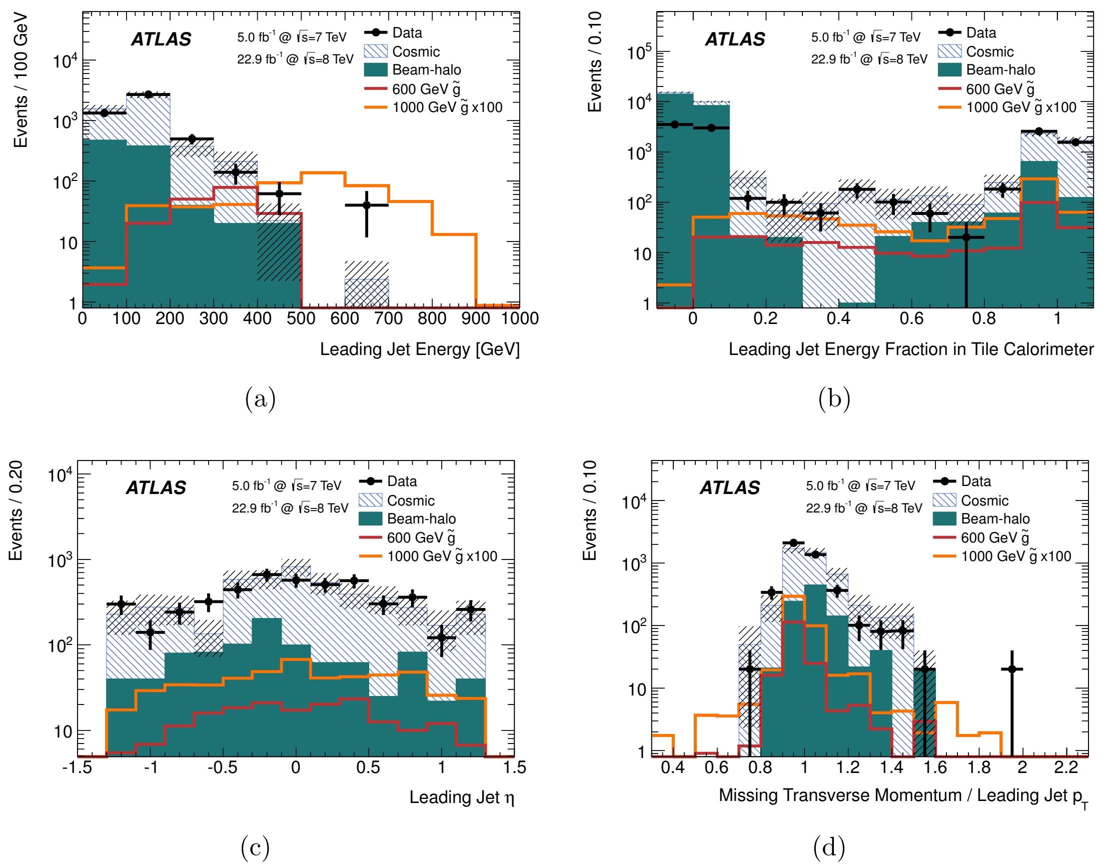

Figure 7.1: Jet variables for the empty bunch signal triggers. The requirements in Table 7.1 are applied except for jet energy > 100 GeV and the final muon veto. To remove overlap in the cosmic and beam-halo sample (which is not done in Table 7.1, an event is not considered “cosmic” if it has a halo-like segment (at least 4 hits, within 0.2 radians to the beam axis direction). For the quantity being plotted, its selection is not applied. Histograms are normalized to the expected number of events in the search region, and the uncertainty is statistical only. Some entries were affected by a DESD-filtering prescale and appear to contribute a larger than $\sqrt{N}$ uncertainty. The beam-halo and cosmic predictions are stacked on top of each other. Linear versions are show in Appendix A.5.

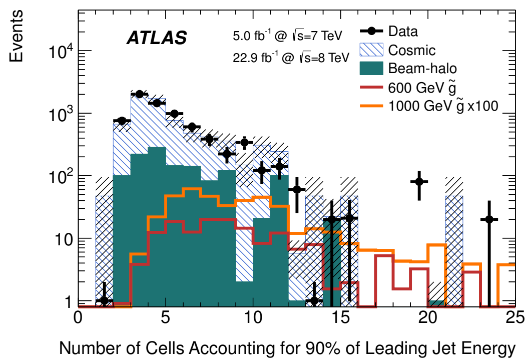

(a)

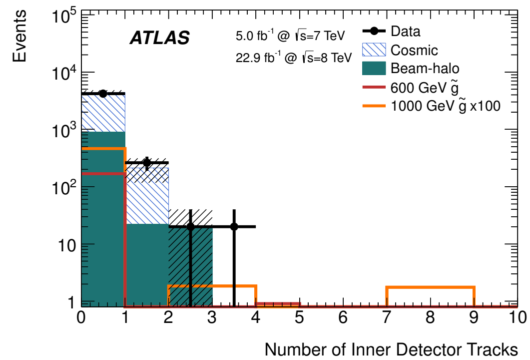

(b)

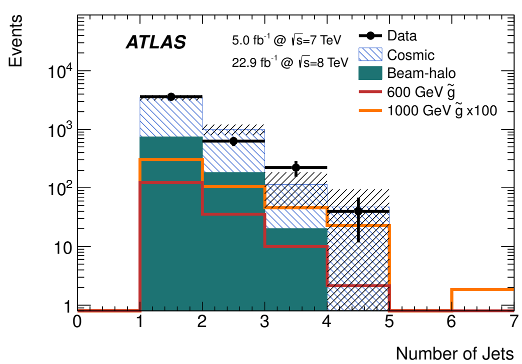

(c)

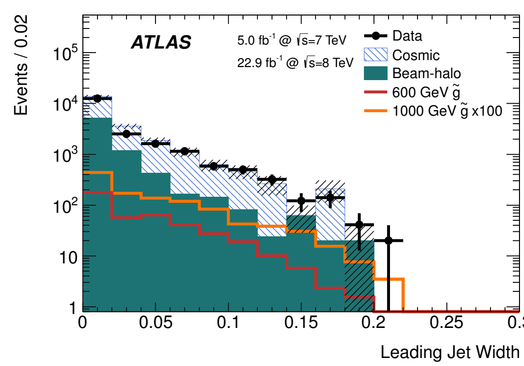

(d)

Figure 7.2: Jet variables for the empty bunch signal triggers. The requirements in Table 7.1 are applied except for jet energy > 100 GeV and the final muon veto. To remove overlap in the cosmic and beam-halo sample (which is not done in Table 7.1, an event is not considered "cosmic" if it has a halo-like segment (at least 4 hits, within .2 radians to parallel). For the quantity being plotted, its selection is not applied. Histograms are normalized to the expected number of events in the search region. The beam-halo and cosmic predictions are stacked on top of each other. Linear versions are show in Appendix A.5.

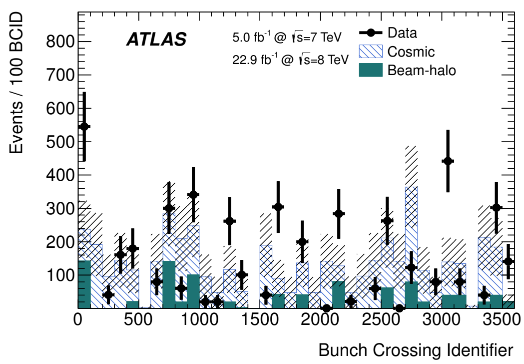

(a) Bunch Crossing Identifier (100/bin)

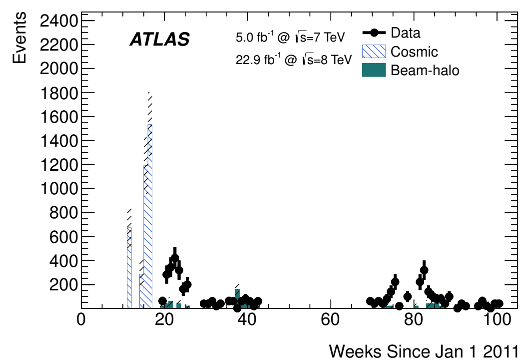

(b) Weeks Since Jan 1st 2011 GMT

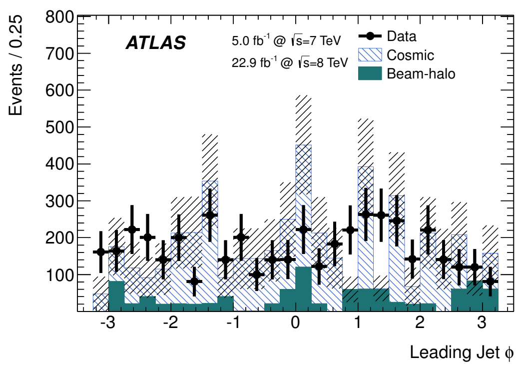

(c) Jet ϕ

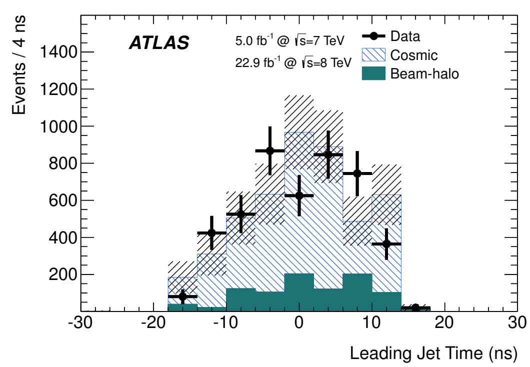

(d) Jet Time (ns)

Figure 7.3: Jet variables for the empty bunch signal triggers. The requirements in Table 7.1 are applied except for jet energy > 100 GeV and the final muon veto. To remove overlap in the cosmic and beam-halo sample (which is not done in Table 7.1, an event is not considered "cosmic" if it has a halo-like segment (at least 4 hits, within .2 radians to parallel). For the quantity being plotted, its selection is not applied. Histograms are normalized to the expected number of events in the search region. The beam-halo and cosmic predictions are stacked on top of each other.

Table 7.1: Cut flow for data in the background sample and search region sample, corresponding to those defined in Table 5.2. The background region data are shown before and after scaling (2.37) which accounts for the different detector live time and accidental muon segment veto between the background and search regions. The accidental muon segment veto occurs when a noise muon segment happens in the same event as a candidate event; it is discussed in Section 10.1. Note that the background region contains far less beam-halo events than the search region, so is mainly used for estimating the cosmic-muon background. The quoted uncertainties are statistical only. Before the muon segment veto, the uncertainties are greater than $\sqrt{N}$ due to the prescale effect from the DESD filtering.

	Regions		
Selection Criteria	Unweighted Cosmic	Weighted Cosmic	Search
Data Quality	138700 ± 1500	429200 ± 4500	799284
Trigger	49390 ± 920	152800 ± 2800	218076
abs(jeteta[0]) < 1.2	44760 ± 870	138500 ± 2700	202015
njets < 6	44690 ± 870	138300 ± 2700	201628
njets > 0	44690 ± 870	138300 ± 2700	201628
met/jetpt[0] $> .5$	44680 ± 870	138200 ± 2700	201618
passed_larg_noise	43820 ± 860	135600 ± 2700	199979
n90[0]>3	12680 ± 470	39200 ± 1500	85866
jetwidth[0]>0.04	4130 ± 260	12770 ± 810	34445
jetFracTile[0]>0.5	1640 ± 180	5070 ± 560	5396
jete[0] > 50	1640 ± 180	5070 ± 560	5396
Muon Veto	2.0 ± 1.4	4.7 ± 3.4	10
jete[0] > 100	1.0 ± 1.0	2.4 ± 2.4	5
jete[0] > 300	1.0 ± 1.0	2.4 ± 2.4	0

Table 7.2: Cut flow table for signal samples in the $\tilde{g} \to g/qq\tilde{\chi}^0$ decays. The cumulative efficiency (%) is provided for each successive cut. The samples used herein correspond to the *generic* signal MC sample as described in Section 6. The gluino mass is varied with a fixed neutralino mass of 100 GeV used in all cases. The quoted uncertainties are statistical only.

	Cumulative Efficiency (%), $m_{\tilde{\chi}^0}$ =100 GeV			
Selection Criteria	$m_{\tilde{g}}$ = 400 GeV	600 GeV	800 GeV	1000 GeV
Trigger	63.09 ± 0.71	69.10 ± 0.70	71.13 ± 0.70	73.48 ± 0.71
abs(jeteta[0]) < 1.2	55.75 ± 0.73	59.69 ± 0.74	60.52 ± 0.75	62.82 ± 0.78
njets < 6	55.75 ± 0.73	59.65 ± 0.74	60.40 ± 0.75	62.62 ± 0.78
njets > 0	55.75 ± 0.73	59.65 ± 0.74	60.40 ± 0.75	62.62 ± 0.78
met/jetpt[0] > .5	55.75 ± 0.73	59.60 ± 0.74	60.23 ± 0.75	62.38 ± 0.78
passed_larg_noise	55.75 ± 0.73	59.60 ± 0.74	60.23 ± 0.75	62.38 ± 0.78
n90[0]>3	49.09 ± 0.73	53.59 ± 0.75	54.15 ± 0.77	56.77 ± 0.79
jetwidth[0]>0.04	23.48 ± 0.62	27.36 ± 0.67	29.91 ± 0.71	31.18 ± 0.74
jetFracTile[0]>0.5	16.99 ± 0.55	19.84 ± 0.60	22.34 ± 0.64	23.04 ± 0.68
jete[0] > 50	16.99 ± 0.55	19.84 ± 0.60	22.34 ± 0.64	23.04 ± 0.68
Muon Veto	14.49 ± 0.51	15.08 ± 0.54	15.48 ± 0.56	14.75 ± 0.57
jete[0] > 100	14.06 ± 0.51	15.01 ± 0.54	15.46 ± 0.56	14.75 ± 0.57
jete[0] > 300	0.47 ± 0.10	10.61 ± 0.46	13.94 ± 0.53	14.08 ± 0.56

Table 7.3: Cut flow table for signal samples in the $\tilde{g} \to gq\bar{q}\tilde{\chi}^0$ and $\tilde{g} \to t\bar{t}\tilde{\chi}^0$ decays. The cumulative efficiency (%) is provided for each successive cut. The samples used herein correspond to the *generic* signal MC sample as described in Section 6. The gluino mass is fixed at 800 GeV in all cases. The quoted uncertainties are statistical only.

	Cumulative Efficiency (%), $m_{\tilde{g}}$ =800 GeV			
	$\tilde{g} \to g/q\bar{q}\tilde{\chi}^0$		$\tilde{g} \to t\bar{t}\tilde{\chi}^0$	
Selection Criteria	$m_{\tilde{\chi}^0}$ = 100 GeV	700 GeV	100 GeV	420 GeV
Trigger	71.13 ± 0.70	30.59 ± 0.71	72.79 ± 0.68	65.92 ± 0.71
abs(jeteta[0]) < 1.2	60.52 ± 0.75	30.59 ± 0.71	63.13 ± 0.74	57.21 ± 0.75
njets < 6	60.40 ± 0.75	30.59 ± 0.71	62.07 ± 0.75	57.01 ± 0.75
njets > 0	60.40 ± 0.75	30.59 ± 0.71	62.07 ± 0.75	57.01 ± 0.75
met/jetpt[0] > .5	60.23 ± 0.75	30.59 ± 0.71	62.07 ± 0.75	57.01 ± 0.75
passed_larg_noise	60.23 ± 0.75	30.59 ± 0.71	62.07 ± 0.75	57.01 ± 0.75
n90[0]>3	54.15 ± 0.77	24.19 ± 0.66	59.48 ± 0.75	55.35 ± 0.75
jetwidth[0]>0.04	29.91 ± 0.71	7.43 ± 0.40	29.76 ± 0.70	24.91 ± 0.65
jetFracTile[0]>0.5	22.34 ± 0.64	6.04 ± 0.37	23.04 ± 0.65	17.52 ± 0.57
jete[0] > 50	22.34 ± 0.64	6.04 ± 0.37	23.04 ± 0.65	17.52 ± 0.57
Muon Veto	15.48 ± 0.56	5.71 ± 0.36	10.08 ± 0.46	8.33 ± 0.42
jete[0] > 100	15.46 ± 0.56	4.53 ± 0.32	10.05 ± 0.46	8.28 ± 0.42
jete[0] > 300	13.94 ± 0.53	0.00 ± 0.00036	8.95 ± 0.44	4.48 ± 0.31

Table 7.4: Cut flow table for signal samples in the $\tilde{g} \rightarrow gq\bar{q}\tilde{\chi}^0$ and various R-hadron models. The cumulative efficiency (%) is provided for each successive cut. The gluino and $\tilde{\chi}^0$masses are fixed to 800 and 100 GeV respectively. The R-hadron-matter interaction models correspond to those described in Section 6. The quoted uncertainties are statistical only.

	Cumulative Efficiency (%): R-hadron models		
Selection Criteria	*Generic*	*Intermediate*	*Regge*
Trigger	71.13 ± 0.70	57.53 ± 0.70	82.86 ± 0.60
abs(jeteta[0]) < 1.2	60.52 ± 0.75	49.94 ± 0.71	74.18 ± 0.69
njets < 6	60.40 ± 0.75	49.11 ± 0.71	73.93 ± 0.69
njets > 0	60.40 ± 0.75	49.11 ± 0.71	73.93 ± 0.69
met/jetpt[0] > .5	60.23 ± 0.75	47.64 ± 0.71	73.66 ± 0.70
passed_larg_noise	60.23 ± 0.75	47.64 ± 0.71	73.66 ± 0.70
n90[0]>3	54.15 ± 0.77	44.16 ± 0.70	68.85 ± 0.73
jetwidth[0]>0.04	29.91 ± 0.71	26.76 ± 0.63	42.65 ± 0.78
jetFracTile[0]>0.5	22.34 ± 0.64	11.72 ± 0.46	26.22 ± 0.69
jete[0] > 50	22.34 ± 0.64	11.72 ± 0.46	26.22 ± 0.69
Muon Veto	15.48 ± 0.56	8.46 ± 0.39	19.46 ± 0.63
jete[0] > 100	15.46 ± 0.56	8.44 ± 0.39	19.41 ± 0.62
jete[0] > 300	13.94 ± 0.53	7.43 ± 0.37	17.21 ± 0.60

Table 7.5: The selection efficiency after all cuts have been applied for all gluino signal samples. The quoted uncertainties are statistical only.

Stopping Model	Final State Quarks	Mass (GeV) $\tilde{g}$	$\tilde{\chi}^0$	Leading Jet Threshold (GeV) 100	300
Generic	$g/q\bar{q}$	400	100	14.06 ± 0.51 %	0.47 ± 0.10 %
Generic	$g/q\bar{q}$	600	100	15.01 ± 0.54 %	10.61 ± 0.46 %
Generic	$g/q\bar{q}$	800	100	15.46 ± 0.56 %	13.94 ± 0.53 %
Generic	$g/q\bar{q}$	1000	100	14.75 ± 0.57 %	14.08 ± 0.56 %
Generic	$g/q\bar{q}$	400	300	3.38 ± 0.27 %	–
Generic	$g/q\bar{q}$	600	500	4.19 ± 0.30 %	–
Generic	$g/q\bar{q}$	800	700	4.53 ± 0.32 %	–
Generic	$g/q\bar{q}$	1000	900	5.69 ± 0.36 %	–
Generic	$t\bar{t}$	600	100	9.93 ± 0.45 %	7.24 ± 0.39 %
Generic	$t\bar{t}$	800	100	10.05 ± 0.46 %	8.95 ± 0.44 %
Generic	$t\bar{t}$	1000	100	9.49 ± 0.46 %	8.95 ± 0.44 %
Generic	$t\bar{t}$	400	20	8.66 ± 0.42 %	4.27 ± 0.30 %
Generic	$t\bar{t}$	600	220	9.78 ± 0.44 %	5.35 ± 0.34 %
Generic	$t\bar{t}$	800	420	8.28 ± 0.42 %	4.48 ± 0.31 %
Generic	$t\bar{t}$	1000	620	8.71 ± 0.43 %	4.73 ± 0.33 %
Intermediate	$g/q\bar{q}$	400	100	8.63 ± 0.40 %	0.394 ± 0.090%
Intermediate	$g/q\bar{q}$	600	100	8.93 ± 0.40 %	6.02 ± 0.34 %
Intermediate	$g/q\bar{q}$	800	100	8.44 ± 0.39 %	7.43 ± 0.37 %
Intermediate	$g/q\bar{q}$	1000	100	7.43 ± 0.38 %	6.87 ± 0.37 %
Regge	$g/q\bar{q}$	400	100	16.70 ± 0.59 %	0.66 ± 0.13 %
Regge	$g/q\bar{q}$	600	100	19.30 ± 0.63 %	13.43 ± 0.54 %
Regge	$g/q\bar{q}$	800	100	19.41 ± 0.62 %	17.21 ± 0.60 %
Regge	$g/q\bar{q}$	1000	100	19.56 ± 0.62 %	18.41 ± 0.61 %
Generic	$g/q\bar{q}$	600	560	–	–
Generic	$g/q\bar{q}$	600	540	–	–
Generic	$g/q\bar{q}$	600	520	0.320 ± 0.038%	–
Generic	$g/q\bar{q}$	600	480	7.94 ± 0.18 %	–
Generic	$g/q\bar{q}$	600	450	10.67 ± 0.21 %	–
Generic	$g/q\bar{q}$	600	400	12.96 ± 0.23 %	–
Generic	$g/q\bar{q}$	600	300	15.01 ± 0.24 %	1.554 ± 0.085%
Generic	$g/q\bar{q}$	600	200	15.59 ± 0.25 %	8.41 ± 0.19 %

Table 7.6: The selection efficiency after all cuts have been applied for all squark signal samples. Decays are always of the form $\tilde{q} \to q\tilde{\chi}^0$. The quoted uncertainties are statistical only.

Stopping Model	Squark Content	Mass (GeV) $\tilde{q}$	Mass (GeV) $\tilde{\chi}^0$	Leading Jet Threshold (GeV) 100	Leading Jet Threshold (GeV) 300
Regge	$\tilde{b}$	300	100	7.64 ± 0.41 %	–
Regge	$\tilde{b}$	400	100	10.81 ± 0.49 %	–
Regge	$\tilde{b}$	600	100	11.95 ± 0.54 %	5.85 ± 0.39 %
Regge	$\tilde{b}$	800	100	12.52 ± 0.57 %	10.50 ± 0.52 %
Regge	$\tilde{b}$	400	300	3.00 ± 0.27 %	–
Regge	$\tilde{b}$	600	500	3.96 ± 0.32 %	–
Regge	$\tilde{b}$	800	700	3.39 ± 0.31 %	–
Regge	$\tilde{b}$	300	200	1.90 ± 0.21 %	–
Regge	$\tilde{t}$	300	100	10.55 ± 0.46 %	–
Regge	$\tilde{t}$	400	100	10.21 ± 0.46 %	–
Regge	$\tilde{t}$	600	100	10.10 ± 0.47 %	4.50 ± 0.33 %
Regge	$\tilde{t}$	800	100	10.62 ± 0.49 %	8.05 ± 0.44 %
Generic	$\tilde{t}$	300	100	11.04 ± 0.46 %	–
Generic	$\tilde{t}$	400	100	10.06 ± 0.45 %	–
Generic	$\tilde{t}$	600	100	9.64 ± 0.45 %	4.58 ± 0.32 %
Generic	$\tilde{t}$	800	100	10.16 ± 0.48 %	7.68 ± 0.42 %
Generic	$\tilde{t}$	400	150	10.75 ± 0.46 %	–
Generic	$\tilde{t}$	400	200	10.94 ± 0.47 %	–
Generic	$\tilde{t}$	600	400	10.99 ± 0.48 %	–
Generic	$\tilde{t}$	800	600	10.72 ± 0.48 %	–

Chapter 8

Background Estimation

We consider several sources of backgrounds: beam-halo muons, cosmic muons, and noise in the calorimeters. Noise is assumed to be zero as assumed below, the remaining two backgrounds are estimated with sidebands. Unlike the 2010 analysis, the early, low-luminosity data is not assumed to be beam-halo free, and the contamination must be subtracted before scaling the expected cosmic by livetime. The next section describes how the beam-halo contribution is calculated for both the cosmic sideband and the search region.

8.1 Beam-halo Background

Protons in either beam can interact with residual gas in the beam pipe, or the beam pipe itself if they stray off orbit, leading to a hadronic shower. If the interaction takes place several hundred meters up beam from ATLAS, most of the shower is absorbed in shielding or surrounding material before reaching ATLAS. The muons from the shower can survive and enter the detector though, traveling parallel to the beamline and in-time with the (filled) proton bunch [30, 10]. These muons are referred to as *beam-halo*. The unpaired-bunch data with a jet passing the criteria is dominantly beam-halo; a candidate event is shown in Figure 8.1.

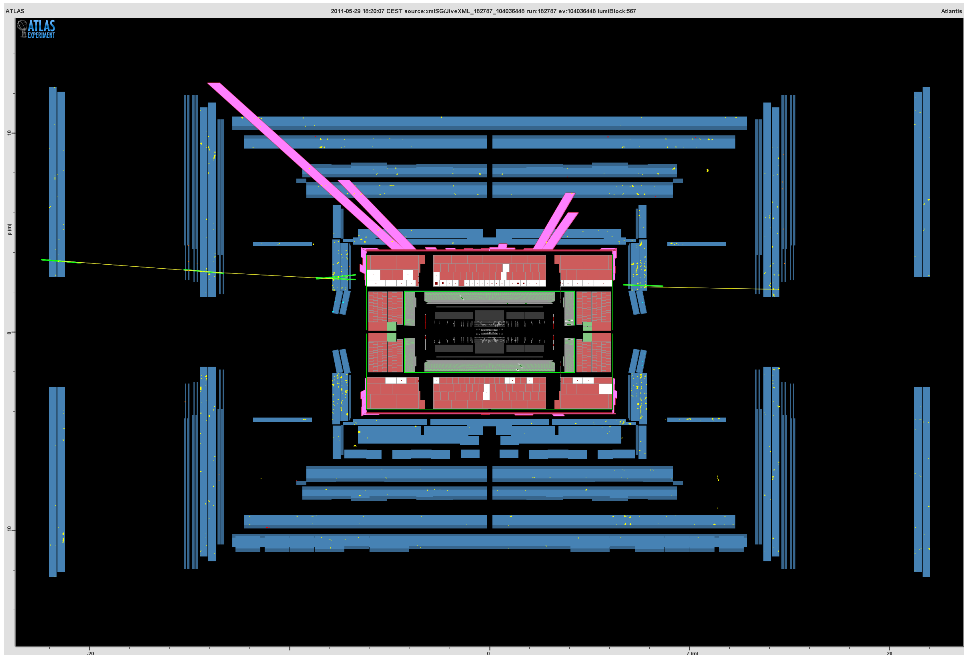

Figure 8.1: A beam-halo candidate event in the unpaired data.

To estimate the amount of beam-halo background in the search (or cosmic side-band) region's empty bunches, we use an orthogonal sample of events from the unpaired bunch crossings which pass the jet criteria. The ratio of jets without a muon segment identified to those with a muon segment is derived. This fraction is then multiplied by the number of beam-halo events observed in the empty bunches that have an identified muon segment, to estimate the number of events that should not have a muon segment and in the empty bunches. Said another way, we assume that the event properties (but not event rates) between beam-halo in the empty bunches and beam-halo in the unpaired bunches is identical. This allows us to estimate the muon spectrometers forward-segment tagging efficiency in the unpaired bunches.

First, a modified version of the standard selection criteria, as described in Table 7.1 is applied to the events from unpaired bunches. To allow for greater statistic, this version has a loosened final jet energy cut, muon segment veto, and jet cleaning. All events passing these cuts are assumed to be from a beam-halo muon if they either have a forward muon segment, or no muon segment at all[1] To estimate the fraction of events that fail to leave a muon segment (and would thus fake a signal decay) this sample is divided into the events that leave a segment nearly parallel with the beam pipe: $\theta < 0.2 || \theta > 2.9$ and have at least 4 muon station measurements and those that have no segment with at least 4 measurements. The ratio of the event yields in these two categories estimates how frequently a forward segment is missed by the MS.

Next, the number of beam-halo muons in the search region (the empty bunches) that did leave a muon segment is calculated. The same selection criteria as Table 7.1 is used, except for the final jet cut. To tag the number of forward muons in the empty bunch events, a muon segment nearly parallel to the beamline (as in step one) is required, instead of vetoing events with any segment. If, in any of these auxiliary measurements, no events are present, the uncertainty is taken as ±1 event. Finally, in addition to the final jet cut used in the search region definition, the beam-halo used either a 50 or 100 GeV jet energy threshold. The measurements with a 100 GeV beam-halo estimate were only used as a double-check, and do not contribute to the final limits. The findings are summarized in the Table 8.1 for all relevant data regions.

8.2 Cosmic Muon Background

Cosmic muons are estimated using the background region (periods A–E of 2011), accounting for possible beam-halo during the period. The beam-halo background is estimated for this cosmic data sample as above, and this estimate is subtracted from the observed events passing all selections. Finally, this number of cosmic events in the cosmic data sample is scaled according to the ratio of livetimes in the signal region / cosmic region to estimate the cosmic background in the signal region. Additionally, the cosmic background estimate is multiplied by the muon-veto efficiency (see Section 10) to account for the rejection of background caused by the muon veto.

[1] Of course there is some cosmic muon contamination in this sample too, but its extremely small compared to the rate of beam-halo muons. The sample of roughly 1000 beam-halo muons comes from only seven or so unpaired bunches, compared 600 cosmic muons from several hundred empty bunches. Furthermore the vast majority of cosmic muons that pass the jet selection leave vertical muon segments.

Table 8.1: Estimation of beam-halo events entering the search region as described in section 8.1. We calculate the fraction of beam-halo muons that do not leave a segment from the unpaired data. This fraction is then applied to the number of events in the search region where a segment was reconstructed to yield a beam-halo estimation. The bottom half of this table uses a tighter jet energy threshold to measure the muon segment veto efficiency; this is a auxiliary measurement only. The quoted uncertainties are statistical only.

1^{st} Jet	Data	Halo Jet	Unpaired		Empty	
Cut [GeV]	Region	Cut [GeV]	Parallel μ	No μ	Parallel μ^a	Pred. No μ
50	Cosmic	50	1634	22	$82 \pm 40.$	1.10 ± 0.59
50	Search	50	1634	22	900 ± 130	12.1 ± 3.2
100	Cosmic	50	1634	22	61 ± 35	0.82 ± 0.50
100	Search	50	1634	22	445 ± 94	6.0 ± 1.8
300	Cosmic	50	1634	22	0.0 ± 1.0	0.000 ± 0.013
300	Search	50	1634	22	$40. \pm 28$	0.54 ± 0.40
100	Cosmic	100	112	1	61 ± 35	0.54 ± 0.63
100	Search	100	112	1	445 ± 94	4.0 ± 4.1
300	Cosmic	100	112	1	0.0 ± 1.0	0.0000 ± 0.0089
300	Search	100	112	1	$40. \pm 28$	0.36 ± 0.44

[a] The uncertainty on these numbers is driven by a large prescale factor applied during data skimming as discussed in Section **??**.

8.3 Noise Events in the Search Region

Every effort has been made to remove noise events, as discussed in previous sections. Figures 9.7 and 9.4 show no discernible noise signature which in 2010 manifested as a rate spike localized in time and jet position. However, it is difficult, if not impossible, to be certain that all noise sources have been eliminated. If no significant excess of events over other backgrounds is observed, it is conservatively assumed that no additional background noise events are present when setting limits on the signal production rate. If instead a significant excess is observed, we would work hard to determine whether the excess were noise-like or signal-like, based on the properties of the excess events.

8.4 Total Background Yield

Estimating the total expected background in the search region is now simply a matter of adding the expected cosmic and beam-halo muon contributions. However, since the expected background rate is so low, the uncertainty in that rate dominates and care is needed in error propagation. Five independent counting experiments are used to calculate the total background. They are: cosmic-region empty-bunches no muon segment, C_N^E; cosmic-region empty-bunches forward muon segment, C_F^E; search-regions unpaired-bunches no muon segment loose jet, A_N^U; search-regions unpaired-bunches forward muon segment loose jet, A_F^U; search-region empty-bunches forward muon segment, S_F^E. In this nomenclature, the final signal region is S_N^E the search region (late 2011 and 2012 data) with no muon segments in the empty bunches. Finally, α denotes the livetime scaling between the cosmic and search regions.

$$T = \alpha \left(C_N^E - C_F^E \frac{A_N^U}{A_F^U} \right) + S_F^E \frac{A_N^U}{A_F^U}. \tag{8.1}$$

This allows the calculation of the total background, T, and its uncertainty, δT by applying $(\delta T)^2 = \sum_i (\frac{\partial T}{\partial x_i} \delta x_i)^2$.

Chapter 9

Final Event Yields

We plot the distributions of the final signal region after applying all selection criteria and compare to the estimated backgrounds. As we can see in Figures 9.5 the shapes and yield of events agree well. As shown in Table 12.2, we see no evidence for excess signal candidates. Some candidate event displays are shown in Figure 9.1.

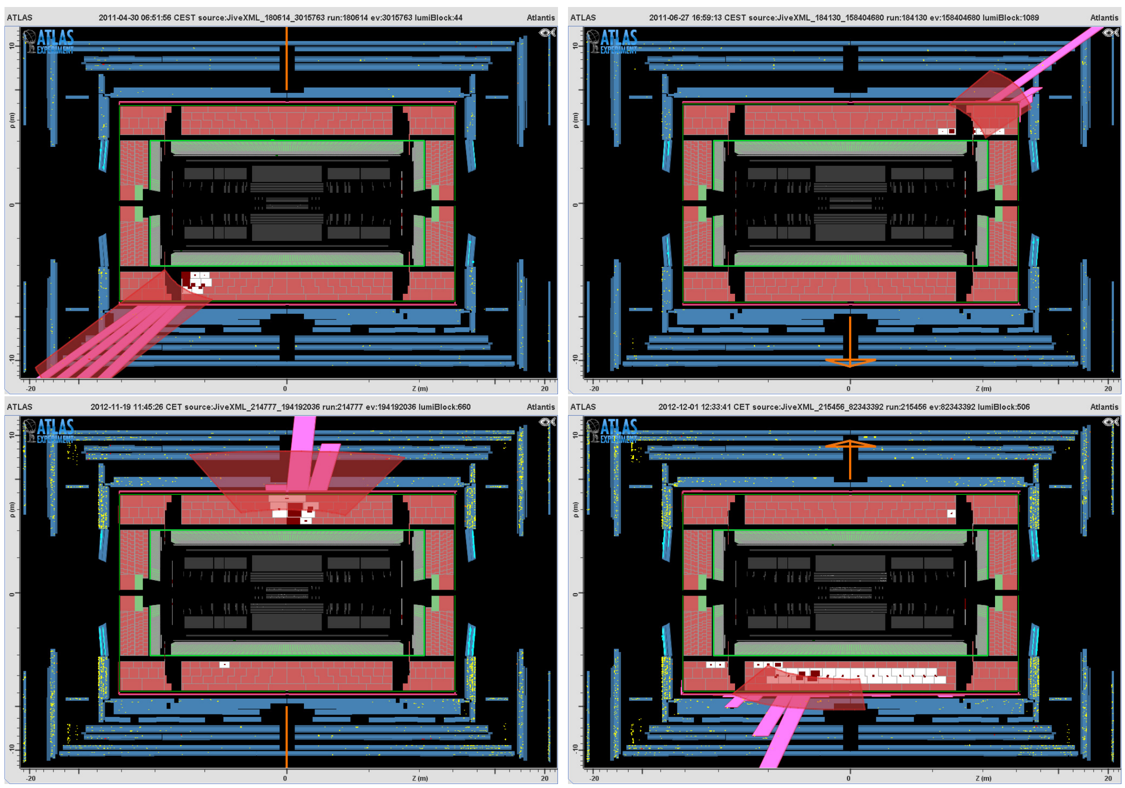

Figure 9.1: Some candidate event displays from 2011 (top) and 2012 (bottom) data passing all selections. The pink bars indicate the magnitude of the CaloTower p_T, while the shaded red area indicates the location and p_T of the primary jet.

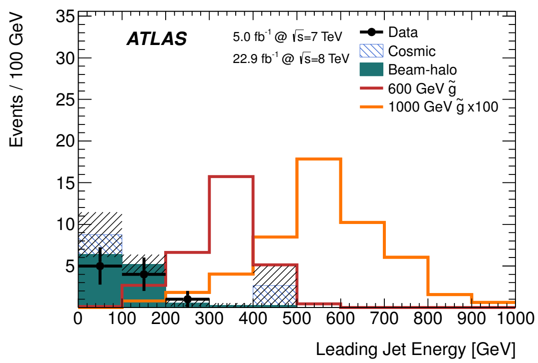

(a)

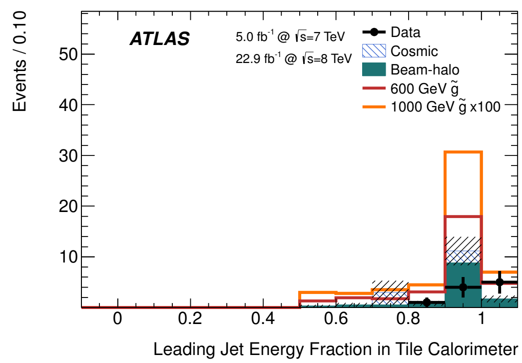

(b)

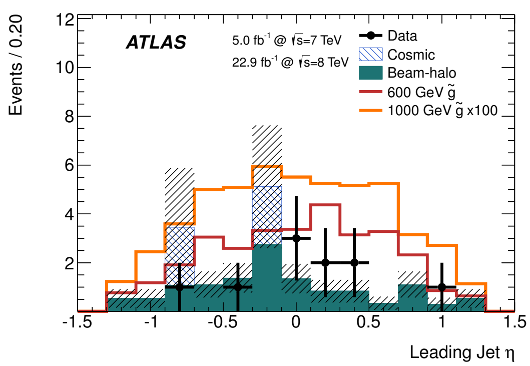

(c)

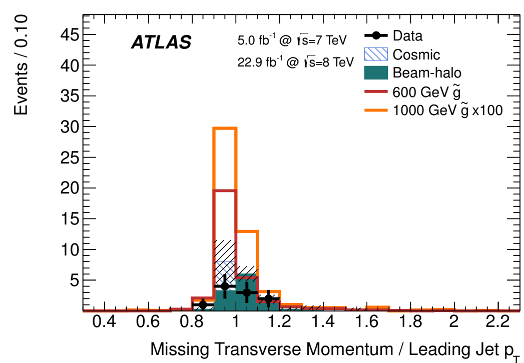

(d)

Figure 9.2: The yield of events in the signal region for candidates with all cuts (in Table 7.1) up to the muon veto but excluding jet energy $>$ 100 GeV. All samples are scaled to represent their anticipated yield in the search region. The beam-halo and cosmic predictions are stacked on top of each other.

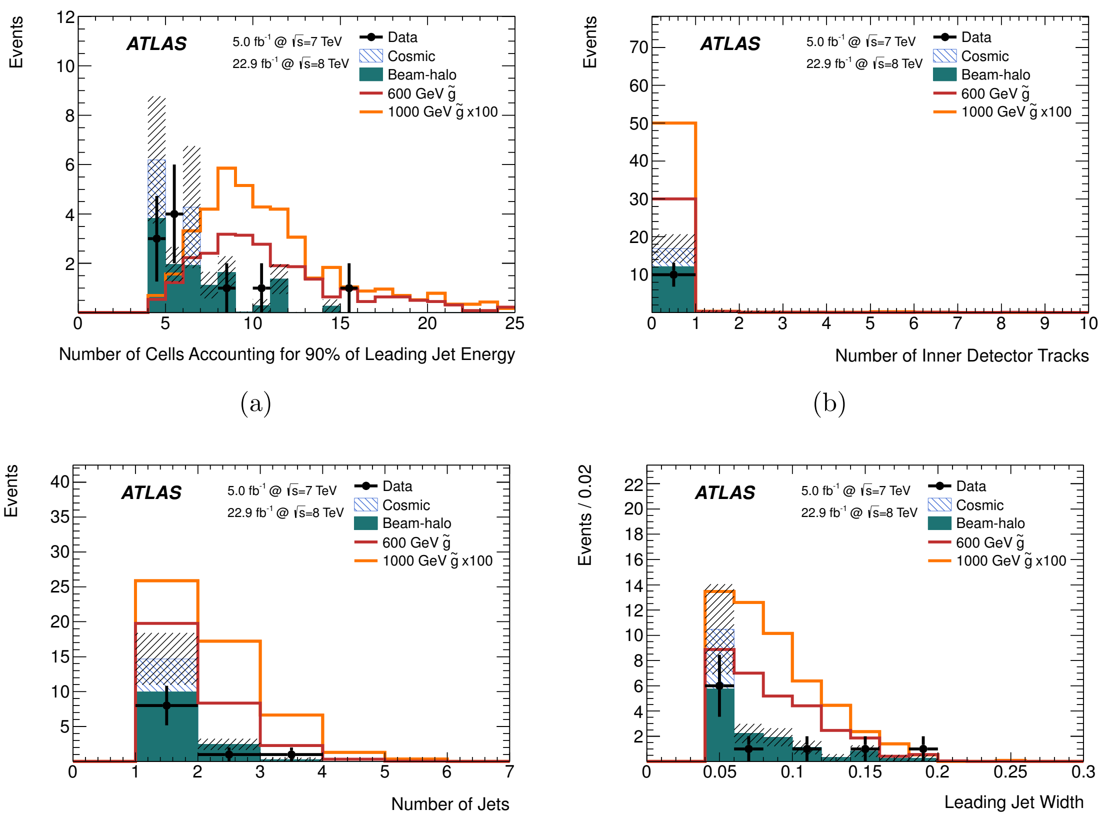

(a) (b) (c) (d)

Figure 9.3: The yield of events in the signal region for candidates with all cuts (in Table 7.1) up to the muon veto but excluding jet energy > 100 GeV. All samples are scaled to represent their anticipated yield in the search region. The beam-halo and cosmic predictions are stacked on top of each other.

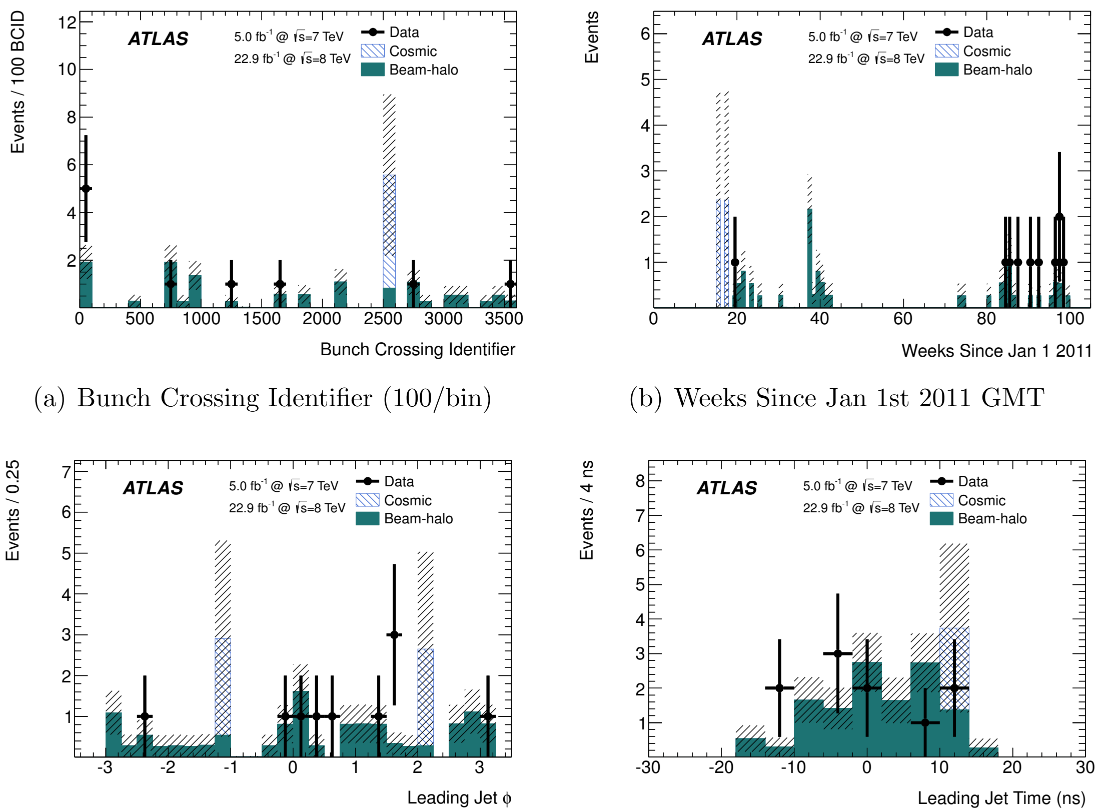

(a) Bunch Crossing Identifier (100/bin)

(b) Weeks Since Jan 1st 2011 GMT

(c) Jet ϕ

(d) Jet Time (ns)

Figure 9.4: The yield of events in the signal region for candidates with all cuts (in Table 7.1) up to the muon veto but excluding jet energy > 100 GeV. All samples are scaled to represent their anticipated yield in the search region. The beam-halo and cosmic predictions are stacked on top of each other.

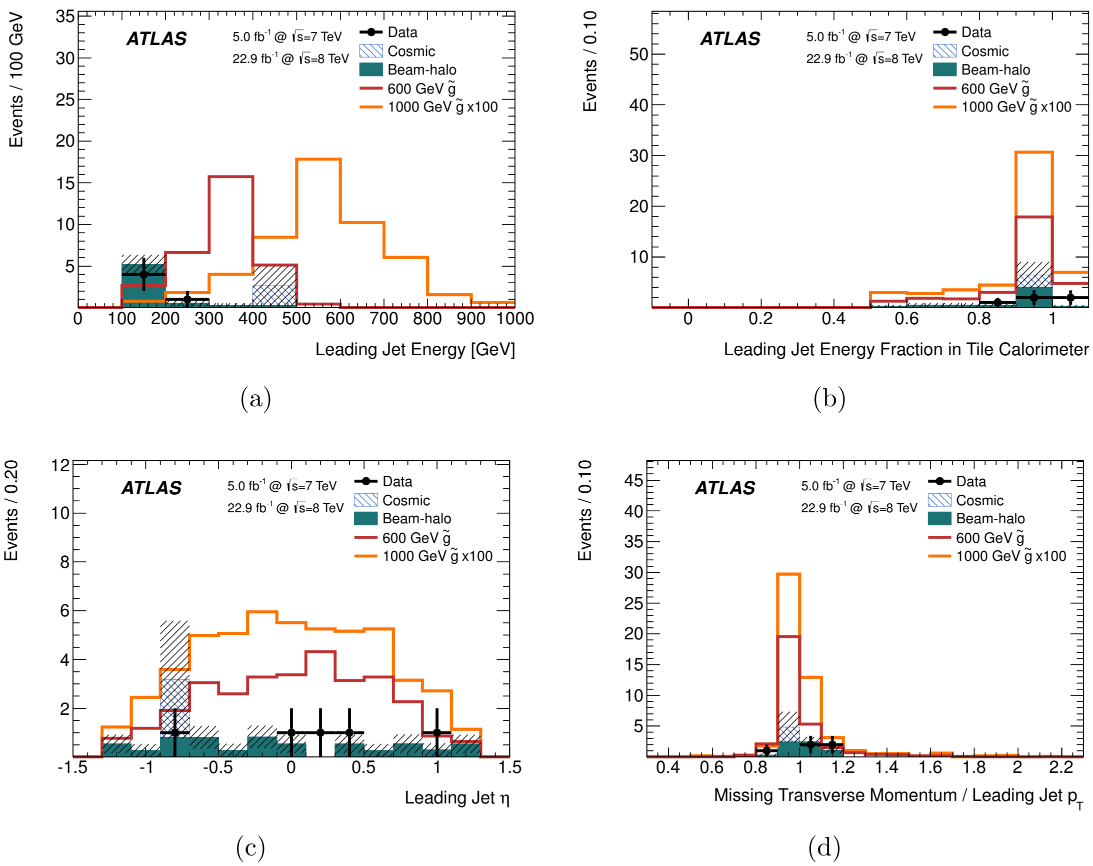

(a) (b) (c) (d)

Figure 9.5: The yield of events in the signal region for candidates with all cuts (in Table 7.1) except jet energy > 300 GeV. All samples are scaled to represent their anticipated yield in the search region. The beam-halo and cosmic predictions are stacked on top of each other.

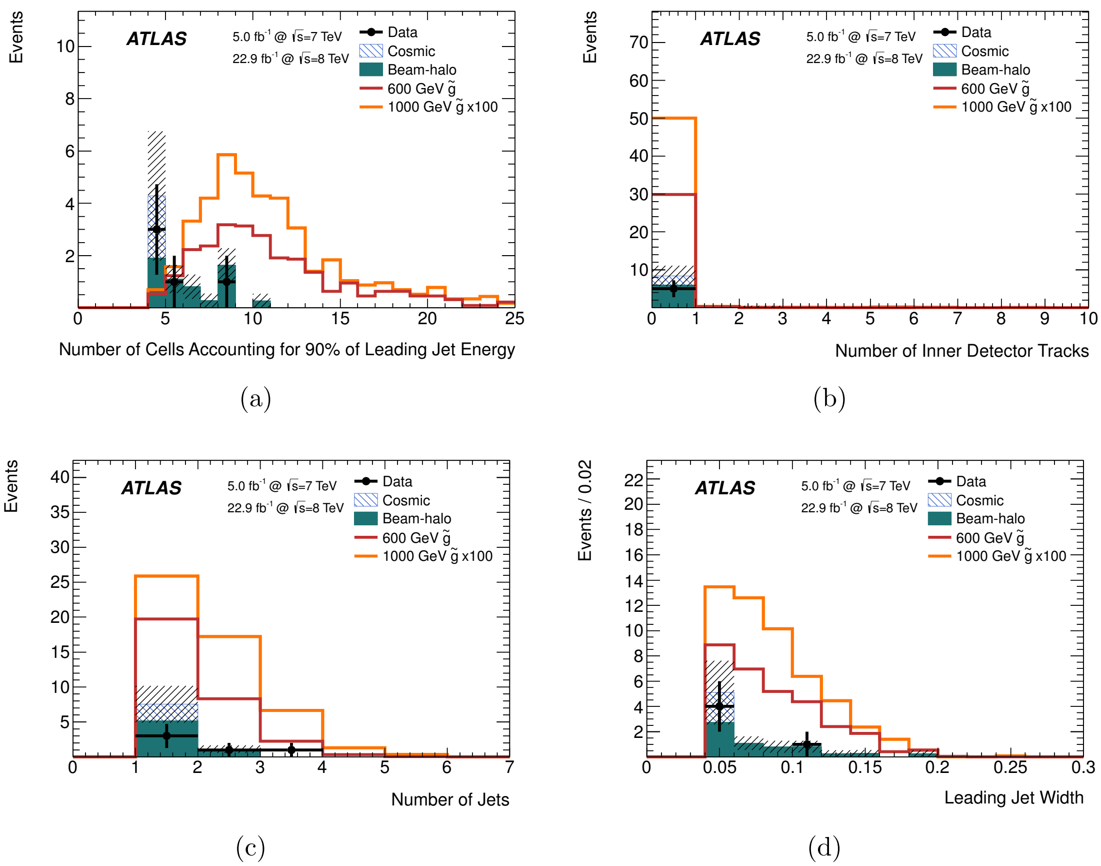

(a) (b) (c) (d)

Figure 9.6: The yield of events in the signal region for candidates with all cuts (in Table 7.1) except jet energy > 300 GeV. All samples are scaled to represent their anticipated yield in the search region. The beam-halo and cosmic predictions are stacked on top of each other.

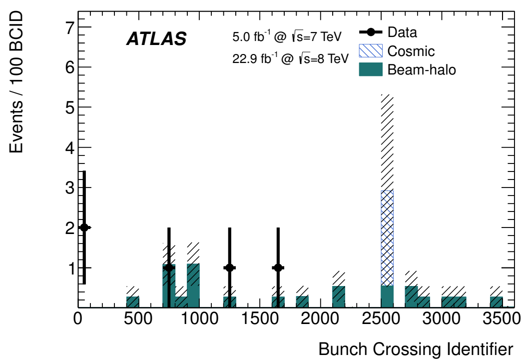

(a) Bunch Crossing Identifier (100/bin)

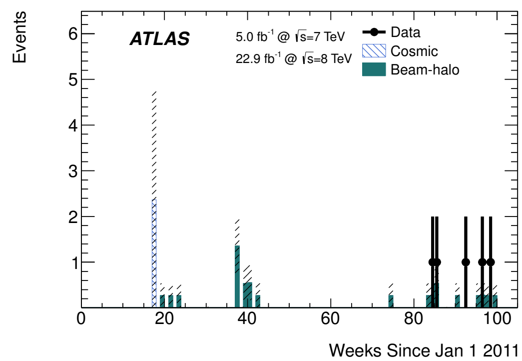

(b) Weeks Since Jan 1st 2011 GMT

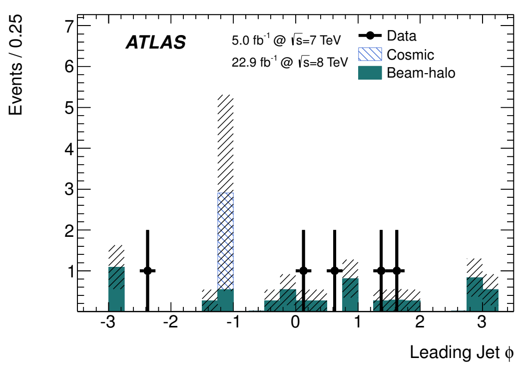

(c) Jet ϕ

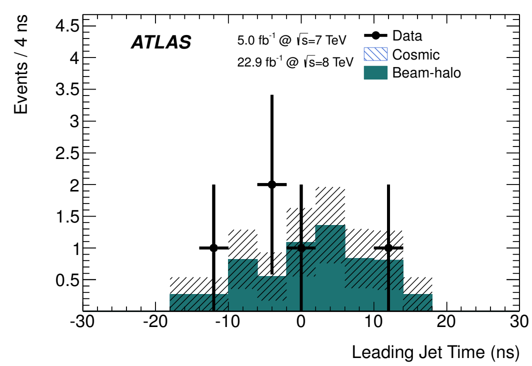

(d) Jet Time (ns)

Figure 9.7: The yield of events in the signal region for candidates with all cuts (in Table 7.1) except jet energy > 300 GeV. All samples are scaled to represent their anticipated yield in the search region. The beam-halo and cosmic predictions are stacked on top of each other.

Chapter 10

Contributions to Signal Efficiency

Quantifying the signal efficiency for the stopped gluino search presents several unique challenges due to the non-prompt nature of their decays. Specifically we have four sources of inefficiency: stopping fraction (Section 6), reconstruction efficiency (Table 7.5,7.6), accidental muon veto, and probability to have the decay occur in an empty bunch crossing (timing efficiency). Since the first two have been discussed elsewhere, here we focus only on accidental muon veto and timing efficiency.

10.1 Accidental Muon Veto

Operating in the empty bunch crossings has the tremendous advantage of eliminating collision backgrounds. However because we employ such a stringent muon activity veto, a significant number of events are rejected in the offline analysis from spurious segments in the muon system, which are not properly modeled in the MC signal simulation. Both activated nuclei β-decay and δ-rays could produce segments with at least 4 hits. This is a separate effect from a signal decay producing a muon segment which then vetoes the event. To study the rate of muon segments we examine events from the empty random trigger data in 2011 and 2012 as function of run number, since the effect can depend strongly on instantaneous luminosity. In Figure 10.1 we calculate the rate of these events which have a muon segment from noise or other background[1]. The efficiency per run is applied on a live-time weighted basis to the cosmic background estimate. It is also applied to the cosmic background estimate after the muon veto, since the probability to have the cosmic background event pass cuts and contribute to the signal region events will depend on it passing the muon veto. The beam-halo background estimate already implicitly accounts for this effect across run periods. For signal, this effect is accounted for, on a per-run basis, inside the timing efficiency calculation.

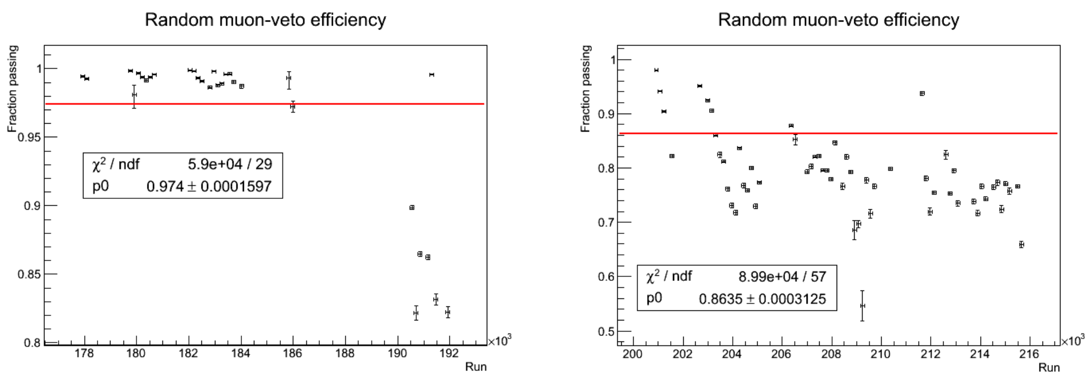

(a) 2011 (b) 2012

Figure 10.1: The fraction of random-triggered empty events (L1_RD1_EMPTY) that do not have a muon segment in it passing cuts (from pile-up / background / noise) in 2011 and 2012, by run number grouping. The signal efficiency is scaled by this efficiency, using the value from the nearest run number grouping. (The fit is purely to guide the eye and not used in the analysis.) Unfortunately, data is not available for runs approximately 186-190k, so the nearest veto fraction (either 97% or 89%) is used.

10.2 Timing Efficiency

The expected signal decay rate does not scale with instantaneous luminosity. Rather, at any moment in time, the decay rate is a function of the hypothetical lifetime and

[1] Unfortunately, data from the random-triggered empty crossings is not easily available for runs ≈186k–190k since it is no longer staged to disk. But the effect on total efficiency is small, since there is just ≈3 fb^{-1}during this period, and the efficiency is bounded between 98% and 85%. This potential effect is accounted for in the timing efficiency's 5% systematic uncertainty.

the entire luminosity history. For example, the decay rate anticipated in today's run is boosted by luminosity delivered yesterday for longer lifetimes. To address the complicated time behavior of the gluino decays, we define a timing efficiency for each lifetime hypothesis, $\epsilon_T(\tau)$, as the number of gluinos decaying in an empty bunch crossing divided by the total number that stopped. This means the number of gluinos we expect to fully reconstruct is $L \times \sigma \times \epsilon_{\text{stop}} \times \epsilon_T(\tau) \times \epsilon_{\text{recon}}$. To calculate the timing efficiency for the actual 2011 and 2012 LHC and ATLAS run schedule, we developed a numerical algorithm and had to fetch several pieces of information from ATLAS's online conditions database, CERN online conditions logging database (COOL). We split the efficiency calculation into short and long lifetimes, to simplify the simulation. For lifetimes less than 10 seconds we take into account bunch structure, but not luminosity block and run structure. For lifetimes over 1 seconds, we average over bunches but allow stopped gluinos from one luminosity block and run to decay in a separate one.

We assign a relative uncertainty of 5% to the timing uncertainty. This accounts for trigger deadtime, prescales (L1_J30_EMPTY was on the auto-prescale list) and the accidental muon veto miscalculation. Any run-by-run miscalibration of the luminosity is ignored at this step and instead accounted for in the luminosity uncertainty discussed in Section 11.

<u>For the short lifetimes:</u>

For each continuous set of luminosity blocks in the good runs list we take the bunch structure and luminosity per bunch from COOL. The algorithm then analytically determines the number of stopped gluinos and number of decays in each bunch-crossing identifier (BCID) for each lifetime hypothesis given the delivered luminosity in each bunch. We simply add up the number of decays occurring in the empty bunch crossing and divide by all the decays. Thus the timing efficiency is a luminosity weighted average over each of the run's global timing efficiency.

<u>For long lifetimes:</u>

Now instead of looking at each run separately, we examine all luminosity blocks together. For each luminosity block we use the ATLAS's calculation of the delivered luminosity (thus we ignore any GRL input), and its time boundaries. Having the full luminosity history allows us to calculate how many decays are expected in any time window for a lifetime hypothesis. Next we use a good runs list to specify which luminosity blocks ATLAS was taking data (with analysis data quality cuts applied). Finally, for each luminosity block, we multiply the number of decays by the fraction of bunches that were empty to get the number of decays "seen". The timing efficiency, shown in Figure 10.2, reaches half its maximum at $\tau \approx 10^6\,\mu$s. For lifetimes much shorter than this, there are relatively few colliding bunches which can contribute, since there is an enforced gap of 250 ns between the last colliding bunch and leading empty bunch.

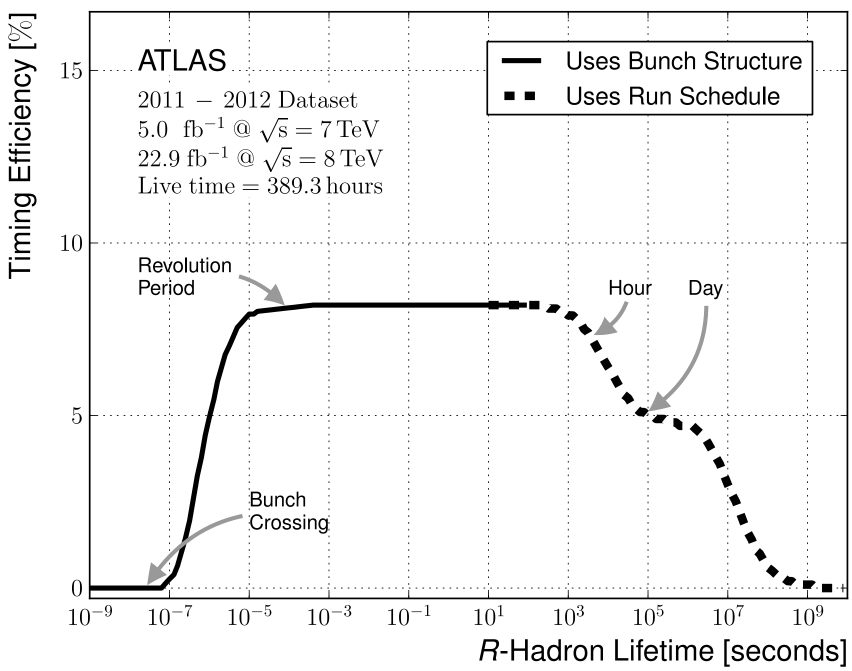

Figure 10.2: A plot of the timing efficiency, $\epsilon_T(\tau)$, as a function of R-hadron lifetime in seconds.

Chapter 11

Systematic uncertainties

11.1 Systematic Uncertainties on Signal Yield

We study three sources of systematic uncertainty on the signal efficiency: the R-hadron interaction with matter, the out-of-time decays in the calorimeters, and the effect of the selection criteria. In addition to these, which are discussed below, we also assign a 3.4% uncertainty on the luminosity measurement. We do not account for the gluino-production cross section uncertainty, which is, included in the limit determinations.

Table 11.1: Summary of systematic uncertainties on the signal yield.

Factor	Relative Magnitude	Reference
Luminosity	3.4%	Section 11
R-hadron-Matter Interactions	11 %	Section 11.1.1
Calorimeter Timing	3 %	Section 11.1.2
Selection Criteria	7.5-58.2%	Section 11.1.3
Timing Efficiency	5 %	Section 10.2
Stopping MC Stats	5.8-9.4%	Table 6.1
Selection MC Stats	3.1-21.1%	Table 7.5,7.6

Table 11.2: Fractional systematic uncertainty on signal yield listed by signal point. This includes effects arising from lack of Monte Carlo statistics and uncertainty in the signal modeling. The uncertainty in the background estimation is show in Table 12.2.

Sample Name	Jet Threshold (GeV) 100	300
gen_g_400_gqq_100	15.9%	–
gen_g_600_gqq_100	15.7%	35.3%
gen_g_800_gqq_100	15.8%	16.2%
gen_g_1000_gqq_100	15.1%	15.3%
gen_g_400_gqq_300	60.1%	–
gen_g_600_gqq_500	48.7%	–
gen_g_800_gqq_700	35.6%	–
gen_g_1000_gqq_900	33.7%	–
gen_g_600_tt_100	18.5%	19.8%
gen_g_800_tt_100	17.7%	18.4%
gen_g_1000_tt_100	16.3%	16.5%
gen_g_400_tt_20	18.8%	36.8%
gen_g_600_tt_220	17.0%	30.5%
gen_g_800_tt_420	17.4%	28.7%
gen_g_1000_tt_620	17.4%	33.5%
int_g_400_gqq_100	16.7%	–
int_g_600_gqq_100	15.5%	28.0%
int_g_800_gqq_100	15.5%	16.0%
int_g_1000_gqq_100	16.1%	16.5%
reg_g_400_gqq_100	15.9%	–
reg_g_600_gqq_100	15.4%	30.6%
reg_g_800_gqq_100	17.8%	15.7%
reg_g_1000_gqq_100	18.8%	17.7%
gen_g_600_gqq_560	–	–
gen_g_600_gqq_540	259.8 %	–
gen_g_600_gqq_520	254.7 %	–
gen_g_600_gqq_480	12.9 %	–
gen_g_600_gqq_450	8.3 %	–
gen_g_600_gqq_400	7.3 %	509.9 %
gen_g_600_gqq_300	6.7 %	203.1 %
gen_g_600_gqq_200	7.0 %	41.0 %

Table 11.3: Fractional systematic uncertainty on signal yield listed by signal point. This includes effects arising from lack of Monte Carlo statistics and uncertainty in the signal modeling. The uncertainty in the background estimation is show in Table 12.2.

Sample Name	Jet Threshold (GeV) 100	300
reg_sb_300_100	17.8%	–
reg_sb_400_100	17.3%	–
reg_sb_600_100	16.6%	59.6%
reg_sb_800_100	15.8%	17.0%
reg_sb_400_300	59.1%	–
reg_sb_600_500	50.0%	–
reg_sb_800_700	35.2%	–
reg_sb_300_200	74.0%	–
reg_st_300_100	16.0%	–
reg_st_400_100	16.2%	–
reg_st_600_100	17.2%	39.8%
reg_st_800_100	16.5%	19.5%
gen_st_300_100	15.6%	–
gen_st_400_100	16.2%	–
gen_st_600_100	16.7%	44.4%
gen_st_800_100	16.5%	17.0%
gen_st_400_150	16.8%	–
gen_st_400_200	15.5%	–
gen_st_600_400	15.9%	–
gen_st_800_600	16.1%	–

11.1.1 R-hadron-Matter Interactions

We use the different generated signal samples to estimate a systematic on the stopping efficiency due to the scattering model. There are two sources of theoretical uncertainty: spectrum of R-hadrons, and their nuclear interactions. To estimate the effect from different R-hadron allowed states three different scattering models are employed: generic, Regge and intermediate. Each allows a different set of charged states that affect the electromagnetic interaction in the calorimeters. There is also a significant uncertainty in the nuclear interactions of the gluino or R-hadron with the calorimeter . To determine this effect we calculated the stopping fraction after varying the nuclear cross section by a factor of two. The two-sided difference gave a relative uncertainty of 11%, which we use as the systematic uncertainty in limit setting.

11.1.2 Timing in the Calorimeters

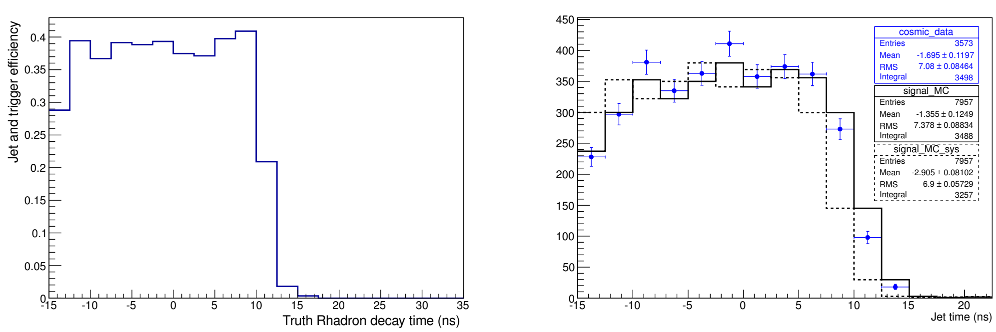

Figure 11.1: Left: The fractional efficiency of signal events as a function of their truth decay time offset. We only use events which had an offset between -15 and 10 nanoseconds. However we estimate the systematic uncertainty by varying this range by 5 nanoseconds in each direction. Right: The reconstructed jet time for events from the MC simulated (using the timing cut) (black, solid), compared to cosmic data events (blue, points). The dashed black line is the result of the systematic shift of the timing cut by -5 ns.

Since the R-hadron decays completely asynchronously with bunch crossings it is possible that the calorimeters might incorrectly measure the energy deposits. To quantify this we applied a random time offset, from -15 to 35 ns, to each R-hadron decay compared to the nominal bunch crossing as discussed in Section 6. Next we study the total number of events passing the offline cuts as a function of this timing offset as shown in Fig 11.1. The digitization and reconstruction steps of the simulation always force the data to reside in one bunch crossing, so very early or late decays are never seen. However, this does not reflect true detector operation, in which a very late decay (i.e. $+40\,\mathrm{ns}$) would be tagged in the next bunch crossing. For this analysis we pick a $25\,\mathrm{ns}$ wide window that captures most of the events, specifically -15 to 10 nanoseconds.

Since this window might not perfectly represent the calorimeter operation, we vary the bounds by 5 ns in each direction (keeping the range 25 ns) and measure the fraction for each sample window. We know from beam splash events that the calorimeter cell timing resolution is better than 5 ns. We then calculate the minimum and maximum efficiency for each mass point, and take the difference as the uncertainty. Across all signals points, the difference was always less than 3% so we assign this as the systematic uncertainty on the calorimeter timing response.

11.1.3 Selection Criteria

To quantify the systematic uncertainty on the event selection criteria we evaluated the signal efficiency across a series of different cuts. We generated this list by taking the nominal set of cuts and varying each individual cut up or down by 10% such that each set had one different criteria (i.e. leading jet energy). For cuts with an integer value, such as number of muon segments, we stepped up or down by one unit. We conclude that the largest fractional uncertainty on the signal efficiency is 10%, as shown in Tables 11.4,11.5, and will use this value for limit setting for all models. To produce Tables 11.6,11.7, the signal's jet energy spectrum was varied by 10% and quantifying the change in reconstruction efficiency. Varying the jet energy scale dominates the total uncertainty from the selection criteria.

Table 11.4: The lowest and highest signal efficiencies found after altering each of the cuts up and down individually. To calculate the systematic uncertainty we take the largest deviation from the standard cuts. The total uncertainty includes this deviation as well as the much smaller statistical error from the finite number of simulation events.

	Signal Efficiencies			Uncertainty	
Sample Name	Lowest	Standard	Highest	Total	Relative
gen_g_400_gqq_100	12.2 %	13.3 %	14.4 %	1.2 %	9.0 %
gen_g_600_gqq_100	12.9 %	13.6 %	14.7 %	1.2 %	8.6 %
gen_g_800_gqq_100	12.5 %	13.6 %	14.6 %	1.2 %	8.9 %
gen_g_1000_gqq_100	11.8 %	12.6 %	13.4 %	0.9 %	7.5 %
gen_g_400_gqq_300	2.1 %	5.0 %	6.8 %	2.9 %	58.2 %
gen_g_600_gqq_500	3.0 %	5.5 %	7.1 %	2.6 %	46.5 %
gen_g_800_gqq_700	3.9 %	5.7 %	7.1 %	1.9 %	32.6 %
gen_g_1000_gqq_900	4.4 %	6.3 %	7.6 %	1.9 %	30.6 %
gen_g_600_tt_100	7.8 %	8.9 %	9.6 %	1.1 %	12.8 %
gen_g_800_tt_100	8.3 %	8.9 %	9.8 %	1.0 %	11.6 %
gen_g_1000_tt_100	7.5 %	8.1 %	8.7 %	0.7 %	9.1 %
gen_g_400_tt_20	7.4 %	8.0 %	8.9 %	1.0 %	13.1 %
gen_g_600_tt_220	7.9 %	8.7 %	9.4 %	0.9 %	10.5 %
gen_g_800_tt_420	6.6 %	7.2 %	7.9 %	0.8 %	10.9 %
gen_g_1000_tt_620	6.7 %	7.4 %	8.1 %	0.8 %	11.0 %
int_g_400_gqq_100	7.9 %	8.7 %	9.2 %	0.9 %	9.9 %
int_g_600_gqq_100	8.4 %	8.9 %	9.4 %	0.7 %	7.7 %
int_g_800_gqq_100	7.9 %	8.4 %	8.9 %	0.6 %	7.7 %
int_g_1000_gqq_100	7.0 %	7.4 %	7.9 %	0.6 %	8.6 %
reg_g_400_gqq_100	10.6 %	11.6 %	12.4 %	1.0 %	8.9 %
reg_g_600_gqq_100	11.0 %	11.8 %	12.7 %	1.0 %	8.2 %
reg_g_800_gqq_100	9.6 %	10.3 %	11.5 %	1.2 %	12.1 %
reg_g_1000_gqq_100	8.8 %	9.6 %	10.8 %	1.3 %	13.5 %
gen_g_600_gqq_200	13.3 %	14.2 %	15.2 %	1.0 %	7.0 %
gen_g_600_gqq_300	12.8 %	13.6 %	14.5 %	0.9 %	6.7 %
gen_g_600_gqq_400	11.1 %	11.9 %	12.7 %	0.9 %	7.3 %
gen_g_600_gqq_450	9.3 %	10.1 %	10.9 %	0.8 %	8.3 %
gen_g_600_gqq_480	7.3 %	8.3 %	9.1 %	1.1 %	12.9 %
gen_g_600_gqq_520	0.2 %	1.0 %	3.7 %	2.6 %	254.7 %
gen_g_600_gqq_540	0.0 %	0.0 %	0.0 %	0.0 %	259.8 %

Table 11.5: The lowest and highest signal efficiencies found after altering each of the cuts up and down individually. To calculate the systematic uncertainty we take the largest deviation from the standard cuts. The total uncertainty includes this deviation as well as the much smaller statistical error from the finite number of simulation events.

	Signal Efficiencies			Uncertainty	
Sample Name	Lowest	Standard	Highest	Total	Relative
reg_sb_300_100	6.4 %	7.0 %	7.7 %	0.8 %	11.3 %
reg_sb_400_100	8.4 %	9.3 %	9.9 %	1.0 %	10.9 %
reg_sb_600_100	8.7 %	9.2 %	10.0 %	0.9 %	9.7 %
reg_sb_800_100	8.2 %	8.8 %	9.4 %	0.7 %	8.3 %
reg_sb_400_300	1.4 %	3.1 %	4.4 %	1.8 %	57.0 %
reg_sb_600_500	2.3 %	4.3 %	5.3 %	2.1 %	47.7 %
reg_sb_800_700	2.3 %	3.4 %	4.3 %	1.1 %	31.5 %
reg_sb_300_200	0.8 %	2.8 %	4.9 %	2.0 %	72.1 %
reg_st_300_100	8.8 %	9.5 %	10.1 %	0.8 %	8.9 %
reg_st_400_100	8.3 %	9.0 %	9.6 %	0.8 %	9.2 %
reg_st_600_100	7.7 %	8.6 %	9.2 %	0.9 %	10.8 %
reg_st_800_100	7.9 %	8.6 %	9.2 %	0.8 %	9.5 %
gen_st_300_100	9.7 %	10.4 %	11.0 %	0.9 %	8.3 %
gen_st_400_100	8.6 %	9.2 %	10.0 %	0.8 %	9.2 %
gen_st_600_100	7.9 %	8.6 %	9.3 %	0.8 %	9.9 %
gen_st_800_100	7.9 %	8.6 %	9.2 %	0.8 %	9.5 %
gen_st_400_150	9.0 %	9.7 %	10.6 %	1.0 %	10.3 %
gen_st_400_200	9.3 %	9.9 %	10.6 %	0.8 %	8.0 %
gen_st_600_400	8.9 %	9.6 %	10.1 %	0.8 %	8.7 %
gen_st_800_600	8.4 %	9.0 %	9.7 %	0.8 %	8.9 %

Table 11.6: The lowest and highest signal efficiencies found after altering only the jet energy cut up and down by 10 GeV. To calculate the systematic uncertainty we take the largest deviation from the standard cuts. The total uncertainty includes this deviation as well as the much smaller statistical error from the finite number of simulation events.

	Signal Efficiencies			Uncertainty	
Sample Name	Lowest	Standard	Highest	Total	Relative
gen_g_400_gqq_100	13.0 %	13.3 %	13.5 %	0.6 %	4.3 %
gen_g_600_gqq_100	13.5 %	13.6 %	13.6 %	0.5 %	3.9 %
gen_g_800_gqq_100	13.6 %	13.6 %	13.6 %	0.5 %	3.9 %
gen_g_1000_gqq_100	12.5 %	12.6 %	12.6 %	0.5 %	4.2 %
gen_g_400_gqq_300	2.1 %	5.0 %	6.8 %	2.9 %	58.2 %
gen_g_600_gqq_500	3.0 %	5.5 %	7.1 %	2.6 %	46.5 %
gen_g_800_gqq_700	3.9 %	5.7 %	7.1 %	1.9 %	32.6 %
gen_g_1000_gqq_900	4.4 %	6.3 %	7.6 %	1.9 %	30.6 %
gen_g_600_tt_100	8.7 %	8.9 %	8.9 %	0.5 %	5.1 %
gen_g_800_tt_100	8.5 %	8.9 %	8.9 %	0.5 %	6.1 %
gen_g_1000_tt_100	7.8 %	8.1 %	8.1 %	0.5 %	6.1 %
gen_g_400_tt_20	8.0 %	8.0 %	8.0 %	0.4 %	5.0 %
gen_g_600_tt_220	8.7 %	8.7 %	8.8 %	0.4 %	4.8 %
gen_g_800_tt_420	7.2 %	7.2 %	7.3 %	0.4 %	5.3 %
gen_g_1000_tt_620	7.3 %	7.4 %	7.4 %	0.4 %	5.3 %
int_g_400_gqq_100	8.6 %	8.7 %	8.7 %	0.4 %	5.0 %
int_g_600_gqq_100	8.8 %	8.9 %	8.9 %	0.4 %	4.9 %
int_g_800_gqq_100	8.4 %	8.4 %	8.5 %	0.4 %	4.9 %
int_g_1000_gqq_100	7.3 %	7.4 %	7.4 %	0.4 %	5.4 %
reg_g_400_gqq_100	11.4 %	11.6 %	11.8 %	0.5 %	4.4 %
reg_g_600_gqq_100	11.7 %	11.8 %	11.8 %	0.4 %	3.5 %
reg_g_800_gqq_100	10.2 %	10.3 %	10.3 %	0.4 %	3.7 %
reg_g_1000_gqq_100	9.4 %	9.6 %	9.6 %	0.4 %	4.0 %
gen_g_600_gqq_200	76.1 %	77.1 %	77.8 %	1.1 %	1.4 %
gen_g_600_gqq_300	73.6 %	75.0 %	76.3 %	1.5 %	2.1 %
gen_g_600_gqq_400	67.0 %	69.6 %	72.0 %	2.7 %	3.9 %
gen_g_600_gqq_450	59.6 %	63.9 %	67.4 %	4.3 %	6.7 %
gen_g_600_gqq_480	46.4 %	54.5 %	61.2 %	8.1 %	14.9 %
gen_g_600_gqq_520	3.8 %	12.0 %	28.9 %	16.9 %	140.6 %
gen_g_600_gqq_540	0.3 %	0.7 %	3.5 %	2.8 %	400.6 %

Table 11.7: The lowest and highest signal efficiencies found after altering only the jet energy cut up and down by 10 GeV. To calculate the systematic uncertainty we take the largest deviation from the standard cuts. The total uncertainty includes this deviation as well as the much smaller statistical error from the finite number of simulation events.

	Signal Efficiencies			Uncertainty	
Sample Name	Lowest	Standard	Highest	Total	Relative
reg_sb_300_100	55.7 %	62.1 %	68.2 %	6.4 %	10.3 %
reg_sb_400_100	73.0 %	75.8 %	78.3 %	3.1 %	4.1 %
reg_sb_600_100	81.8 %	82.8 %	83.5 %	1.6 %	1.9 %
reg_sb_800_100	84.9 %	85.4 %	85.8 %	1.4 %	1.6 %
reg_sb_400_300	13.0 %	25.7 %	38.6 %	12.9 %	50.3 %
reg_sb_600_500	16.7 %	28.6 %	41.2 %	12.6 %	43.9 %
reg_sb_800_700	18.7 %	29.9 %	42.6 %	12.8 %	42.9 %
reg_sb_300_200	9.1 %	20.7 %	33.8 %	13.1 %	63.2 %
reg_st_300_100	48.7 %	52.9 %	57.5 %	4.7 %	8.9 %
reg_st_400_100	56.8 %	60.6 %	64.3 %	3.9 %	6.5 %
reg_st_600_100	68.9 %	70.9 %	73.1 %	2.5 %	3.5 %
reg_st_800_100	74.4 %	75.5 %	76.6 %	1.7 %	2.2 %
gen_st_300_100	50.2 %	54.4 %	58.5 %	4.3 %	8.0 %
gen_st_400_100	59.2 %	63.0 %	66.5 %	3.9 %	6.2 %
gen_st_600_100	69.1 %	70.8 %	73.0 %	2.5 %	3.6 %
gen_st_800_100	74.3 %	75.7 %	76.8 %	1.8 %	2.4 %
gen_st_400_150	55.1 %	58.6 %	62.9 %	4.5 %	7.6 %
gen_st_400_200	49.3 %	52.9 %	57.4 %	4.6 %	8.7 %
gen_st_600_400	49.9 %	54.3 %	59.5 %	5.2 %	9.6 %
gen_st_800_600	49.4 %	53.7 %	58.2 %	4.6 %	8.7 %

11.2 Systematic Uncertainties on Background Yield

The statistical uncertainty on the background yield arises from the amount of live time (in bunch hours) for the cosmic data sample and the limited events in the unpaired data. The systematic uncertainty arises from the scaling factor used to propagate the cosmic sample data yield into an expectation of background events in the search region. Similarly, for the beam-halo background, a systematic is assigned using the statistical uncertainty of the estimate in Table 12.2. Determining the scale factor between data-taking regions and the timing efficiency employ similar methods. The timing efficiency is checked by ensuring that the calculation for long- and short-lifetimes match. A conservative 5% uncertainty is assigned to combination of timing efficiency and scale factor.

Chapter 12

Results

The predicted number of background events agrees well with the observed number of events in the search region. Using these yields we calculate upper limits on the cross section of gluino pair production in a simple "cut-and-count" method and also as a function of gluino mass for a given range of lifetimes. In Table 12.1, we show the different efficiencies and multiplicative factors used to convert the limit on number of events into number of produced events (and thus gluino mass).

12.1 Limit Setting Procedure

We use a Bayesian method to set 95% confidence level upper limits on the number of events of signal that could be produced. For each signal sample we fit the signal

Table 12.1: Summary of factors used for converting the limit on number of observed signal events to number of produced signal events.

Factor	Magnitude	Notes	Reference
Luminosity @ 7 TeV	$5.0\,\text{fb}^{-1}$	Periods 2011F-M, after GRL	Table 5.2
Luminosity @ 8 TeV	22.9fb^{-1}	Periods 2012A-L, after GRL	Table 5.2
$\epsilon_{reconstruction}$	10 %	Approximate value for selection	Table 7.5
$\epsilon_{stopping}$	12 %	Generic models	Table 6.1
ϵ_{timing}	8.4 %	$10^{-5} < \tau\,(\text{sec}) < 10^{3}$	Fig. 10.2

Table 12.2: The number of observed and expected events corresponding to each of the selection criteria. Note that the total expected background includes the contribution from cosmic background (scaled to livetime times muon-veto efficiency) plus the contribution from beam-halo. The uncertainty is for the beam-halo estimate in the "cosmic" region and in the search region is partially correlated. To demonstrate the effect on the total background estimation we quote the uncertainty (in %) treating the two numbers as completely uncorrelated and completely correlated, respectively. Quoted uncertainties are statistical only.

1^{st} Jet Cut (GeV)	Muon Veto	Halo Jet Cut (GeV)	Expected Events Cosmics	Beam-halo	Total	Obs. Events
50	No	50	4820 ± 570	900 ± 130	5720 ± 590	5396
50	Yes	50	2.1 ± 3.6	12.1 ± 3.2	14.2 ± 4.0	10
100	Yes	50	0.4 ± 2.7	6.0 ± 1.8	6.4 ± 2.9	5
300	Yes	50	2.4 ± 2.4	0.54 ± 0.40	2.9 ± 2.4	0
100	Yes	100	1.1 ± 2.8	4.0 ± 4.0	5.0 ± 2.6	5
300	Yes	100	2.4 ± 2.4	0.36 ± 0.43	2.7 ± 2.4	0

with a Gaussian function accounting for all sources of efficiency loss and systematic uncertainty. The partial statistical correlation between the beam-halo and cosmic regions in the background determination is treated correctly as in Section 8.4. In order to retain only physically meaningful solutions the fitted values are not allowed to fluctuate below zero. More details and double checks are show in Appendix A.4.1. The inputs to the limit setting algorithms is shown in Table 12.2, the output in Table 12.3.

Each limit is interpreted using the stopping and reconstruction efficiency of a generated signal point from Tables 6.1 and 6.2. The samples with a gluino decay in equal proportions to $g\tilde{\chi}^0$ and to $q\bar{q}\tilde{\chi}^0$. The reconstruction efficiency does not differ significantly for these two processes, so we assume that they are equal.

Table 12.3: Limits on the number of produced gluinos pairs for all the signal points studied, for lifetime in the plateau efficiency region. The limits include the efficiencies of stopping, timing, reconstruction and accidental muon veto. The systematics include all the statistical uncertainties on the above efficiencies as well as nuclear cross section and mass dependent effects on timing.

1^{st} Jet	Stopping	Final	Mass (GeV)		Expected Limits (Events)			Observed Limit (Events)	
(GeV)	Model	Quarks	$\tilde{g}$	$\tilde{\chi}^0$	-1σ	Median	$+1\sigma$	Produced	In S.R.
100	Generic	gqq	600	200	3541	5424	8371	4759	7.42
100	Generic	gqq	600	300	3673	5626	8682	4937	7.41
100	Generic	gqq	600	400	4265	6534	10086	5733	7.43
100	Generic	gqq	600	450	5204	7976	12319	6997	7.47
100	Generic	gqq	600	480	7191	11046	17126	9683	7.69
100	Generic	gqq	400	100	3973	6092	9417	5343	7.52
100	Generic	gqq	600	100	3714	5694	8799	4995	7.50
100	Generic	gqq	800	100	3611	5537	8559	4857	7.51
100	Generic	gqq	1000	100	3763	5767	8907	5059	7.47
100	Generic	gqq	400	300	67667	111663	191457	95490	32.29
100	Generic	gqq	600	500	28148	45237	74883	39033	16.36
100	Generic	gqq	800	700	16914	26541	42496	23090	10.46
100	Generic	gqq	1000	900	12858	20116	32067	17519	9.97
100	Generic	tt	600	100	5771	8868	13754	7772	7.72
100	Generic	tt	800	100	5655	8684	13455	7613	7.65
100	Generic	tt	1000	100	5907	9059	14011	7945	7.54
100	Generic	tt	400	20	6638	10202	15830	8941	7.75
100	Generic	tt	600	220	5771	8856	13708	7765	7.60
100	Generic	tt	800	420	6843	10505	16270	9211	7.63
100	Generic	tt	1000	620	6507	9989	15472	8758	7.63
100	Inter.	gqq	400	100	11367	17440	26987	15294	7.58
100	Inter.	gqq	600	100	10862	16650	25725	14606	7.49
100	Inter.	gqq	800	100	11497	17624	27230	15460	7.49
100	Inter.	gqq	1000	100	13131	20138	31138	17662	7.53
100	Regge	gqq	400	100	7849	12036	18606	10557	7.52
100	Regge	gqq	600	100	6766	10371	16024	9098	7.49
100	Regge	gqq	800	100	6878	10563	16369	9260	7.66
100	Regge	gqq	1000	100	6895	10598	16445	9288	7.75

Table 12.4: Limits on the number of produced gluinos pairs for all the signal points studied, for lifetime in the plateau efficiency region. The limits include the efficiencies of stopping, timing, reconstruction and accidental muon veto. The systematics include all the statistical uncertainties on the above efficiencies as well as nuclear cross section and mass dependent effects on timing.

1^{st} Jet	Stopping	Final	Mass (GeV)		Expected Limits (Events)			Observed Limit (Events)	
(GeV)	Model	Quarks	$\tilde{g}$	$\tilde{\chi}^0$	-1σ	Median	$+1\sigma$	Produced	In S.R.
100	Regge	$\tilde{b}$	300	100	17144	26328	40798	23080	7.66
100	Regge	$\tilde{b}$	400	100	12058	18510	28665	16229	7.62
100	Regge	$\tilde{b}$	600	100	10831	16617	25710	14573	7.57
100	Regge	$\tilde{b}$	800	100	10266	15741	24331	13807	7.51
100	Regge	$\tilde{b}$	400	300	162905	268147	458242	229504	29.92
100	Regge	$\tilde{b}$	600	500	72734	117217	194767	101046	17.39
100	Regge	$\tilde{b}$	800	700	51428	80637	128971	70172	10.34
100	Regge	$\tilde{b}$	300	200	1575297	2705177	4885734	2282570	188.48
100	Regge	$\tilde{t}$	300	100	7986	12247	18936	10742	7.53
100	Regge	$\tilde{t}$	400	100	8268	12681	19611	11122	7.54
100	Regge	$\tilde{t}$	600	100	8437	12950	20053	11355	7.62
100	Regge	$\tilde{t}$	800	100	7963	12216	18897	10713	7.56
100	Generic	$\tilde{t}$	300	100	6099	9350	14450	8202	7.50
100	Generic	$\tilde{t}$	400	100	6728	10319	15958	9050	7.54
100	Generic	$\tilde{t}$	600	100	7051	10818	16740	9487	7.57
100	Generic	$\tilde{t}$	800	100	6677	10242	15844	8982	7.56
100	Generic	$\tilde{t}$	400	150	6331	9715	15035	8519	7.58
100	Generic	$\tilde{t}$	400	200	6148	9425	14563	8268	7.49
100	Generic	$\tilde{t}$	600	400	6142	9417	14558	8260	7.52
100	Generic	$\tilde{t}$	800	600	6304	9668	14948	8479	7.53
300	Generic	$\tilde{b}$	600	100	68526	118564	207485	46633	11.86
300	Generic	$\tilde{b}$	800	100	9764	15401	24285	7059	3.22
300	Generic	$\tilde{t}$	600	100	22568	36942	60966	15958	4.77
300	Generic	$\tilde{t}$	800	100	8559	13538	21426	6178	3.30
300	Generic	$\tilde{t}$	600	100	20659	34189	57117	14505	5.50
300	Generic	$\tilde{t}$	800	100	7010	11059	17440	5068	3.22

Table 12.5: Limits on the number of produced gluinos pairs for all the signal points studied, for lifetime in the plateau efficiency region. The limits include the efficiencies of stopping, timing, reconstruction and accidental muon veto. The systematics include all the statistical uncertainties on the above efficiencies as well as nuclear cross section and mass dependent effects on timing.

1^{st} Jet	Stopping	Final	Mass (GeV)		Expected Limits (Events)			Observed Limit (Events)	
(GeV)	Model	Quarks	$\tilde{g}$	$\tilde{\chi}^0$	-1σ	Median	$+1\sigma$	Produced	In S.R.
300	Generic	gqq	600	100	5643	9151	14937	4014	4.26
300	Generic	gqq	800	100	3173	5001	7878	2294	3.20
300	Generic	gqq	1000	100	3115	4906	7720	2254	3.18
300	Generic	tt	600	100	6335	10024	15870	4572	3.31
300	Generic	tt	800	100	5048	7975	12600	3646	3.27
300	Generic	tt	1000	100	4952	7808	12304	3581	3.21
300	Generic	tt	400	20	14568	23695	38820	10343	4.42
300	Generic	tt	600	220	10094	16223	26200	7220	3.86
300	Generic	tt	800	420	11655	18674	30045	8351	3.74
300	Generic	tt	1000	620	12153	19638	31926	8663	4.10
300	Inter.	gqq	600	100	14912	23861	38330	10693	3.69
300	Inter.	gqq	800	100	10357	16322	25706	7491	3.20
300	Inter.	gqq	1000	100	11247	17734	27944	8134	3.21
300	Regge	gqq	600	100	9453	15194	24544	6760	3.87
300	Regge	gqq	800	100	6001	9454	14882	4341	3.19
300	Regge	gqq	1000	100	5717	9026	14247	4132	3.24

Table 12.6: Comparison of observed and expected limits for different uncertainties on the signal efficiencies. All rows show an 800 GeV decaying to a 100 GeV $\tilde{\chi}^0$ and light quarks. The fractional signal efficiency uncertainty used in the final reported limits is 16.6%. A significantly smaller signal efficiency uncertainty was chosen to gauge the effect.

1^{st} Jet Cut (GeV)	Fractional Signal Error	Expected Limits (Events) -2σ	-1σ	Median	$+1\sigma$	$+2\sigma$	Observed Limit (Events)
100	16.6 %	2395	3771	6939	11473	17353	6100
100	1.6 %	2235	3503	6387	10427	15535	5628
300	16.6 %	2679	3705	5843	9210	13846	2679
300	1.6 %	2499	3441	5383	8391	12447	2499

Table 12.7: The Bayesian limits on the gluino massed for different signal models, assuming the lifetime is between 10^{-5} and 10^3 seconds.

1^{st} Jet Cut (GeV)	Stopping Model	Decay Process	$m_{\tilde{\chi}^0}$ (GeV)	Limits on $m_{\tilde{g}}$ (GeV) Expected	Observed
100	Generic	$\tilde{g} \rightarrow g/q\bar{q} + \tilde{\chi}^0$	100	744.5	757.5
300	Generic	$\tilde{g} \rightarrow g/q\bar{q} + \tilde{\chi}^0$	100	731.1	831.8
100	Generic	$\tilde{g} \rightarrow g/q\bar{q} + \tilde{\chi}^0$	$m_{\tilde{g}} - 100$	525.8	545.0
100	Generic	$\tilde{g} \rightarrow t\bar{t} + \tilde{\chi}^0$	100	702.0	714.4
300	Generic	$\tilde{g} \rightarrow t\bar{t} + \tilde{\chi}^0$	100	699.6	783.9
100	Generic	$\tilde{g} \rightarrow t\bar{t} + \tilde{\chi}^0$	$m_{\tilde{g}} - 380$	693.5	704.7
300	Generic	$\tilde{g} \rightarrow t\bar{t} + \tilde{\chi}^0$	$m_{\tilde{g}} - 380$	643.6	712.2
100	Generic	$\tilde{t} \rightarrow t + \tilde{\chi}^0$	100	384.3	392.0
300	Generic	$\tilde{t} \rightarrow t + \tilde{\chi}^0$	100	–	–
100	Generic	$\tilde{t} \rightarrow t + \tilde{\chi}^0$	$m_{\tilde{t}} - 200$	389.1	397.3
100	Intermediate	$\tilde{g} \rightarrow g/q\bar{q} + \tilde{\chi}^0$	100	643.1	654.3
300	Intermediate	$\tilde{g} \rightarrow g/q\bar{q} + \tilde{\chi}^0$	100	615.1	698.5
100	Regge	$\tilde{g} \rightarrow g/q\bar{q} + \tilde{\chi}^0$	100	685.9	697.9
300	Regge	$\tilde{g} \rightarrow g/q\bar{q} + \tilde{\chi}^0$	100	663.6	758.2
100	Regge	$\tilde{t} \rightarrow t + \tilde{\chi}^0$	100	371.3	379.1
300	Regge	$\tilde{t} \rightarrow t + \tilde{\chi}^0$	100	–	–
100	Regge	$\tilde{b} \rightarrow b + \tilde{\chi}^0$	100	334.2	343.5
300	Regge	$\tilde{b} \rightarrow b + \tilde{\chi}^0$	100	–	–
100	Regge	$\tilde{b} \rightarrow b + \tilde{\chi}^0$	$m_{\tilde{b}} - 100$	–	–

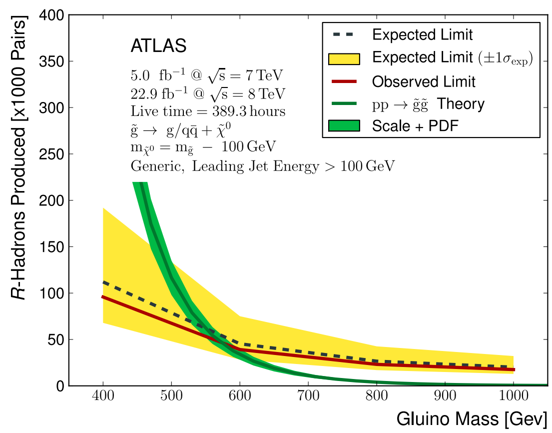

(a) Generic Interaction Model with fixed mass splitting of 100 GeV

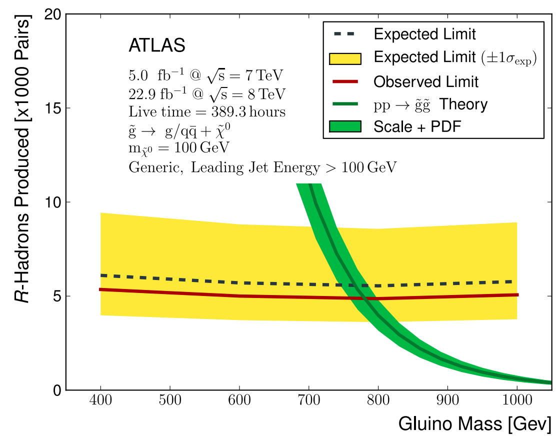

(b) Generic Interaction Model with fixed LSP mass at 100 GeV

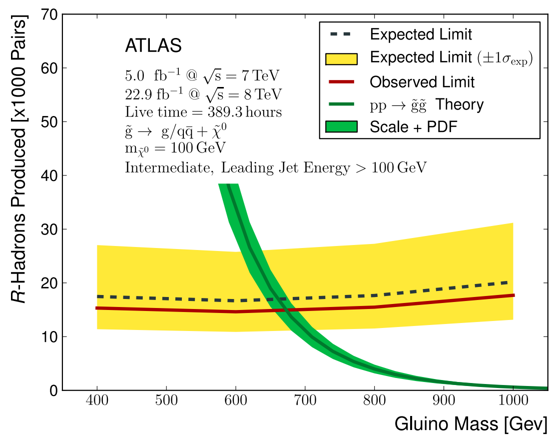

(c) Intermediate Matter Interaction Model fixed LSP mass at 100 GeV

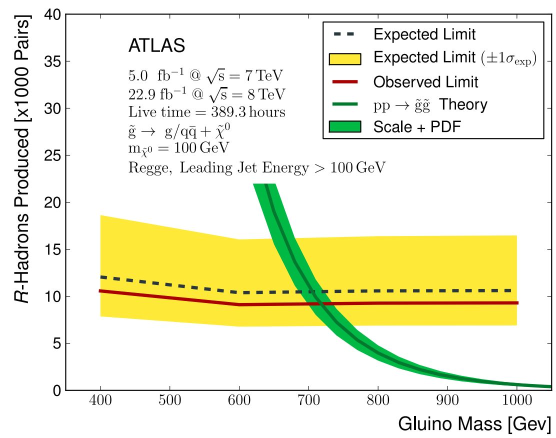

(d) Regge Matter Interaction Model fixed LSP mass at 100 GeV

Figure 12.1: Plots of the Bayesian upper production limits versus gluino mass for several signal models, with $g/q\bar{q}$ final state. The gluino lifetime is between 10^{-5} and 10^{3} seconds. The limit in these plots come from the jet energy > 100 GeV signal region.

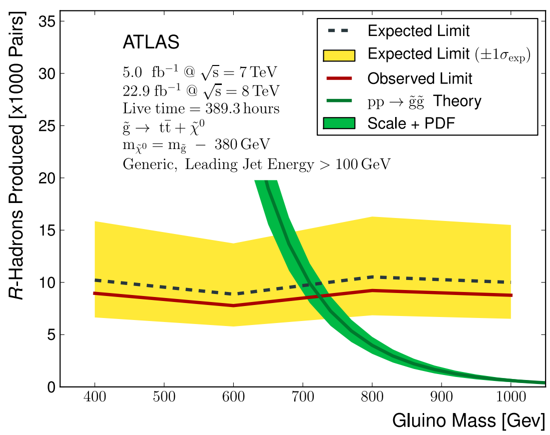

(a) Generic Interaction Model fixed mass splitting of 380 GeV

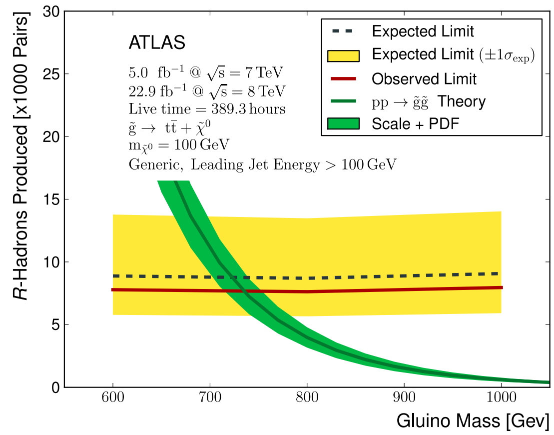

(b) Generic Interaction Model fixed LSP mass at 100 GeV

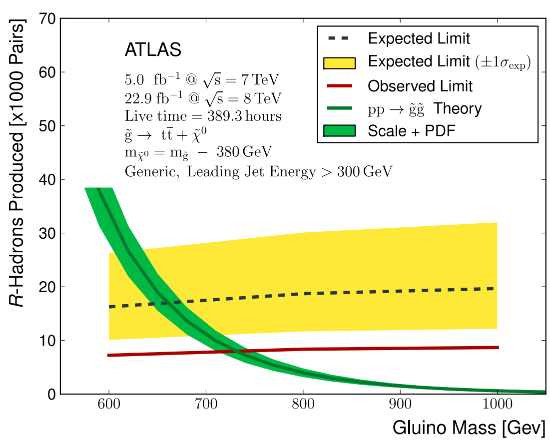

(c) Generic Interaction Model fixed mass splitting of 380 GeV

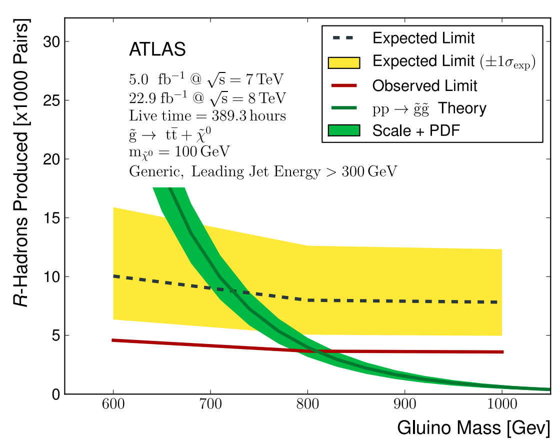

(d) Generic Interaction Model fixed LSP mass at 100 GeV

Figure 12.2: Plots of the Bayesian upper production limits versus gluino mass for several signal models, with $t\bar{t}$ final state. The gluino lifetime is between 10^{-5} and 10^3 seconds. The limit in these plots come from the jet energy > 100 GeV signal region.

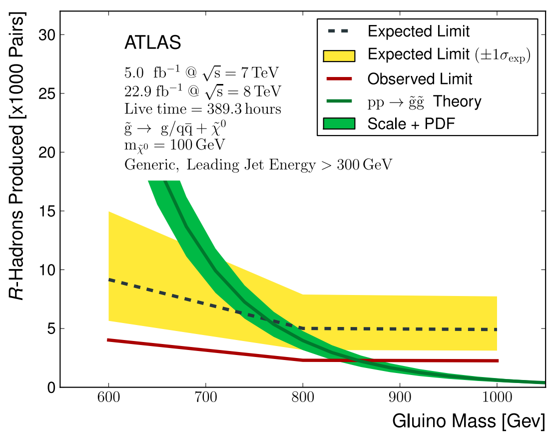

(a) Generic Interaction Model fixed LSP mass at 100 GeV

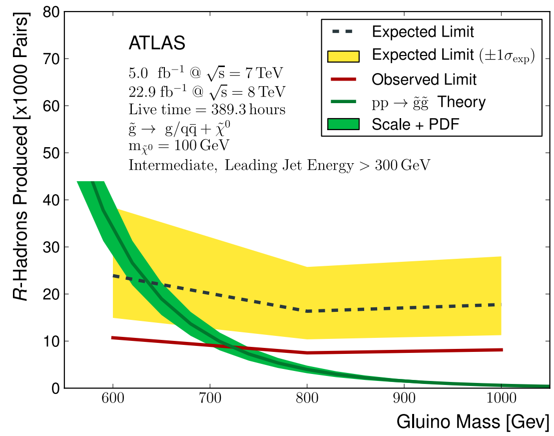

(b) Intermediate Matter Interaction Model fixed LSP mass at 100 GeV

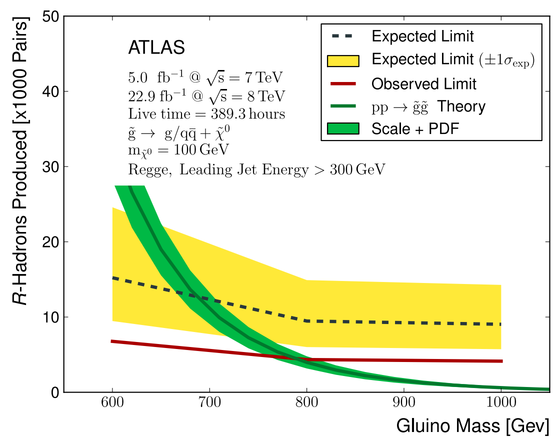

(c) Regge Matter Interaction Model fixed LSP mass at 100 GeV

Figure 12.3: Plots of the Bayesian upper production limits versus gluino mass for several signal models, with $g/q\bar{q}$ final state. The gluino lifetime is between 10^{-5} and 10^{3} seconds. The limit in these plots come from the jet energy > 300 GeV signal region.

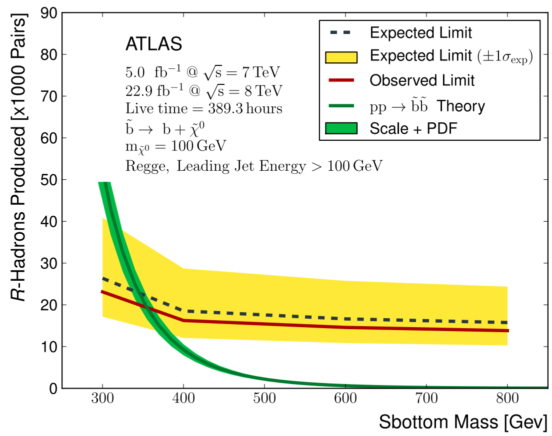

(a) Regge Interaction Model $\tilde{b} \to b\tilde{\chi}^0$ Final State with fixed LSP mass at 100 GeV

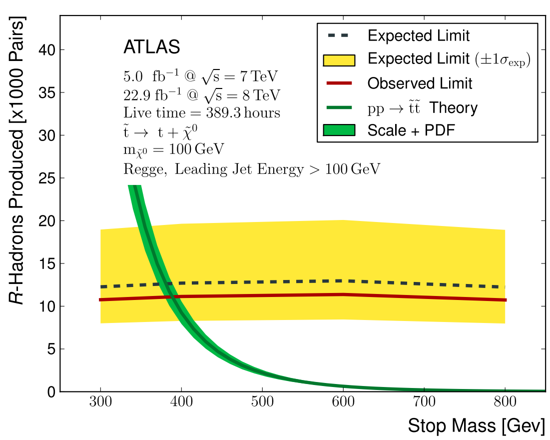

(b) Regge Interaction Model $\tilde{t} \to t\tilde{\chi}^0$ Final State with fixed LSP mass at 100 GeV

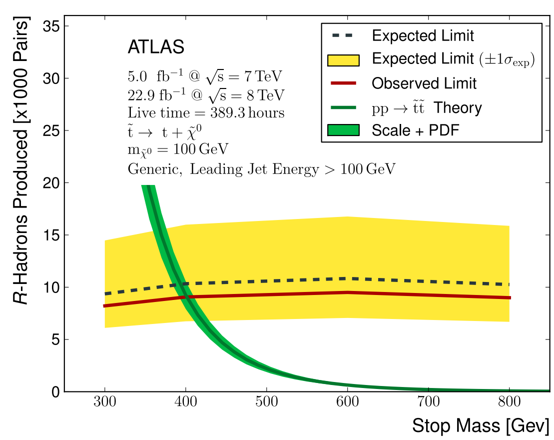

(c) Generic Interaction Model $\tilde{t} \to t\tilde{\chi}^0$ Final State with fixed LSP mass at 100 GeV

Figure 12.4: Plots of the Bayesian upper production limits versus squark mass for several signal models, for lifetime in the plateau efficiency region between 10^{-5} and 10^3 seconds. The limit in these plots come from the jet energy > 100 GeV signal region.

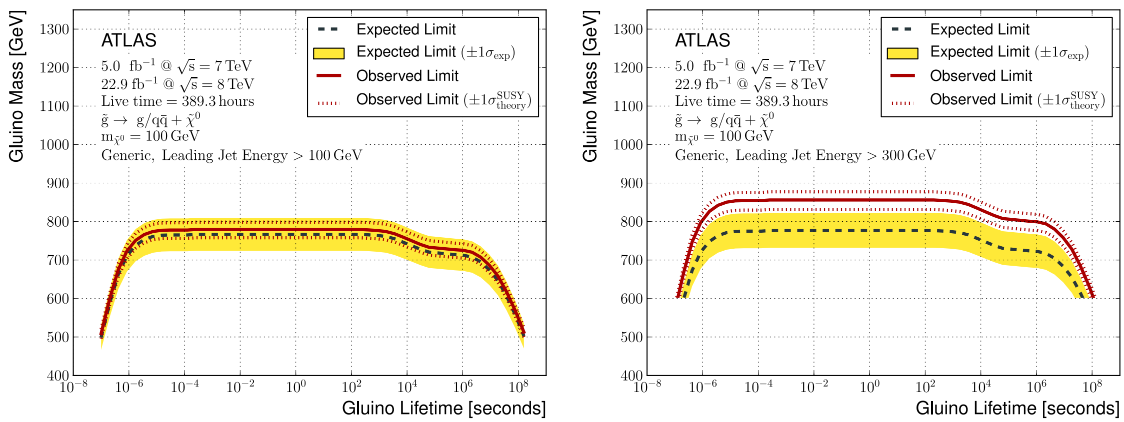

(a) Gluino Generic R-Hadron, Leading Jet Energy > 100 GeV

(b) Gluino Generic R-Hadron, Leading Jet Energy > 300 GeV

Figure 12.5: Plots of the Bayesian lower limit on gluino mass versus gluino lifetime. A 800 GeV R-hadron decaying to a 100 GeV $\tilde{\chi}^0$ was used as a reference for stopping and reconstruction efficiency.

12.2 Results as a Function of Gluino Mass

To provide limits in terms of the gluino mass, $m_{\tilde{g}}$, we calculate the cross sections at several different points then use a power law interpolation for masses not directly calculated. Note that the number of expected signal events is given by the signal cross sections at 7 and 8 TeV, weighted by their integrated luminosities in the 2011 and 2012 data. Figure 12.1 shows the limits for the various models considered. We also set mass limits for the different stopping models as can be seen in Table 12.7.

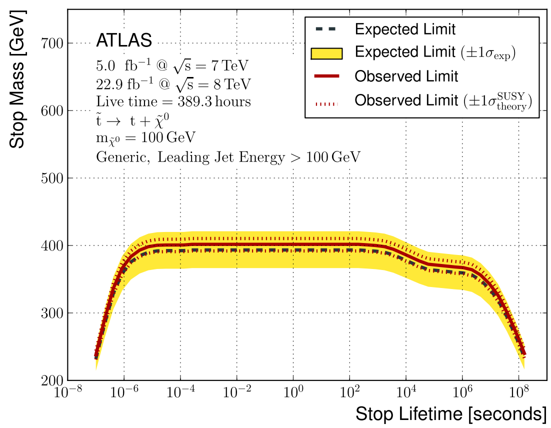

(a) Stop Generic R-Hadron, Leading Jet Energy > 100 GeV

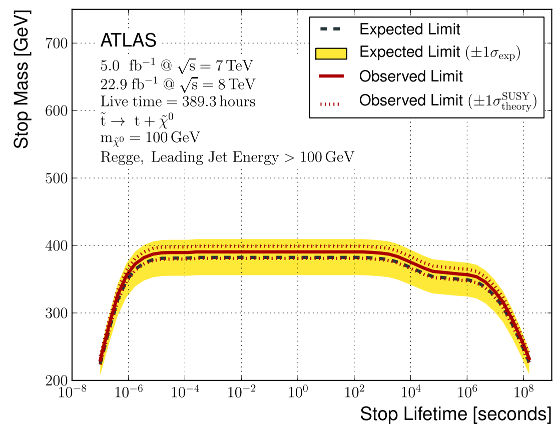

(b) Stop Regge R-Hadron, Leading Jet Energy > 100 GeV

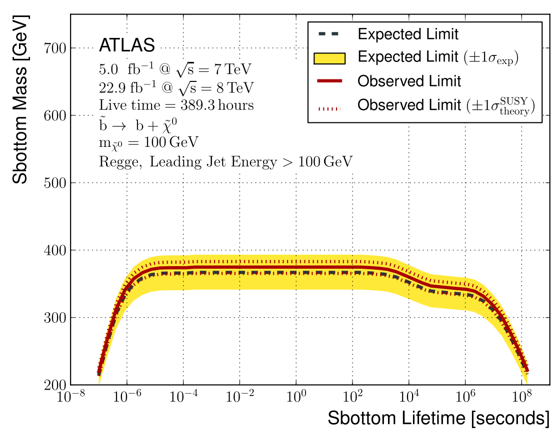

(c) Sbottom Regge R-Hadron, Leading Jet Energy > 100 GeV

Figure 12.6: Plots of the Bayesian lower limit on squark mass versus squark lifetime. A 800 GeV R-hadron decaying to a 100 GeV $\tilde{\chi}^0$ was used as a reference for stopping and reconstruction efficiency.

Chapter 13

Summary and Conclusion

We have presented an updated search using 2011 and 2012 data from the ATLAS experiment for stopped long-lived gluino R-hadrons decaying in the calorimeter, using a jet trigger operating in the empty bunch crossings of the LHC. The remaining events after all selections are compatible with the expected rate from backgrounds, predominantly cosmic and beam-halo muons of which, a muon segment was not identified in the muon detector system. Limits are set on the gluino mass, for different gluino decays and neutralino masses. With an LSP of mass 100 GeV, we exclude $m_{\tilde{g}} < 832$ GeV (731 GeV expected), for a gluino lifetime between $10\mu s$ and 1000 seconds in the generic R-hadron model with decays to $q\bar{q}\tilde{\chi}^0$ and $g\tilde{\chi}^0$. These results are currently the world's best constraints on this process.

Appendix A

Appendix

A.1 Additional Cut flow tables

A complete cut flow table is shown for all points studied in this note in Tables A.1, A.2, A.3, A.4, A.5, A.6, A.7 .

A.2 Choice of number of hits for muon segment veto

In the 2010 analysis, any (MuonBoy) muon segment would veto the event. In 2011/2012, it was found that the muon veto efficiency was too low in the random empty data for this cut, about 30% for the later half of 2012, see Figure A.1 (left). An investigation into the number of hits (measurements in either MDT, RPC, TGC, or CSC stations) that are combined on each segment showed that real muon segments from real muons tend to have more than 4 hits, whereas muon segments from noise in the random data tend to have fewer hits, see Figure A.2. Using this requirement, the efficiency in the random-triggered data rises to 75% in the latter half of 2012, see Figure A.1 (right), an increase of more than a factor of 2 in efficiency. The additional background from using this requirement was estimated in the background data sample (early 2011). An increase by a factor of 2.0 was seen for the background (19

Table A.1: Cut flow table for signal samples in the $\tilde{g} \to g/qq\tilde{\chi}^0$ decays. The cumulative efficiencies (%) are listed for each successive cut. The samples used herein correspond to the *generic* signal MC sample as described in Section 6. The gluino mass is varied while the neutralino mass is fixed to $m_{\tilde{g}} - 100\ GeV$ in all cases. The quoted uncertainties are statistical only.

	Cumulative Efficiency (%), $m_{\tilde{\chi}^0} = 100$ GeV			
Selection Criteria	$m_{\tilde{g}} = 400$ GeV	600 GeV	800 GeV	1000 GeV
Trigger	26.11 ± 0.66	26.81 ± 0.67	30.59 ± 0.71	31.45 ± 0.71
abs(jeteta[0]) < 1.2	26.11 ± 0.66	26.81 ± 0.67	30.59 ± 0.71	31.45 ± 0.71
njets < 6	26.11 ± 0.66	26.81 ± 0.67	30.59 ± 0.71	31.45 ± 0.71
njets > 0	26.11 ± 0.66	26.81 ± 0.67	30.59 ± 0.71	31.45 ± 0.71
met/jetpt[0] > .5	26.11 ± 0.66	26.81 ± 0.67	30.59 ± 0.71	31.45 ± 0.71
passed_larg_noise	26.11 ± 0.66	26.81 ± 0.67	30.59 ± 0.71	31.45 ± 0.71
n90[0]>3	21.54 ± 0.61	21.28 ± 0.62	24.19 ± 0.66	24.79 ± 0.66
jetwidth[0]>0.04	5.81 ± 0.35	7.67 ± 0.40	7.43 ± 0.40	8.41 ± 0.43
jetFracTile[0]>0.5	5.10 ± 0.33	6.16 ± 0.36	6.04 ± 0.37	7.04 ± 0.39
jete[0] > 50	5.10 ± 0.33	6.16 ± 0.36	6.04 ± 0.37	7.04 ± 0.39
Muon Veto	4.92 ± 0.32	5.86 ± 0.35	5.71 ± 0.36	6.83 ± 0.39
jete[0] > 100	3.38 ± 0.27	4.19 ± 0.30	4.53 ± 0.32	5.69 ± 0.36
jete[0] > 300	0.00 ± 0.00	0.00 ± 0.00	0.00 ± 0.00	0.00 ± 0.00

Table A.2: Cut flow table for signal samples in the $\tilde{g} \to t\bar{t}\tilde{\chi}^0$ decays. The cumulative efficiencies (%) are listed for each successive cut. The samples used herein correspond to the *generic* signal MC sample as described in Section 6. The gluino mass is varied while the neutralino mass is fixed to 100 GeV in all cases. The quoted uncertainties are statistical only.

	Cumulative Efficiency (%), $m_{\tilde{\chi}^0} = 100$ GeV		
Selection Criteria	$m_{\tilde{g}} = 600$ GeV	800 GeV	1000 GeV
Trigger	68.88 ± 0.70	72.79 ± 0.68	74.81 ± 0.68
abs(jeteta[0]) < 1.2	60.74 ± 0.74	63.13 ± 0.74	63.97 ± 0.75
njets < 6	60.18 ± 0.74	62.07 ± 0.75	62.68 ± 0.75
njets > 0	60.18 ± 0.74	62.07 ± 0.75	62.68 ± 0.75
met/jetpt[0] $> .5$	60.18 ± 0.74	62.07 ± 0.75	62.63 ± 0.75
passed_larg_noise	60.18 ± 0.74	62.07 ± 0.75	62.63 ± 0.75
n90[0]>3	57.80 ± 0.75	59.48 ± 0.75	59.43 ± 0.76
jetwidth[0]>0.04	28.16 ± 0.68	29.76 ± 0.70	31.62 ± 0.72
jetFracTile[0]>0.5	20.71 ± 0.62	23.04 ± 0.65	24.19 ± 0.67
jete[0] > 50	20.71 ± 0.62	23.04 ± 0.65	24.19 ± 0.67
Muon Veto	9.97 ± 0.46	10.08 ± 0.46	9.49 ± 0.46
jete[0] > 100	9.93 ± 0.45	10.05 ± 0.46	9.49 ± 0.46
jete[0] > 300	7.24 ± 0.39	8.95 ± 0.44	8.95 ± 0.44

Table A.3: Cut flow table for signal samples in the $\tilde{g} \to t\bar{t}\tilde{\chi}^0$ decays. The cumulative efficiencies (%) are listed for each successive cut. The samples used herein correspond to the *generic* signal MC sample as described in Section 6. The gluino mass is varied while the neutralino mass is fixed to $m_{\tilde{g}} - 380\ GeV$ in all cases. The quoted uncertainties are statistical only.

	Cumulative Efficiency (%), $m_{\tilde{\chi}^0} = 100$ GeV			
Selection Criteria	$m_{\tilde{g}} = 400$	600 GeV	800 GeV	1000 GeV
Trigger	65.57 ± 0.70	67.25 ± 0.70	65.92 ± 0.71	67.73 ± 0.72
abs(jeteta[0]) < 1.2	56.74 ± 0.73	58.21 ± 0.74	57.21 ± 0.75	59.38 ± 0.76
njets < 6	56.50 ± 0.73	57.83 ± 0.74	57.01 ± 0.75	59.12 ± 0.76
njets > 0	56.50 ± 0.73	57.83 ± 0.74	57.01 ± 0.75	59.12 ± 0.76
met/jetpt[0] > .5	56.50 ± 0.73	57.83 ± 0.74	57.01 ± 0.75	59.12 ± 0.76
passed_larg_noise	56.50 ± 0.73	57.83 ± 0.74	57.01 ± 0.75	59.12 ± 0.76
n90[0]>3	54.51 ± 0.74	55.91 ± 0.74	55.35 ± 0.75	56.61 ± 0.76
jetwidth[0]>0.04	26.08 ± 0.65	26.02 ± 0.66	24.91 ± 0.65	26.05 ± 0.68
jetFracTile[0]>0.5	18.45 ± 0.57	19.02 ± 0.59	17.52 ± 0.57	18.97 ± 0.60
jete[0] > 50	18.45 ± 0.57	19.02 ± 0.59	17.52 ± 0.57	18.97 ± 0.60
Muon Veto	8.72 ± 0.42	9.82 ± 0.45	8.33 ± 0.42	8.71 ± 0.43
jete[0] > 100	8.66 ± 0.42	9.78 ± 0.44	8.28 ± 0.42	8.71 ± 0.43
jete[0] > 300	4.27 ± 0.30	5.35 ± 0.34	4.48 ± 0.31	4.73 ± 0.33

Table A.4: Cut flow table for signal samples in the $\tilde{g} \rightarrow g/qq\tilde{\chi}^0$ decays. The cumulative efficiencies (%) are listed for each successive cut. The samples used herein correspond to the *intermediate* signal MC sample as described in Section 6. The gluino mass is varied while the neutralino mass is fixed to 100 GeV in all cases. The quoted uncertainties are statistical only.

	Cumulative Efficiency (%), $m_{\tilde{\chi}^0} = 100$ GeV			
Selection Criteria	$m_{\tilde{g}} = 400$ GeV	600 GeV	800 GeV	1000 GeV
Trigger	46.63 ± 0.72	54.95 ± 0.70	57.53 ± 0.70	58.56 ± 0.71
abs(jeteta[0]) < 1.2	42.25 ± 0.71	48.23 ± 0.71	49.94 ± 0.71	51.23 ± 0.72
njets < 6	42.25 ± 0.71	47.99 ± 0.71	49.11 ± 0.71	49.83 ± 0.72
njets > 0	42.25 ± 0.71	47.99 ± 0.71	49.11 ± 0.71	49.83 ± 0.72
met/jetpt[0] > .5	42.25 ± 0.71	47.61 ± 0.71	47.64 ± 0.71	48.16 ± 0.72
passed_larg_noise	42.25 ± 0.71	47.61 ± 0.71	47.64 ± 0.71	48.16 ± 0.72
n90[0]>3	37.75 ± 0.70	43.83 ± 0.70	44.16 ± 0.70	44.93 ± 0.72
jetwidth[0]>0.04	20.78 ± 0.58	26.94 ± 0.63	26.76 ± 0.63	28.28 ± 0.65
jetFracTile[0]>0.5	10.39 ± 0.44	11.85 ± 0.46	11.72 ± 0.46	11.87 ± 0.47
jete[0] > 50	10.39 ± 0.44	11.85 ± 0.46	11.72 ± 0.46	11.87 ± 0.47
Muon Veto	8.69 ± 0.41	9.01 ± 0.40	8.46 ± 0.39	7.45 ± 0.38
jete[0] > 100	8.63 ± 0.40	8.93 ± 0.40	8.44 ± 0.39	7.43 ± 0.38
jete[0] > 300	0.394 ± 0.090	6.02 ± 0.34	7.43 ± 0.37	6.87 ± 0.37

Table A.5: Cut flow table for signal samples in the $\tilde{g} \to g/qq\tilde{\chi}^0$ decays. The cumulative efficiencies (%) are listed for each successive cut. The samples used herein correspond to the *regge* signal MC sample as described in Section 6. The gluino mass is varied while the neutralino mass is fixed to 100 GeV in all cases. The quoted uncertainties are statistical only.

	Cumulative Efficiency (%), $m_{\tilde{\chi}^0} = 100$ GeV			
Selection Criteria	$m_{\tilde{g}} = 400$ GeV	600 GeV	800 GeV	1000 GeV
Trigger	67.65 ± 0.74	78.02 ± 0.66	82.86 ± 0.60	84.86 ± 0.56
abs(jeteta[0]) < 1.2	62.48 ± 0.77	70.14 ± 0.72	74.18 ± 0.69	74.10 ± 0.69
njets < 6	62.48 ± 0.77	70.04 ± 0.73	73.93 ± 0.69	73.17 ± 0.69
njets > 0	62.48 ± 0.77	70.04 ± 0.73	73.93 ± 0.69	73.17 ± 0.69
met/jetpt[0] > .5	62.48 ± 0.77	69.84 ± 0.73	73.66 ± 0.70	72.68 ± 0.70
passed_larg_noise	62.48 ± 0.77	69.84 ± 0.73	73.66 ± 0.70	72.68 ± 0.70
n90[0]>3	57.80 ± 0.78	65.19 ± 0.75	68.85 ± 0.73	68.73 ± 0.73
jetwidth[0]>0.04	31.97 ± 0.74	39.20 ± 0.77	42.65 ± 0.78	44.70 ± 0.78
jetFracTile[0]>0.5	19.65 ± 0.63	24.32 ± 0.68	26.22 ± 0.69	27.86 ± 0.70
jete[0] > 50	19.65 ± 0.63	24.32 ± 0.68	26.22 ± 0.69	27.86 ± 0.70
Muon Veto	17.01 ± 0.60	19.37 ± 0.63	19.46 ± 0.63	19.56 ± 0.62
jete[0] > 100	16.70 ± 0.59	19.30 ± 0.63	19.41 ± 0.62	19.56 ± 0.62
jete[0] > 300	0.66 ± 0.13	13.43 ± 0.54	17.21 ± 0.60	18.41 ± 0.61

Table A.6: Cut flow table for signal samples in the $\tilde{g} \rightarrow g/qq\tilde{\chi}^0$ decays. The cumulative efficiencies (%) are listed for each successive cut. The samples used herein correspond to the *generic* signal MC sample as described in Section 6. The gluino mass is fixed while the neutralino mass varies in all cases. The quoted uncertainties are statistical only.

	Cumulative Efficiency (%), $m_{\tilde{g}} = 600$ GeV				
Selection Criteria	$m_{\tilde{\chi}^0} = 480$ GeV	450 GeV	400 GeV	300 GeV	200 GeV
Trigger	38.23 ± 0.33	48.82 ± 0.34	57.54 ± 0.34	64.82 ± 0.33	67.49 ± 0.32
abs(jeteta[0]) < 1.2	38.16 ± 0.33	46.70 ± 0.34	51.53 ± 0.34	56.62 ± 0.34	58.65 ± 0.34
njets < 6	38.16 ± 0.33	46.70 ± 0.34	51.53 ± 0.34	56.62 ± 0.34	58.65 ± 0.34
njets > 0	38.16 ± 0.33	46.70 ± 0.34	51.53 ± 0.34	56.62 ± 0.34	58.65 ± 0.34
met/jetpt[0] > .5	38.16 ± 0.33	46.70 ± 0.34	51.53 ± 0.34	56.62 ± 0.34	58.64 ± 0.34
n90[0]>3	31.26 ± 0.31	38.40 ± 0.33	44.09 ± 0.34	50.15 ± 0.34	52.60 ± 0.34
jetwidth[0]>0.04	11.50 ± 0.22	15.58 ± 0.25	19.74 ± 0.27	24.72 ± 0.30	26.58 ± 0.30
jetFracTile[0]>0.5	9.17 ± 0.19	11.99 ± 0.22	14.87 ± 0.24	18.31 ± 0.26	19.90 ± 0.27
jete[0] > 50	9.17 ± 0.19	11.99 ± 0.22	14.87 ± 0.24	18.31 ± 0.26	19.90 ± 0.27
Muon Veto	8.79 ± 0.19	11.22 ± 0.22	13.34 ± 0.23	15.15 ± 0.25	15.69 ± 0.25
jete[0] > 100	7.94 ± 0.18	10.67 ± 0.21	12.96 ± 0.23	15.01 ± 0.24	15.59 ± 0.25
jete[0] > 300	0.0 ± 0.0	0.0 ± 0.0	0.0047 ± 0.0047	1.554 ± 0.085	8.41 ± 0.19

	Cumulative Efficiency (%), $m_{\tilde{g}} = 600$ GeV		
Selection Criteria	$m_{\tilde{\chi}^0} = 560$ GeV	540 GeV	520 GeV
Trigger	0.0 ± 0.000031	0.439 ± 0.045	8.99 ± 0.19
abs(jeteta[0]) < 1.2	0.0 ± 0.000031	0.439 ± 0.045	8.99 ± 0.19
njets < 6	0.0 ± 0.000031	0.439 ± 0.045	8.99 ± 0.19
njets > 0	0.0 ± 0.000031	0.439 ± 0.045	8.99 ± 0.19
met/jetpt[0] > .5	0.0 ± 0.000031	0.439 ± 0.045	8.99 ± 0.19
n90[0]>3	0.0 ± 0.000031	0.261 ± 0.035	6.17 ± 0.16
jetwidth[0]>0.04	0.0 ± 0.000031	0.078 ± 0.019	1.985 ± 0.095
jetFracTile[0]>0.5	0.0 ± 0.000031	0.078 ± 0.019	1.874 ± 0.092
jete[0] > 50	0.0 ± 0.000031	0.078 ± 0.019	1.874 ± 0.092
Muon Veto	0.0 ± 0.000031	0.078 ± 0.019	1.823 ± 0.091
jete[0] > 100	0.0 ± 0.000031	0.0046 ± 0.0046	0.320 ± 0.038
jete[0] > 300	0.0 ± 0.000031	0.0 ± 0.000031	0.0± 0.000032

Table A.7: Cut flow table for signal samples in the $\tilde{q} \to q\tilde{\chi}^0$ decays. The cumulative efficiencies (%) are listed for each successive cut. The samples used herein correspond to the signal MC samples as described in Section 6. The squark mass is fixed to $m_{\tilde{q}} =$ 400 GeV and neutralino mass $m_{\tilde{\chi}^0} = 100$ GeV all cases. The quoted uncertainties are statistical only.

	Cumulative Efficiency (%)		
Selection Criteria	Regge $\tilde{t}$	Generic $\tilde{t}$	Regge $\tilde{b}$
Trigger	47.70 ± 0.71	49.22 ± 0.71	63.14 ± 0.68
abs(jeteta[0]) < 1.2	43.12 ± 0.70	44.68 ± 0.70	58.20 ± 0.70
njets < 6	43.12 ± 0.70	44.68 ± 0.70	58.20 ± 0.70
njets > 0	43.12 ± 0.70	44.68 ± 0.70	58.20 ± 0.70
met/jetpt[0] > .5	43.12 ± 0.70	44.68 ± 0.70	58.20 ± 0.70
n90[0]>3	39.42 ± 0.69	41.44 ± 0.70	51.12 ± 0.71
jetwidth[0]>0.04	22.38 ± 0.59	21.76 ± 0.58	32.42 ± 0.66
jetFracTile[0]>0.5	13.36 ± 0.48	14.14 ± 0.49	11.72 ± 0.45
jete[0] > 50	13.36 ± 0.48	14.14 ± 0.49	11.72 ± 0.45
Muon Veto	9.74 ± 0.42	10.52 ± 0.43	9.50 ± 0.41
jete[0] > 100	9.24 ± 0.41	9.98 ± 0.42	9.18 ± 0.41
jete[0] > 300	0.120 ± 0.049	0.040 ± 0.028	0.020 ± 0.020

events with no muon segments and 19 additional events observed with at least one segment with 4 or fewer hits), see Figure A.3. The significance of a signal would thus be enhanced by S/sqrt(B) of about 1.5 using the Nhits>4 requirement. Alternative cuts, say >3 or >5, showed slightly worse S/sqrt(B) improvements.

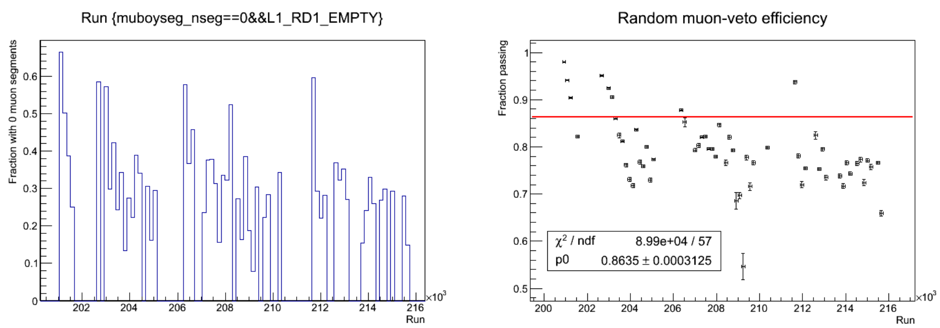

Figure A.1: The muon veto efficiency for random-triggered data in 2012 using all muon segments (left) and only those with at least 5 hits (right).

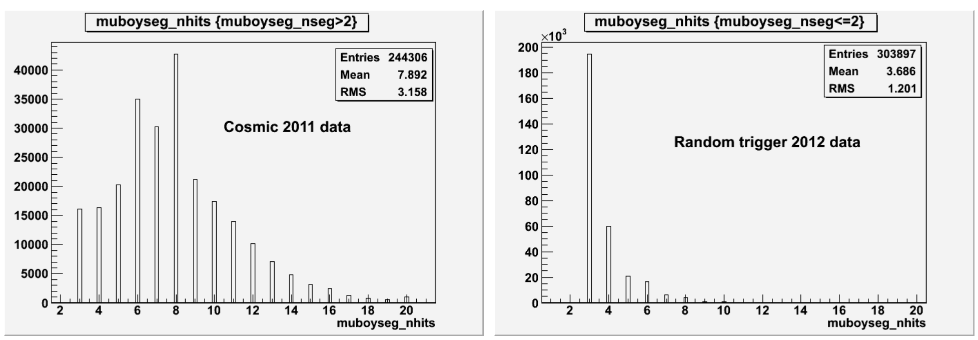

Figure A.2: The number of muon hits on each muon segment in data from cosmic muon events (left), which are mostly real muon segments, and from random-triggered data, which are mostly noise or background.

A.3 TileCal Dead Fraction

There are two possible effects from TileCal trips: potentially appreciable loss in detector livetime (and thus signal efficiency) and the loss of energy in a candidate

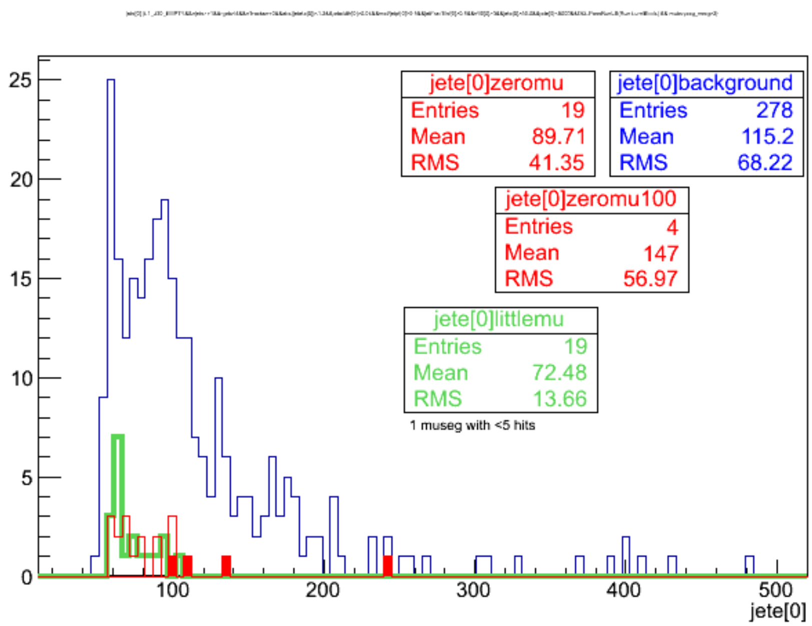

Figure A.3: Energy of jets in the background control region. Blue is cosmic data with good muons, red have no muon segments. The additional background from only vetoing muon segments with more than 4 hits is shown as the green histogram.

Table A.8: The candidate events that occurred in the same run and luminosity block as a TileCal trip. The sector refers to the segment (geometric and readout) affected by the trip.

Run	LumiBlock	Jet E (GeV)	$\Delta\phi$ Sector-Jet	Jet η	Sector
208982	682	101.61	1.92	-0.72	LBA37
209629	388	99.92	0.19	-0.05	LBC19
211670	232	89.61	1.83	0.15	EBC62
214777	660	135.27	2.99	0.06	LBC37

jet. To quantify the first effect, we use the average trip per pb^{-1}(0.6 pb) found elsewhere [47]. Examining all the 2012 periods, we find that period G has the average rate of luminosity, so we focus on it as a worst case scenario (Table 5.2). We would expect a total of 870 trips in 94 hours of running. If each trip takes 60 seconds to correct and disables one-tenth the calorimeter, then the detector live time drops by less than 2%. But one-tenth is probably too big as each trip takes the one sector, of which there are over 100 in the central barrel of the TileCal. This effect gets washed away in other timing systematics.

The next possible effect deals with loss of energy in a candidate event. We look at all events with jet energy greater than 50 GeV, which passed the muon veto, for both the cosmic and search regions in Table A.8. The list of trips was accessed directly from [48]. Of particular interest, is the event in run 209629. It occurred in the adjacent phi-sector of the trip and is 100 MeV short of being put into the 100 GeV sideband for background estimation. No corrupted events remained after the muon veto [49].

A.4 Limit Setting Double Checks

The limits quoted in the final results employ a flat prior which is known to have theoretical problems. To check the sensitivity to this shape of the prior, we use a Poisson prior following Ref [41]. The flat prior always provides a conservative limit and for the three test points, is within 10% of the Poisson-prior limit as seen in

Table A.9: The 95% upper limit on the number of events detected in the signal region. Limits were calculated and compared with based a flat or Poisson prior on the signal strength.

Number of Events		95% Upper Limit	
Background Expected	Observed	Poisson Prior	Flat Prior
14.2 ± 4.8	10	8.63	8.92
6.4 ± 3.2	5	6.87	7.24
2.9 ± 2.4	0	2.81	3.02

Table A.9.

A.4.1 Bayesian Confidence Interval

We used a set of 5000 pseudo-experiments to construct the median and $\pm 1\sigma$ bands shown in Figures 12.1,12.2,12.4,12.5 and 12.6. Each pseudo-experiment uses the same efficiency and background estimate but picks a new number of observed limits from a Poisson distribution smeared by a Gaussian for the background uncertainty. However in the 300 GeV case no pseudo-experiment can chose fewer than 0 events, which truncates the distribution of upper limits as seen in Figure A.4. Since the distribution of upper limits (Figure A.4(a)) is truncated on the left, it is not possible to find an upper limit 2σ to the left of the median. In fact, the -2σ and observed limits are only 1.15σ below the median.

A.5 Linear Versions of Plots

Figures A.5,A.6 correspond to Figures 7.1,7.2.

A.6 g vs $q\bar{q}$ Decays

Table A.10: The selection efficiency after all cuts have been applied for all signal samples. The quoted uncertainties are statistical only.

Leading Jet	Stopping	Mass (GeV)		Final State	
Cut (GeV)	Model	$\tilde{g}$	$\tilde{\chi}^0$	$g\tilde{\chi}^0$	$q\bar{q}\tilde{\chi}^0$
100	Generic	400	100	12.10 $\pm$ 0.65 %	16.40 $\pm$ 0.81 %
100	Generic	600	100	13.79 $\pm$ 0.75 %	16.30 $\pm$ 0.78 %
100	Generic	800	100	13.88 $\pm$ 0.82 %	16.50 $\pm$ 0.76 %
100	Generic	1000	100	13.87 $\pm$ 0.90 %	15.34 $\pm$ 0.75 %
100	Generic	400	300	3.25 $\pm$ 0.28 %	4.8 $\pm$ 1.0 %
100	Generic	600	500	4.02 $\pm$ 0.30 %	6.7 $\pm$ 1.6 %
100	Generic	800	700	4.46 $\pm$ 0.32 %	6.2 $\pm$ 1.8 %
100	Generic	1000	900	5.56 $\pm$ 0.36 %	9.2 $\pm$ 2.3 %
100	Inter.	400	100	7.66 $\pm$ 0.52 %	9.83 $\pm$ 0.64 %
100	Inter.	600	100	7.92 $\pm$ 0.56 %	9.85 $\pm$ 0.59 %
100	Inter.	800	100	7.33 $\pm$ 0.55 %	9.32 $\pm$ 0.57 %
100	Inter.	1000	100	7.30 $\pm$ 0.61 %	7.55 $\pm$ 0.49 %
100	Regge	400	100	13.92 $\pm$ 0.73 %	20.53 $\pm$ 0.99 %
100	Regge	600	100	17.21 $\pm$ 0.86 %	21.09 $\pm$ 0.91 %
100	Regge	800	100	17.71 $\pm$ 0.92 %	20.76 $\pm$ 0.86 %
100	Regge	1000	100	17.53 $\pm$ 0.98 %	21.05 $\pm$ 0.81 %
300	Generic	400	100	0.040 $\pm$ 0.040%	0.95 $\pm$ 0.21 %
300	Generic	600	100	8.57 $\pm$ 0.61 %	12.63 $\pm$ 0.70 %
300	Generic	800	100	12.17 $\pm$ 0.78 %	15.08 $\pm$ 0.73 %
300	Generic	1000	100	12.93 $\pm$ 0.87 %	14.83 $\pm$ 0.73 %
300	Generic	400	300	0.00 $\pm$ 0.00039%	0.00 $\pm$ 0.012%
300	Generic	600	500	0.00 $\pm$ 0.00037%	0.00 $\pm$ 0.025%
300	Generic	800	700	0.00 $\pm$ 0.00039%	0.00 $\pm$ 0.042%
300	Generic	1000	900	0.00 $\pm$ 0.00039%	0.00 $\pm$ 0.053%
300	Inter.	400	100	0.116 $\pm$ 0.067%	0.73 $\pm$ 0.18 %
300	Inter.	600	100	4.74 $\pm$ 0.44 %	7.21 $\pm$ 0.51 %
300	Inter.	800	100	6.48 $\pm$ 0.52 %	8.14 $\pm$ 0.53 %
300	Inter.	1000	100	6.53 $\pm$ 0.58 %	7.11 $\pm$ 0.47 %
300	Regge	400	100	0.00 $\pm$ 0.00093%	1.55 $\pm$ 0.30 %
300	Regge	600	100	10.74 $\pm$ 0.71 %	15.90 $\pm$ 0.82 %
300	Regge	800	100	14.97 $\pm$ 0.86 %	19.01 $\pm$ 0.83 %
300	Regge	1000	100	16.12 $\pm$ 0.95 %	20.02 $\pm$ 0.80 %

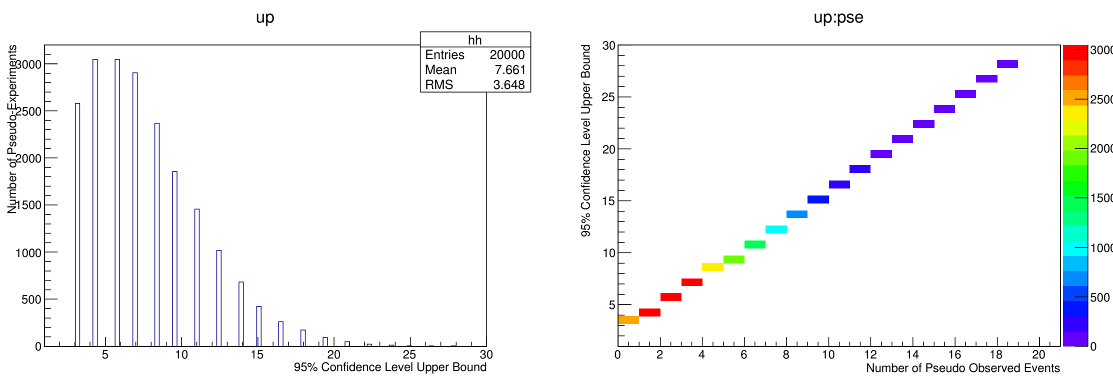

(a) (b)

Figure A.4: Bayesian upper limits on the number of events a model (after efficiency) could produce without being ruled out at 95% confidence. A.4(a) shows the distribution of upper limits from pseudo-experiments while A.4(b) shows the relation between the pseudo-experiments upper limit and the number of observed events it had.

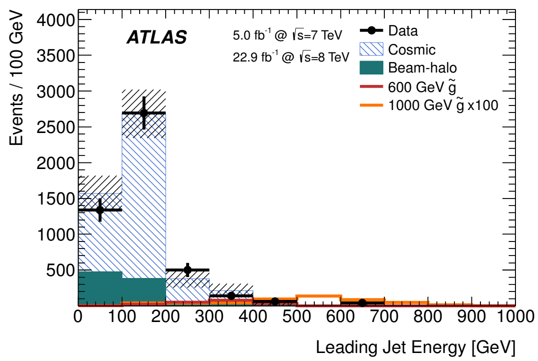

(a)

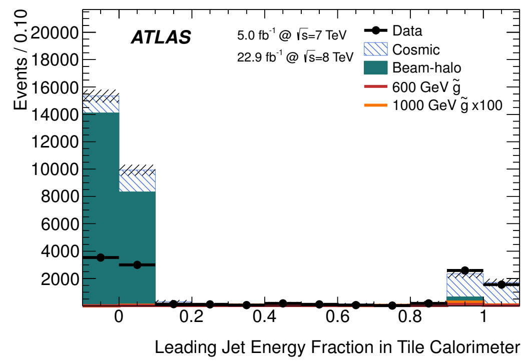

(b)

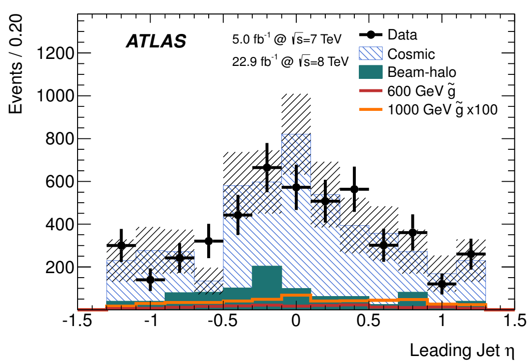

(c)

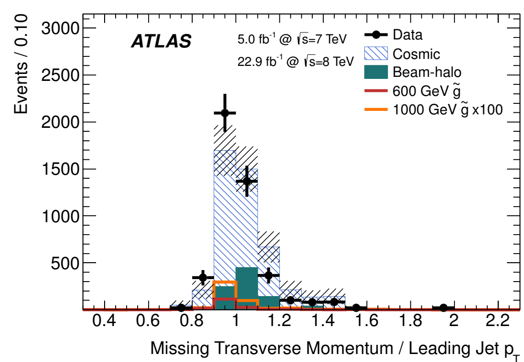

(d)

Figure A.5: Linear Versions of Figure 7.1. Jet variables for the empty bunch signal triggers. The requirements in Table 7.1 are applied except for jet energy > 100 GeV and the final muon veto. To remove overlap in the cosmic and beam-halo sample (which is not done in Table 7.1, an event is not considered "cosmic" if it has a halo-like segment (at least 4 hits, within .2 radians to parallel). For the quantity being plotted, its selection is not applied. Histograms are normalized to the expected number of events in the search region. The jet fraction in the Tile does not agree at low values because the beam-halo method does not account for areas purely in the LAr with poor muon system coverage, and there may also be additional sources of noise in the LAr. This region is not used in the analysis.

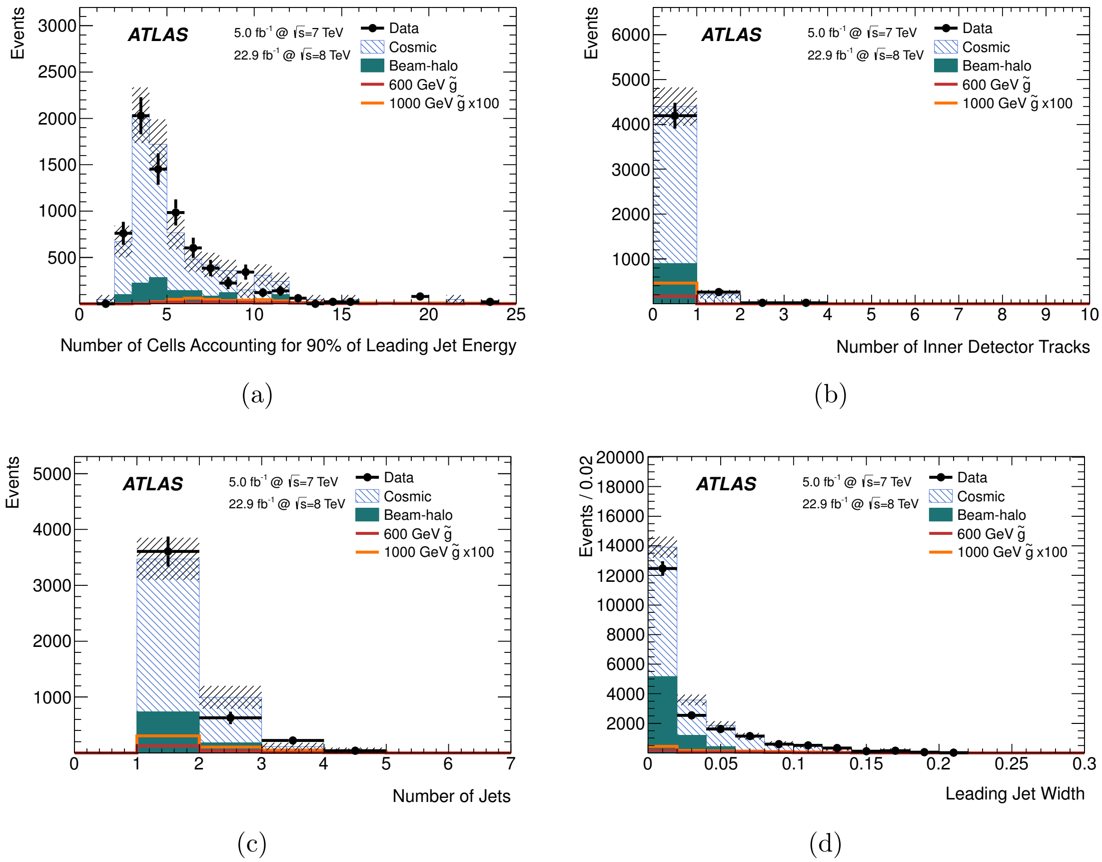

Figure A.6: Linear Versions of Figure 7.2. Jet variables for the empty bunch signal triggers. The requirements in Table 7.1 are applied except for jet energy > 100 GeV and the final muon veto. To remove overlap in the cosmic and beam-halo sample (which is not done in Table 7.1, an event is not considered “cosmic” if it has a halo-like segment (at least 4 hits, within .2 radians to parallel). For the quantity being plotted, its selection is not applied. Histograms are normalized to the expected number of events in the search region.

Glossary

ADC analog-to-digital converter. 46, 135

ASC amplifier/shaper/discriminator. 49, 135

BBN big bang nucleosynthesis. 19, 135

BCID bunch-crossing identifier. 99, 135

BPTX beam position and timing monitors. 29, 51, 53, 135

BR barrel regions. 28, 135

CERN European Laboratory for Particle Physics. 31, 33, 50, 135

COOL CERN online conditions logging database. 99, 135

CSC cathode strip chamber. 28, 47, 49, 50, 61, 124, 135

CSM chamber service module. 49, 135

CTP central trigger processor. 51, 135

DM dark matter. 17, 21, 22, 135

EF event filter. 55, 57, 135

ER endcap regions. 28, 135

FEB front-end board. 44, 46, 135

GMSB gauge-mediated supersymmetry breaking. 2, 5, 22, 135

GRL good runs list. 56, 99, 111, 135

HLT high level trigger. 29, 50, 55, 135

ID inner detector. 41–43, 135

IP interaction point. 39, 41, 135

IR interaction region. 35, 135

LAr liquid-argon calorimeter. 27, 41, 44–46, 50, 52, 60, 74, 135, 138

LHC Large Hadron Collider. 2–4, 20–22, 27–29, 31, 32, 34–39, 41, 51, 54, 55, 61, 65, 68, 99, 123, 135

LLP long-lived particle. 2, 5, 17, 19, 135

LSP lightest supersymmetric particle. 5, 15, 17, 19, 22, 123, 135

MDT monitored drift tubes. 28, 41, 47–49, 61, 124, 135

MET missing transverse momentum. 28, 29, 55, 135

MS muon system. 41, 47, 48, 60, 61, 86, 135

NLSP next-to-lightest supersymmetric particle. 17, 19, 21, 135

PMT photomultipiler tuber. 44, 46, 57, 135

PS proton synchroton. 33, 34, 37, 135

PSB proton synchroton booster. 32, 34, 135

QCD quantum chromodynamics. 9, 15, 18, 135

QFT quantum field theory. 6, 18, 135

ROD read-out driver. 44, 46, 50, 135

RPC resistive plate chamber. 28, 47, 48, 124, 135

RPV R-parity violating. 2, 22, 135

SCT silicon microstrip. 41–43, 135

SM standard model. 3, 4, 6–9, 13–18, 23, 64, 135

split-SUSY split supersymmetry. 2, 5, 20, 135

SPS super proton synchrotron. 34, 37, 135

SUSY supersymmetry. 2, 13–15, 17–22, 65, 135

TDAQ trigger and data acquisition. 50, 51, 135

TDC time-to-digital converter. 49, 135

TGC thin gap chamber. 28, 47, 48, 124, 135

TileCal tile calorimeter. 41, 45, 46, 57, 132, 134, 135

TRT transition radiation tracker. 41, 43, 135

Bibliography

[1] *LBDS and abort gap cleaning*, Evian, France, 2010. CERN.

[2] Study of the spin properties of the Higgs-like particle in the $H \to WW^{(*)} \to e\nu\mu\nu$ channel with 21 fb^{-1} of $\sqrt{s} = 8$ TeV data collected with the ATLAS detector. 2013.

[3] Study of the spin of the Higgs-like boson in the two photon decay channel using 20.7 fb-1 of pp collisions collected at $\sqrt{s} = 8$ TeV with the ATLAS detector. 2013.

[4] G. Aad et al. The ATLAS Experiment at the CERN Large Hadron Collider. *JINST*, 3:S08003, 2008.

[5] G. Aad et al. Search for Heavy Long-Lived Charged Particles with the ATLAS detector in pp collisions at $\sqrt{s} = 7$ TeV. *Phys.Lett.*, B703:428–446, 2011.

[6] G. Aad et al. Search for Massive Long-lived Highly Ionising Particles with the ATLAS Detector at the LHC. *Phys.Lett.*, B698:353–370, 2011.

[7] G. Aad et al. Search for stable hadronising squarks and gluinos with the ATLAS experiment at the LHC. *Phys.Lett.*, B701:1–19, 2011.

[8] G. Aad et al. Observation of a new particle in the search for the Standard Model Higgs boson with the ATLAS detector at the LHC. *Phys.Lett.*, B716:1–29, 2012.

[9] G. Aad et al. Search for decays of stopped, long-lived particles from 7 TeV pp collisions with the ATLAS detector. *Eur.Phys.J.*, C72:1965, 2012.

[10] G. Aad et al. Characterisation and mitigation of beam-induced backgrounds observed in the ATLAS detector during the 2011 proton-proton run. 2013.

[11] G. Aad et al. Jet energy resolution in proton-proton collisions at $\sqrt{s} = 7$ TeV recorded in 2010 with the ATLAS detector. *Eur.Phys.J.*, C73:2306, 2013.

[12] G. Aad et al. Search for long-lived, multi-charged particles in pp collisions at $\sqrt{s}$=7 TeV using the ATLAS detector. *Phys.Lett.*, B722:305–323, 2013.

[13] G. Aad et al. Search for long-lived stopped R-hadrons decaying out-of-time with pp collisions using the ATLAS detector. 2013.

[14] G. Aad et al. Searches for heavy long-lived sleptons and R-Hadrons with the ATLAS detector in pp collisions at $\sqrt{s} = 7$ TeV. *Phys.Lett.*, B720:277–308, 2013.

[15] G. et al Aad. Expected Performance of the ATLAS Experiment - Detector, Trigger and Physics. December 2008.

[16] G. et al Aad. The ATLAS Simulation Infrastructure. *The European Physical Journal C*, 70(3):823–874, September 2010.

[17] T. Aaltonen et al. Search for Long-Lived Massive Charged Particles in 1.96 TeV $\bar{p}p$ Collisions. *Phys.Rev.Lett.*, 103:021802, 2009.

[18] V.M. Abazov et al. Search for Long-Lived Charged Massive Particles with the D0 Detector. *Phys.Rev.Lett.*, 102:161802, 2009.

[19] V.M. Abazov et al. A Search for charged massive long-lived particles. *Phys.Rev.Lett.*, 108:121802, 2012.

[20] V.M. Abazov et al. Search for charged massive long-lived particles at $\sqrt{s} = 1.96$ TeV. *Phys.Rev.*, D87(5):052011, 2013.

[21] G. Abbiendi et al. Search for stable and longlived massive charged particles in e+ e- collisions at s**(1/2) = 130-GeV to 209-GeV. *Phys.Lett.*, B572:8–20, 2003.

[22] P. Abreu et al. Search for heavy stable and longlived particles in e+ e- collisions at s**(1/2) = 189-GeV. *Phys.Lett.*, B478:65–72, 2000.

[23] P. Achard et al. Search for heavy neutral and charged leptons in e^+e^- annihilation at LEP. *Phys.Lett.*, B517:75–85, 2001.

[24] A. Aktas et al. Measurement of anti-deuteron photoproduction and a search for heavy stable charged particles at HERA. *Eur.Phys.J.*, C36:413–423, 2004.

[25] B. Andersson, G. Gustafson, G. Ingelman, and T. Sjostrand. Parton Fragmentation and String Dynamics. *Phys. Rept.*, 97:31–145, 1983.

[26] N. Arkani-Hamed, S. Dimopoulos, G. F. Giudice, and A. Romanino. Aspects of split supersymmetry. *Nucl. Phys.*, B709:3–46, 2005.

[27] A. Arvanitaki, S. Dimopoulos, A. Pierce, S. Rajendran, and Jay G. Wacker. Stopping gluinos. *Phys. Rev.*, D76:055007, 2007.

[28] Asimina Arvanitaki, Chad Davis, Peter W. Graham, Aaron Pierce, and Jay G. Wacker. Limits on split supersymmetry from gluino cosmology. *Phys.Rev.*, D72:075011, 2005.

[29] ATLAS Collaboration. Measurement of the rate of collisions from satellite bunches for the april-may 2010 lhc luminosity calibration. Technical Report ATLAS-CONF-2010-102, CERN, Geneva, Dec 2010.

[30] L S Azhgirey, I S Baishev, K M Potter, and V Talanov. Machine induced background in the high luminosity experimental insertion of the lhc project. page 4 p, Jul 2004.

[31] R. Barate et al. Search for pair production of longlived heavy charged particles in e+ e- annihilation. *Phys.Lett.*, B405:379–388, 1997.

[32] W. Beenakker, S. Brensing, M. Kramer, A. Kulesza, E. Laenen, et al. Soft-gluon resummation for squark and gluino hadroproduction. *JHEP*, 0912:041, 2009.

[33] W. Beenakker, S. Brensing, M. Kramer, A. Kulesza, E. Laenen, et al. Squark and gluino hadroproduction. *Int.J.Mod.Phys.*, A26:2637–2664, 2011.

[34] W. Beenakker, R. Hopker, M. Spira, and P.M. Zerwas. Squark and gluino production at hadron colliders. *Nucl.Phys.*, B492:51–103, 1997.

[35] J. Beringer et al. Review of Particle Physics (RPP). *Phys.Rev.*, D86:010001, 2012.

[36] G. Bhattacharyya. Electroweak Symmetry Breaking and BSM Physics (A Review). *Pramana*, 72:37–54, 2009.

[37] O. Brüning, P. Collier, P. Lebrun, S. Myers, R. Ostojic, J. Poole, and P. Proudlock. *LHC Design Report*. CERN, Geneva, 2004.

[38] C. Friberg, E. Norrbin, and T. Sjostrand. Qcd aspects of leptoquark production at hera. *Phys. Lett. B.*, 403:329, 1997.

[39] M. Cacciari, G. Salam, and G. Soyez. The anti-k_t jet clustering algorithm. *Journal of High Energy Physics*, 2008(04):63, April 2008.

[40] M. Cahill-Rowley, J. Hewett, S. Hoeche, A. Ismail, and T. Rizzo. The New Look pMSSM with Neutralino and Gravitino LSPs. *Eur.Phys.J.*, C72:2156, 2012.

[41] D. Casadei. Reference analysis of the signal + background model in counting experiments. *Journal of Instrumentation*, 7:1012, 2012.

[42] S. Chatrchyan et al. Observation of a new boson at a mass of 125 GeV with the CMS experiment at the LHC. *Phys.Lett.*, B716:30–61, 2012.

[43] S. Chatrchyan et al. Search for heavy long-lived charged particles in pp collisions at $\sqrt{s} = 7$ TeV. *Phys.Lett.*, B713:408–433, 2012.

[44] S. Chatrchyan et al. Search for stopped long-lived particles produced in pp collisions at $\sqrt{s} = 7$ TeV. *JHEP*, 1208:026, 2012.

[45] S. Chatrchyan et al. Search for fractionally charged particles in pp collisions at $\sqrt{s} = 7$ TeV. *Phys.Rev.*, D87:092008, 2013.

[46] S. Chatrchyan et al. Study of the Mass and Spin-Parity of the Higgs Boson Candidate Via Its Decays to Z Boson Pairs. *Phys.Rev.Lett.*, 110:081803, 2013.

[47] S. Chekanov. 2012 statistics on lvps trips and studies of lvps timing, January 2013.

[48] S. Chekanov. 2013 lvps trip monitoring during ls1, January 2013.

[49] S. Chekanov. Tile overflow analysis, January 2013.

[50] S. Coleman and J. Mandula. All Possible Symmetries of the S Matrix. *Physical Review*, 159(5):1251–1256, July 1967.

[51] The ATLAS Collaboration. A particle consistent with the higgs boson observed with the atlas detector at the large hadron collider. *Science*, 338(6114):1576–1582, 2012.

[52] The ATLAS Collaboration. Characterisation and mitigation of beam-induced backgrounds observed in the atlas detector during the 2011 proton-proton run. *Journal of Instrumentation*, 8(07):P07004, 2013.

[53] The CMS Collaboration. A new boson with a mass of 125 gev observed with the cms experiment at the large hadron collider. *Science*, 338(6114):1569–1575, 2012.

[54] S. Dawson. Introduction to electroweak symmetry breaking. pages 1–83, 1998.

[55] Y. R. de Boer, A. B. Kaidalov, D. A. Milstead, and O. I. Piskounova. Interactions of Heavy Hadrons using Regge Phenomenology and the Quark Gluon String Model. *J. Phys.*, G35:075009, 2008.

[56] S. Deser and B. Zumino. Consistent supergravity. *Physics Letters B*, 62(3):335 – 337, 1976.

[57] H. Dreiner and S. Grab. All Possible Lightest Supersymmetric Particles in R-Parity Violating mSUGRA. *Phys.Lett.*, B679:45–50, 2009.

[58] J. Ellis, S. Kelley, and D. Nanopoulos. Probing the desert using gauge coupling unification. *Phys.Lett.*, B260:131–137, 1991.

[59] L. Evans and P. Bryant. LHC Machine. *Journal of Instrumentation*, 3(08):S08001, August 2008.

[60] M. Fairbairn et al. Stable massive particles at colliders. *Phys. Rept.*, 438:1–63, 2007.

[61] G.F. Farrar, R. Mackeprang, D. Milstead, and J.P. Roberts. Limit on the mass of a long-lived or stable gluino. 2010. * Temporary entry *.

[62] D. Z. Freedman, P. van Nieuwenhuizen, and S. Ferrara. Progress toward a theory of supergravity. *Phys Rev D*, 13:3214–3218, June 1976.

[63] M. Fujii and T. Yanagida. Natural gravitino dark matter and thermal leptogenesis in gauge mediated supersymmetry breaking models. *Phys.Lett.*, B549:273–283, 2002.

[64] P. Gambino, G.F. Giudice, and P. Slavich. Gluino decays in split supersymmetry. *Nucl.Phys.*, B726:35–52, 2005.

[65] R. Garoby. RF gymnastics in synchrotrons. 2011.

[66] E. Gianfelice-Wendt, W. Bartmann, A. Boccardi, C. Bracco, E. Bravin, et al. LHC Abort Gap Cleaning Studies During Luminosity Operation. 2012.

[67] J.J. Goodson. *Search for Supersymmetry in States with Large Missing Transverse Momentum and Three Leptons including a Z-Boson.* PhD thesis, Stony Brook University, May 2012. Presented 17 Apr 2012.

[68] Z. Gresce. Standard references and text passages for susy papers, January 2013.

[69] K. Hanke. Past and present operation of the cern ps booster. *International Journal of Modern Physics A*, 28(13):1330019, 2013.

[70] V. Khachatryan et al. Search for Heavy Stable Charged Particles in pp collisions at $\sqrt{s} = 7$ TeV. *JHEP*, 1103:024, 2011.

[71] A. Kraan. Interactions of heavy stable hadronizing particles. *Eur. Phys. J.*, C37:91–104, 2004.

[72] M. Kramer, A. Kulesza, R. van der Leeuw, M. Mangano, S. Padhi, et al. Supersymmetry production cross sections in pp collisions at $\sqrt{s} = 7$ TeV. 2012.

[73] A. Kulesza and L. Motyka. Soft gluon resummation for the production of gluino-gluino and squark-antisquark pairs at the LHC. *Phys.Rev.*, D80:095004, 2009.

[74] A. Kulesza and L. Motyka. Threshold resummation for squark-antisquark and gluino-pair production at the LHC. *Phys.Rev.Lett.*, 102:111802, 2009.

[75] M. Kusakabe, T. Kajino, T. Yoshida, and G. Mathews. Effect of Long-lived Strongly Interacting Relic Particles on Big Bang Nucleosynthesis. *Phys.Rev.*, D80:103501, 2009.

[76] R. Mackeprang. Stable Heavy Hadrons in ATLAS. *Ph.D. Thesis, University of Copenhagen*, 2007.

[77] R. Mackeprang and D. Milstead. An Updated Description of Heavy-Hadron Interactions. *Eur. Phys. J.*, C66:493–501, 2010.

[78] R. Mackeprang and A. Rizzi. Interactions of coloured heavy stable particles in matter. *Eur. Phys. J.*, C50:353–362, 2007.

[79] S. Martin. A Supersymmetry Primer. page 152, September 1997.

[80] N. Arkani-Hamed and S. Dimopoulos. Supersymmetric unification without low energy supersymmetry and signatures for fine-tuning at the LHC. *JHEP*, 06:073, 2005.

[81] E. Noether. Invariante variationsprobleme. *Nachrichten von der Gesellschaft der Wissenschaften zu G?ttingen, Mathematisch-Physikalische Klasse*, 1918:235–257, 1918.

[82] C. Ohm and T. Pauly. The ATLAS beam pick-up based timing system. *Nucl.Instrum.Meth.*, A623:558–560, 2010.

[83] S. Raby. Gauge-mediated susy breaking at an intermediate scale. *Phys. Rev. D*, 56:2852, 1997.

[84] H. Rudolf, J. Lopuszanski, and M. Sohnius. All possible generators of supersymmetries of the s-matrix. *Nuclear Physics B*, 88(2):257 – 274, 1975.

[85] T. Sjöstrand, S. Mrenna, and P. Skands. PYTHIA 6.4 physics and manual. *Journal of High Energy Physics*, 2006(05):26, May 2006.

[86] T. Appelquist, H. Cheng, and B. A. Dobrescu. Bounds on universal extra dimensions. *Phys. Rev. D*, 64, 2001.

[87] The ATLAS Collaboration, G. Aad *et al.* Properties of Jets and Inputs to Jet Reconstruction and Calibration with the ATLAS Detector Using Proton-Proton Collisions at $\sqrt{s} = 7$ TeV. *ATL-COM-PHYS-2010-365.*

[88] V. Khachatryan *et al.* [CMS Collaboration]. Search for stopped gluinos in pp collisions at $\sqrt{s} = 7$ TeV. *Phys. Rev. Lett.*, 106:011801, 2011.

[89] V. M. Abazov *et al.* [D0 Collaboration]. Search for stopped gluinos from $p\bar{p}$ collisions at $\sqrt{s} = 1.96$ TeV. *Phys. Rev. Lett.*, 99:131801, 2007.

[90] Niels van Eldik. The ATLAS muon spectrometer: Calibration and pattern recognition. 2007.

[91] W-M Yao and Others. Review of Particle Physics. *Journal of Physics G: Nuclear and Particle Physics*, 33(1), July 2006.